Thermomechanical and poromechanical behavior of Flechtinger sandstone

MSc.
Alireza Hassanzadegan
aus Teheran

Von der Fakultät VI
Planen Bauen Umwelt
der Technischen Universität Berlin
zur Erlangung des akademischen Grades
Doktor der Ingenieurwissenschaften
(Dr.-Ing.)

genehmigte
Dissertation

Berlin 2013

D 83

dedicated to my parents

Promotionsausschuss:

Vorsitzender:	Prof. Dr. Wilhelm Dominik
Gutachter:	Prof. Dr. Uwe Tröger
Gutachter:	Prof. Dr. Günter Zimmermann
Gutachter:	PD Dr. Arno Zang

Tag der wissenschaftlichen Aussprache: 7. December 2012

Contents

List of Figures

Chapter 1

Chapter 2

Chapter 3

Chapter 4

Chapter 5

List of Tables

Acknowledgements

I would like to gratitude a number of kind people around me without whom it would not be possible to do my study. I would like to acknowledge Guido Blöcher and Günter Zimmermann not just because of giving me this opportunity but also for their support from the time of arrival in Germany. I would like to gratitude Liane Liebeskind for Laboratory assistance and to gratitude Siavash Ghabezloo for his fruitful and constructive comments and suggestions. I would like to thank Professor Tröger for his academic support. Further, I would like to thank all my friends, especially Stephanie Frick, Lorenzo Cremonese, Guy Fitzpatrick, Luca Urpi, and Maren Brehme. I thank you, if you helped me in my experiments, if you lend me a book or shared your data, even if you said hello. Special mention must be made of my wife Parisa who encouraged me a lot.

This research was founded by the German Federal Ministry of Environment, Nature Conservation and Nuclear Safety.

Abstract

The production and injection of water from a geothermal system results in pore pressure changes and consequently changing in the stress acting on the reservoir and surrounding rocks. A decrease in pore pressure due to depletion increases the stress carried by reservoir rock and may result in a various type of deformations at micro and macro scales e.g. elastic and inelastic. At the microscale the rock deformation may be accompanied by rearrangement of contact points, opening and closure of cracks, solid compaction and pore collapse. It may result to reactivation of the faults and surface subsidence at the macroscale. The injection of cold water into a hot water reservoir will contract the rock, albeit the surrounding rock will constrain this contraction and thermal stress will be induced. This thermally induced stress not only influences the rock mechanical properties but also affects the poroelastic parameters and consequently porosity and permeability of the rock.

Acoustic velocity measurements and mechanical tests can be employed to provide the dynamic and static elastic moduli of rock, respectively. Several experiments were performed in this study using a conventional triaxial testing system to investigate thermal effects on acoustic, poroelastic and hydraulic parameters of Flechtinger sandstone, an outcropping equivalent of the (Rotliegend) reservoir rock. The isothermal jacketed drained experiments were performed at 30, 60, 90, 120, and 140°C. Direct and indirect methods were employed to measure the Biot coefficient and porosity variation. In the indirect method, two experiments are required: a hydrostatic compression test on a jacketed specimen to measure the drained bulk modulus of the framework and a hydrostatic compression test on an unjacketed specimen to measure the bulk modulus of the solid grains. The direct method employs a jacketed specimen and the change in pore volume and volumetric strain are measured.

Thermomechanical behavior of Flechtinger sandstone was accompanied by an entropic behavior where the sign of temperature dependence of the drained bulk modulus changes (inversion effect). The inelastic behavior of the rock, the interrelation between thermal expansion coefficient and bulk modulus, and the path dependence of heat transfer processes govern the temperature effects and induced changes in pore geometry. The porosity variation was decreasing with an increase in temperature at low effective pressures and was increasing with a rise in temperature at high effective pressures. The Biot coefficient decreased with increasing effective pressure and temperature. Moreover, the bulk moduli were fitted to exponential functions and aspect ratio distribution and crack porosity were determined for each stress-strain curve. The peak of aspect ratio distribution function increased with temperature which can be assigned to creation of new cracks due to thermal and mechanical loading. Furthermore, a new model was derived to describe the pressure dependence of permeability to poroelasticity theory where the effect of pressure on mechanical and hydraulic properties can be determined.

Abstract

Die Produktion und Injektion von Wasser aus einem geothermischen System in ein Reservoir führt zu Porendruckänderungen und damit zu Veränderungen der Spannungen im Reservoir und in den umliegenden Gesteine. Eine Abnahme des Porendrucks durch Überproduktion erhöht den Stress auf das Reservoirgestein und kann verschiedene Arten von Deformationen in verschiedenen Skalenbereichen hervorrufen, z.B. elastische und unelastische. Auf der Mikroskala kann die Verformung durch Verschiebung von Kornkontakten, Öffnen oder Schließen von Rissen, Kompaktion oder Porenversagen begleitet werden. Es kann zur Reaktivierung von Störungen oder zu Setzungserscheinungen an der Oberfläche auf der Makroskala kommen. Die Injektion von kaltem Wasser in einen Warmwasserspeicher würde das Gestein thermisch kompaktieren, jedoch hemmt das Korngerüst des Gesteins die Kompaktion, wodurch wiederum thermischer Stress induzieret wird. Der thermisch induziert Stress beeinflusst nicht nur die gesteinsmechanischen Eigenschaften, sondern wirkt sich auch auf die poroelastischen Parameter und somit auch auf die Porosität und Permeabilität des Gesteins aus.

Akustische Geschwindigkeitsmessungen und mechanische Tests können verwendet werden um die dynamischen und statischen Elastizitätsmoduli von Gesteinen zu bestimmen. In dieser, Studie wurden mehrere Experimente zur Bestimmung von thermischen Effekten auf akustische, poroelastische und hydraulische Parameter durchgeführt. Unter Verwendung eines herkömm-lichen Triaxial-Systems wurden Proben des Flechtinger Sandsteins geprüft. Der Flechtinger Sandstein ist ein Analogmaterial zu den Rotliegend Sedimenten des geothermischen Reservoirs in Groß Schönebeck. Die Experimente wurden bei verschiedenen Temperaturen anhand von ummantelten und drainierten Proben bei 30, 60, 90, 120 und 140 °C durchgeführt. Direkte und indirekte Methoden wurden eingesetzt, um den Biot-Koeffizienten und die Porositätsveränderung zu messen. Für die indirekte Methode werden zwei Experimente benötigt: Hydrostatische Kompression einer ummantelten Probe, um das Kompressionsmodul des drainiert Korngerüstes zu erhalten, und die hydrostatische Kompression, einer nicht ummantelten Probe, um das Kompressionsmodul der Körner zu messen. Das direkte Verfahren verwendet eine umschlossene Probe wobei die Änderung des Porenvolumens und die volumetrische Spannung gemessen wird.

Das thermomechanische Verhalten des Flechtinger Sandsteins wurde von einem entropischen Verhalten begleitet, wobei sich die Abhängigkeit des drainierten Kompressionsmoduls von der Temperatur abhängt. Das inelastische Verhalten des Gesteins, die Wechselwirkungen zwischen dem thermischen Ausdehnungskoeffizienten und dem Kompressionsmodul und die Wärmeübertragung auf verschiedenen Fließwegen ruft Veränderungen der Porenraumgeometrie hervor. Die Porosität nimmt mit dem Temperaturanstieg bei niedrigem Effektivdruck ab und steigt mit einem Anstieg der Temperatur bei höheren Effektivdrücken. Der Biot-Koeffizient nimmt mit zunehmendem Effektivdruck und sinkender Temperatur ab. Darüber hinaus wurden die Kompressionsmoduli an Exponentialfunktionen angepasst und das Seitenverhältnis und die Riss-Porosität wurde für jede Belastungs-Kurve bestimmt. Das Maximum der Seitenverhältnis-Verteilungsfunktion stieg mit der Temperatur, was auf die Bildung von neuen Rissen aufgrund thermischer und mechanischer Belastung zurückgeführt werden konnte. Des Weiteren wurde ein neues Modell abgeleitet welches die Druckabhängigkeit der Permeabilität auf Basis Poro-Elastizitts-Theorie zeigt, Dabei wird der Einfluss des Drucks auf die mechanischen und hydraulischen Eigenschaften beschrieben.

Preface

The present dissertation comprises four manuscripts that I have published or submitted for publication during the course of my doctoral studies. This research addresses the thermomechanical effects in Groß Schönebeck geothermal reservoir in the North German Basin. Two wells have been drilled and completed mainly in Rotliegend sandstones to circulate the water within the reservoir and to extract thermal energy. Injection of cold water initiates a transient thermal behavior in the vicinity of the injection well which in concert with pressure can alter the rock properties. The stress changes due to thermal effects could be estimated if the poroelastic coefficients are known. Consequently, in this dissertation I focus on thermal effects on poroelastic parameters and transport properties (e.g. porosity and permeability). In the first chapter I present an introduction to the thermo-poromechanics and then I presents the manuscripts submitted for publication. The bibliography of the manuscripts (one conference proceeding and three ISI papers) is given here:

- **Chapter 2:** Hassanzadegan, A., Blöcher, G., Zimmermann, G., Milsch, H., Moeck, I. (2011). Induced Stress in a Geothermal Doublet System, Proceedings, Thirty-Sixth Workshop on Geothermal Reservoir Engineering Stanford University, Stanford, California, SGP-TR-191.

- **Chapter 3:** Hassanzadegan, A., Blöcher, G., Zimmermann, G., and Milsch, H. (2012). Thermoporoelastic properties of Flechtinger sandstone. International Journal of Rock Mechanics and Mining Sciences, 49:94-104.

- **Chapter 4:** Hassanzadegan, A., Blöcher, G., Milsch, H., Urpi, L., Zimmermann, G. (2012). The effect of temperature on static and dynamic elastic moduli of Flechtinger sandstone, Rock Mechanics and Rock Engineering (accepted for publication).

- **Chapter 5:** Hassanzadegan, A., Zimmermann, G., (2012). The poroelastic description of permeability evolution, Pure and Applied Geophysics (accepted).

During the time of my study, I first built a reservoir model and simulated the hydromechanical behavior on the reservoir scale to understand the mechanisms involved. I found that stress changes within the reservoir can be calculated if the appropriate hydraulic and poroelastic parameters are known (Chapter 2). Afterwards, I performed several experiments using a conventional triaxial system and investigated thermal effects on poroelastic and hydraulic properties (Chapters 3, 4 and 5).

Chapter 1

Introduction and summary

1 Introduction

This research is an interdisciplinary study which addresses the coupling phenomenon (Fig. 1) occurring in the Enhanced Geothermal System (EGS) of the Groß Schönebeck geothermal reservoir, located in North German Basin. Coupling of deformation and pore pressure diffusion (Darcy's law) characterizes the poroelastic response of fluid-saturated porous rocks. Thermal stress may arise in a heated body either because of a non-uniform temperature distribution, external boundaries, a mismatch in thermal expansion of heterogeneous rock mass or combination of them. The thermomechanical behavior of fluid-saturated porous rock is important in a number of diverse areas. Arised problems involve strong coupling between heat transfer, pressurization and motion of interstitial pore fluid and deformation of the porous matrix. The equations of poroelasticity are coupled in both directions, that is pore pressure influences the deformation and the deformation influences the pore pressure, coupling in thermoelasticity is much more unidirectional. That is, temperature influences deformation and stresses; however the effect of stresses and deformation on temperature field is negligible. The heat and mass transfer are also coupled, taking into account the mechanical effects, the preferred flow path in porous media affects the thermal field and conductive and convective heat transfer influences the fluid flow.

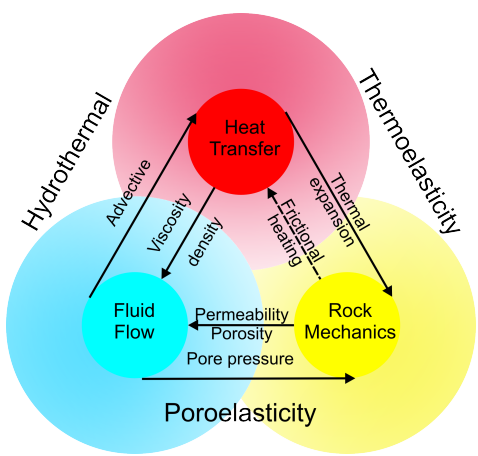

Figure 1: Thermo-Hydro-Mechanical processes. Each process affects the initiation and progress of the other one (Arno Zang, personal communication).

The Groß Schönebeck site is geographically located at approximately 40 km north of Berlin (Fig. 2). The Groß Schönebeck reservoir is a confined aquifer, located at about 4 km depth within the Lower Permian of the North East German Basin. Injection of cold water into a hot water reservoir will contract the rock, however the surrounding rock will constrain this contraction and thermal stress will be induced.

This thermally induced stress not only influences the rock mechanical properties but also affects the poroelastic and consequently transport properties of the rock. A doublet system will be applied in Groß Schönebeck geothermal reservoir. One vertical well as an injector and one deviated well as a production well have been completed in Rotliegend sandstone formation and volcanic rock. The deviated well benefits from higher contact area between well and reservoir and possibility of creating several parallel hydraulic fractures. Stimulation treatments have been performed to enhance the productivity of the wells. Different concepts can be employed to enhance the reservoir performance by stimulation e.g. hydraulic fracturing, thermally induced fracturing, and chemical-acid stimulation (Zimmermann et al., 2011). The hydraulic stimulation experiments were performed at the Groß Schönebeck field in 2007, which was followed by matrix acidizing treatment in 2009. The productivity index increased from 2.4 $m^3/(hMPa)$ before stimulation to 10.1 $m^3/(hMPa)$ after stimulation (Zimmermann et al., 2011).

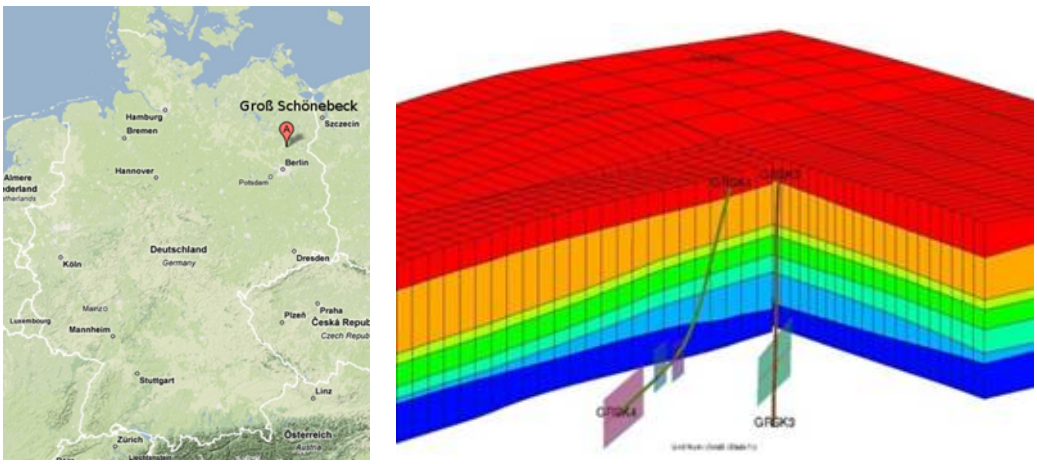

(a) Location (b) Injection and production well

Figure 2: Location and development of Groß Schönebeck geothermal reservoir

The stratigraphy of the reservoir is given by Moeck et al. (2008). The reservoir formation comprises two different rock types: sedimentary sandstone and volcanic rocks. The main reservoir formation interval are the sandstones of the Upper Rotliegend (Dethlingen Formation). A shale cap rock covers the reservoir. Underneath, the Hannover formation is placed which has a high concentration of silts and mudstones. The Dethlingen formation consists of three sub layers: 1) Elbe alternating sequence, mostly consists of silt to fine grained sandstone. 2) Elbe base sandstone- II composed of fine grained sandstone. 3) Elbe base sandstone -I, consists of fine to middle grained sandstone. The Havel formation is the most lowest sedimentary geological unit, consisting of mainly conglomerates. Beneath the sedimentary strata, a volcanic formation is placed.

The in situ stress state was determined for Lower Permian formation by Moeck et al. (2008). The minimum horizontal stress magnitude was evaluated by hydraulic fracturing to be 54 MPa. The vertical stress was estimated by considering the average weight of the overburden to be 100 MPa and the bounds on maximum horizontal stress were calculated based on sliding friction coefficient. The azimuth of the maximum horizontal stress was obtained by analysing the acoustic borehole televiewer (ABF14) images and formation microimages (FMI) to be 18.5±3.7°. The pore pressure was determined by production logs at stationary condition to be 43 MPa at a depth of 4100 m depth (Moeck et al., 2008). The Hannover formation has a temperature of 138°C and temperature increases continuously to 147°C for the volcanic rocks.

The interpretation of 2-D seismic data characterized the fault pattern with major NW-striking faults

and NE-striking minor faults. The NE-trending faults (minor faults) holds the highest ratio of shear to normal stresses. These faults reveal a critically stress state in the sandstone and a highly stressed state in the volcanic layer. Since critically stressed faults are described as hydraulically conductive (Barton et al., 1995), hence, close to slipping or active faults are expected to be the main fluid pathways in the reservoir e.g. Moeck et al. (2008). The orientation of the microseismic events was approximately in the north-south direction and was similar to the maximum horizontal stress direction (Kwiatek et al., 2008).

1.1 Reservoir Geomechanics

Production and injection of water into an aquifer cause changes in pore pressure and therefore changes in stresses acting on the reservoir and surrounding rocks and may lead to rock deformation, fault reactivation and rock failure. Under a critical stress state, a small change of the effective stress caused by fluid-pressure changes in the reservoir is likely to reactivate the movement on normal faults (Moeck et al., 2008). If the in situ stress is not critical the reservoir rock will deform and may alter the rock properties. The well productivity during the life cycle of the reservoir is strongly dependent on the rock properties (e.g porosity and permeability) in the vicinity of the wells and within the reservoir. In the neighborhood of the production well the pore pressure drops and the effective stress increases. When the pressure drops the rock experience a higher acting load and may deform. If the strains are high enough, the rock may fail in shear or tension. Three stress regimes can be defined if the rock fails in shear: normal, thrust (reverse) and strike-slip regimes (Fig. 3). These stress regimes can be described and characterized in accordance with fault regimes (Anderson, 1951). The strength of the rock, the stress level at which rock fails, is a function of pore pressure and principal effective stress components, the eigenvalues of the stress tensor, and can be determined by various test types such as uniaxial compressive strength, tensile strength, etc. If the strains are small in comparison with strains at failure the rock may deform elastically.

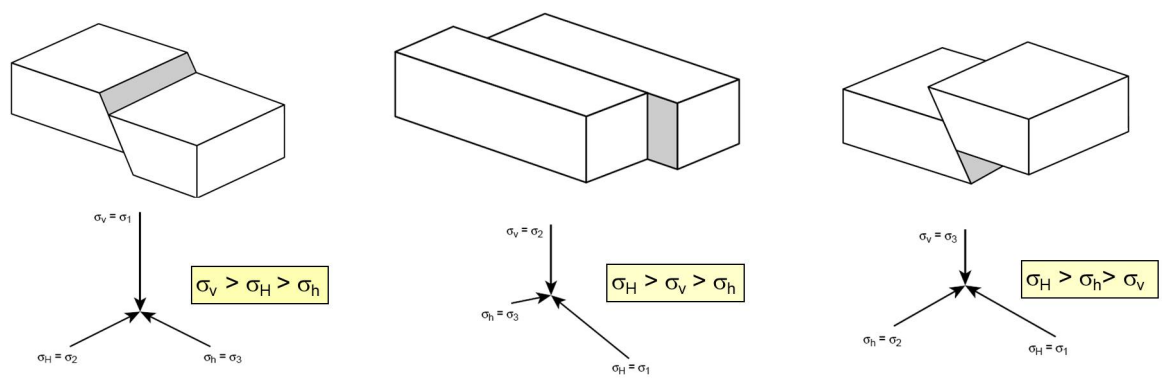

(a) Normal fault regime (b) Strike-slip fault regime (c) Reverse fault regime

Figure 3: Three fault regimes (Anderson, 1951).

The total amount of energy that can be extracted from a geothermal reservoir fluid strongly depends on the production temperature. Moreover, from the reservoir management point of view it is essential to keep the pore pressure within the reservoir constant. Thus, the produced water after extraction of heat will be reinjected into the reservoir. The production and injection of geothermal fluid has some mechanical consequences which is due to change of pressure, temperature and stress.

The rock mechanical effects can be considered either at reservoir size or grain size. At the reservoir scale the mechanical behavior of the reservoir and surrounding rock may result in wellbore stability problems, casing collapse, reservoir compaction, subsidence at the surface, fault reactivation, etc. As

the effective stress increases with reduction in pore pressure, the rock will shrink and the reservoir will compact. The reservoir compaction may cause subsidence at the ground surface or anisotropic stress changes in surrounding rocks (Soltanzadeh and Hawkes, 2008). If the reservoir was a free body it would simply contract or expand due to changes in effective stress and temperature. However, the reservoir rock is constrained by the surrounding rock which acts against the compaction or expansion of the reservoir rock. As a results of this competition between internal driving forces and external constraints anisotropic stress changes may be induced depending on discrepancies between mechanical properties of reservoir and surrounding rocks, reservoir geometry and pore pressure distribution (Soltanzadeh and Hawkes, 2008). That is, instead of having subsidence at the surface during depletion, the weight of the overburden would be carried by the sideburden and thereby sideburden is compacted while the overburden is stretched. The inverse process might occur while injecting water into the reservoir (Segall and Fitzgerald, 1998; Bandura, 2012). Segall and Fitzgerald (1998) stated that if the depleted reservoir is located in an extensional regime, a normal faulting would occur on the flank of the reservoir, whereas in compressional regime a reverse faulting would be induced above and below the depleted reservoir (Fig. 4). Segall and Fitzgerald (1998) concluded that stress changes within the reservoir can be estimated if the appropriate poroelastic parameters are known. The stress changes due to production may results in normal faulting within the reservoir if the Biot coefficient is large enough.

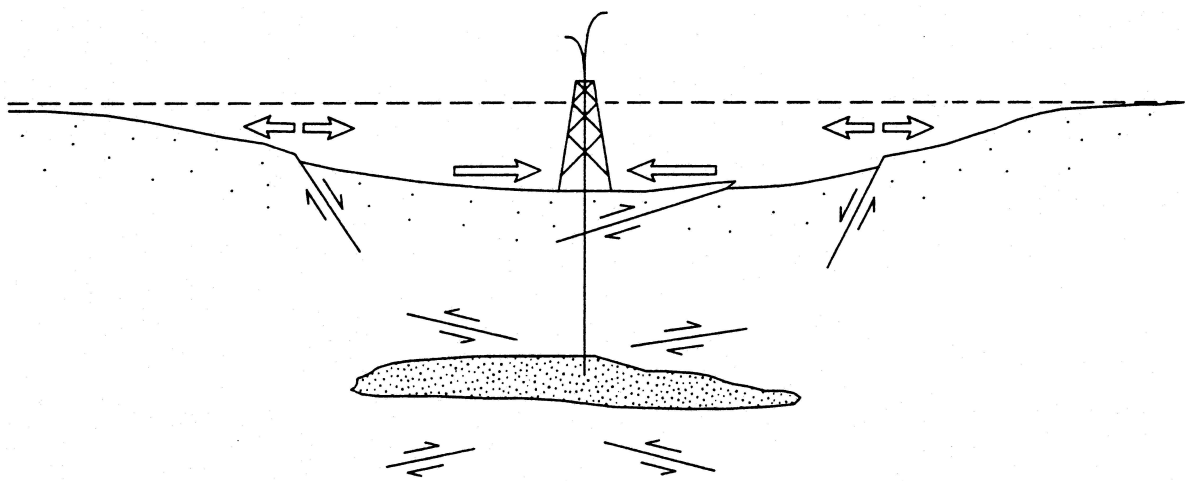

Figure 4: Surface deformation and faulting associated with reservoir depletion (Segall and Fitzgerald, 1998). Normal faults may occur on the flank of the reservoir and reverse faulting would be induced above or below a depleted reservoir.

1.2 Poromechanics

The presence of fluid in porous rock modifies its mechanical behavior. The constitutive equations of poroelastic theory or Biot theory was first proposed by Biot (1941) and developed afterwards by Biot (1956); Biot and Willis (1957); Rice and Cleary (1976). The linear theory of poroelasticity presents the coupling between rock and fluid as a generalization of one-dimensional theory of soil consolidation (Terzaghi, 1923). The coupling between fluid and porous rock is governed by two key mechanisms: the rock will dilate due to increase of pore fluid pressure and on the other hand compression of the rock causes an increase in pore pressure (Detournay and Cheng, 1993). The diffusion of excess pore pressure leads to a time dependent behavior in deformation of the rock. The rock appear compliant at drained conditions and more stiff at undrained conditions. Two kinematics quantities describes the conceptual theorem; the

deformation of the porous media with respect to reference configuration is defined by strain tensor ε_{ij} and increment of fluid content ζ is defined to be the increment of fluid volume per unit reference bulk volume. The sign convention of elasticity considers the compressive stresses to be negative but fluid pressure is positive. In contrast, the sign convention of rock mechanics assumes that compressive stresses are positive. The increment of fluid content ζ is positive when the mass is transferred to the control volume or fluid gained by porous solid. The conjugate quantities express the thermodynamic potential of the system. The conjugate quantities of the strain and fluid increment content are Cauchy stress tensor σ_{ij} and pore pressure P_p, respectively. That is, the work increment associated with strain increment $d\varepsilon$ and $d\zeta$ in the presence of stress σ_{ij} and P_p is given by $dW = \sigma_{ij}d\varepsilon + P_p d\zeta$. The pore pressure is in equilibrium with porous solid. Biot coefficient α is defined as the efficiency of pore fluid in counteracting the total applied stress. The elastic response requires a linear relation between stress (σ_{ij}, P_p) and the strain (ε_{ij}, ζ), the components of stress are linearly related to the components of strain. Some assumptions are implicitly introduced in a linear formulation:

1. Proportionality: given a variable stress or strain (x=σ or ε) its contribution to total is ax, where a is a constant parameter.
2. Additivity: the total strain is the sum of individual strain
3. Divisibility: a body that can be continually sub-divided into infinitesimal small elements with properties being those of the bulk material.
4. Time independent, the complete stress-strain curve is not a function of applied stress. For example, in a creep response material continues to strain whereas the applied stress is held constant.

In a porous media, the rock properties can be simplified by describing the properties in terms of equivalent continuum (effective properties). Therefore the equations will be solved for this continuum rather than pore space (properties are assumed to vary continuously from one point to another). In this kind of formulation the interaction between parameters is neglected and no setup value for start of the strain is assumed. In addition, the proportionality coefficients are constant and do not vary by change in the variable value (material properties are constant).

Moreover, it is based on the reversibility assumption where there is no energy dissipation during a closed loop cycle of deformation process. Therefore, it would be possible to employ the superposition principle and describe the elastic deformation of the rock in terms of two states of equilibrium as illustrated in Figure 5.

The effect of boundary conditions on fluid low while deforming the sample can be categorized into two extreme cases whether the fluid is allowed to expelled out (drained condition) or the boundary is sealed (undrained conditions). Figure 6 describes the concepts and terminologies that are employed in poroelasticity theory.

The effective elastic properties of crustal rock are controlled to a large extent by porosity (Walsh, 1980). The effect of pore space on bulk modulus have been studied by Eshelby (1957) using energy approach. The rate of change of porosity with applied load first was given by Walsh (1965) where the difference between bulk modulus of solid grains and bulk modulus of porous material determines the rate of change of porosity with pressure. The porosity of rock has been divided by Walsh (1980) into two categories: equant dimensional pores and flat pores or low aspect ratio pores (cracks). The low aspect ratio pores (long, narrow cracks) particularly reduce the effective moduli of rocks. The pores with a circular shape are the stiffest type of elliptical pores and becomes compliant as their elliptical aspect ratio decreases. Moreover, the bulk modulus of rock may increase with increasing confining pressure due to the closure of the cracks (Brace, 1965; Walsh, 1965). Carroll and Katsube (1983) described the rate of change in porosity with poroelastic parameters and McTigue (1986) included thermal effect on porosity evolution.

To quantify the effect of pore geometry on elastic moduli of the rock a common approach is to solve elasticity equation for a rock containing a regular pore shape and applying proper internal and external

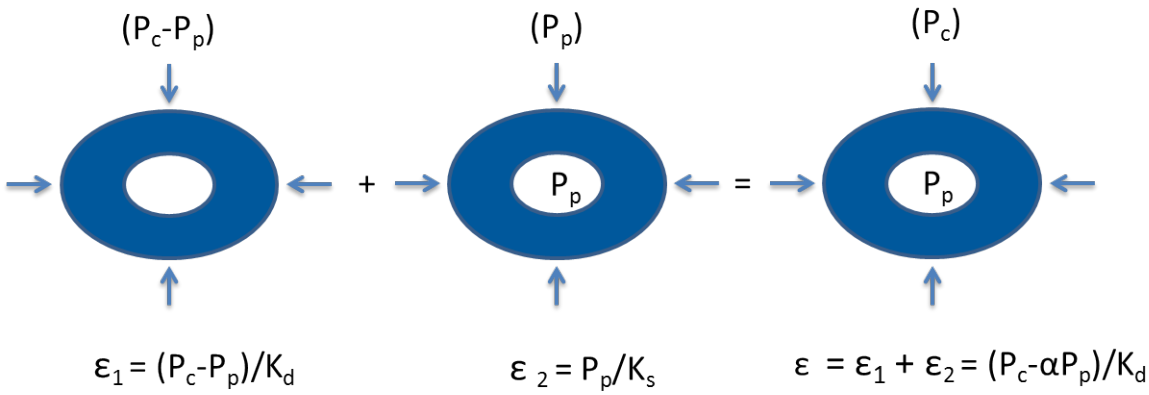

Figure 5: The superposition principle is applied to describe the elastic deformation of the rock. The state of stress can be described by two states of equilibrium (I) a pressure of $(P_c - P_p)$ acting on the external surface and a zero pore pressure and (II) a hydrostatic pressure of P_p applied to pore space and external surface of the rock

boundary conditions. Complex-variable method have been utilized by Zimmerman (1991) to study the two dimensional irregular pore shapes. Mavko and Nur (1978) studied the deformations of non-elliptical cracks in a loaded elastic material. Mackenzie (1950) derived the effective bulk modulus of the porous material, where the bulk modulus is a function of porosity, solid bulk and shear moduli. Each type of pore has a different effect on elastic and hydraulic properties of the rock. Brace (1965) differentiated the equant pores and cracks depending on their pressure dependence fluid flow response; the cracks close under pressure while pores remain open to the fluid flow. While the pore volume changes of the cracks is not significant but it controls the fluid flow pathways and consequently the permeability of the rock. Sisavath et al. (2000) studied the effect of pore shape function and deformation of the pores on the hydraulic conductance of the rock.

The applied stress acting on the rock may be accompanied by elastic or inelastic deformations. The constitutive equations of the rock, the relation between stress and strains, are different from the other material, since the geomaterials are pressure dependent and their strength and deformation depends on mean stress values (Fredrich and Fossum, 2002). Moreover, the basic differences in mechanical behavior of the metal and porous rock are found to be the presence of pores and the tendency to maintain constant volume during compression and shear (Lade, 1988). Lade (1988) summarized that theory of elasticity and work hardening plasticity theory could describe the mechanical behavior of both materials. Brace (1978) categorized the deformation in granular materials to elastic changes in mineral, compaction of the solid minerals accompanied by pore space reduction and dilatancy or pore space increase. In addition, a number of microscope inelastic deformation mechanisms such as grain sliding, grain rotation, intergranular cracks (Hertzian crack at the point of contacts), cement breakage and pore collapse might be triggered. Walsh (1973) stated that stress state in a granular rock subjected to a uniform change in temperature or uniform applied stresses is generally not uniform. He defined the internal stress as the difference between this complicated stress state and the stress that would exist if the rock was homogeneous. The internal stress depends on grain shape and the mismatch of thermoelastic properties of the neighboring grains, e.g. anisotropic elastic moduli and anisotropic thermal expansion of minerals.

Permeability is a measure of the geometry of the pores and pore dimension (Brace, 1978). Thus, by change of pore geometry or crack closure the permeability would change. Bear (1988) described the conceptual models employed to derive Darcy's law from the basic principles underlying the theory of hydrodynamics. Furthermore, permeability is a measure of the ease of fluid flow through porous media

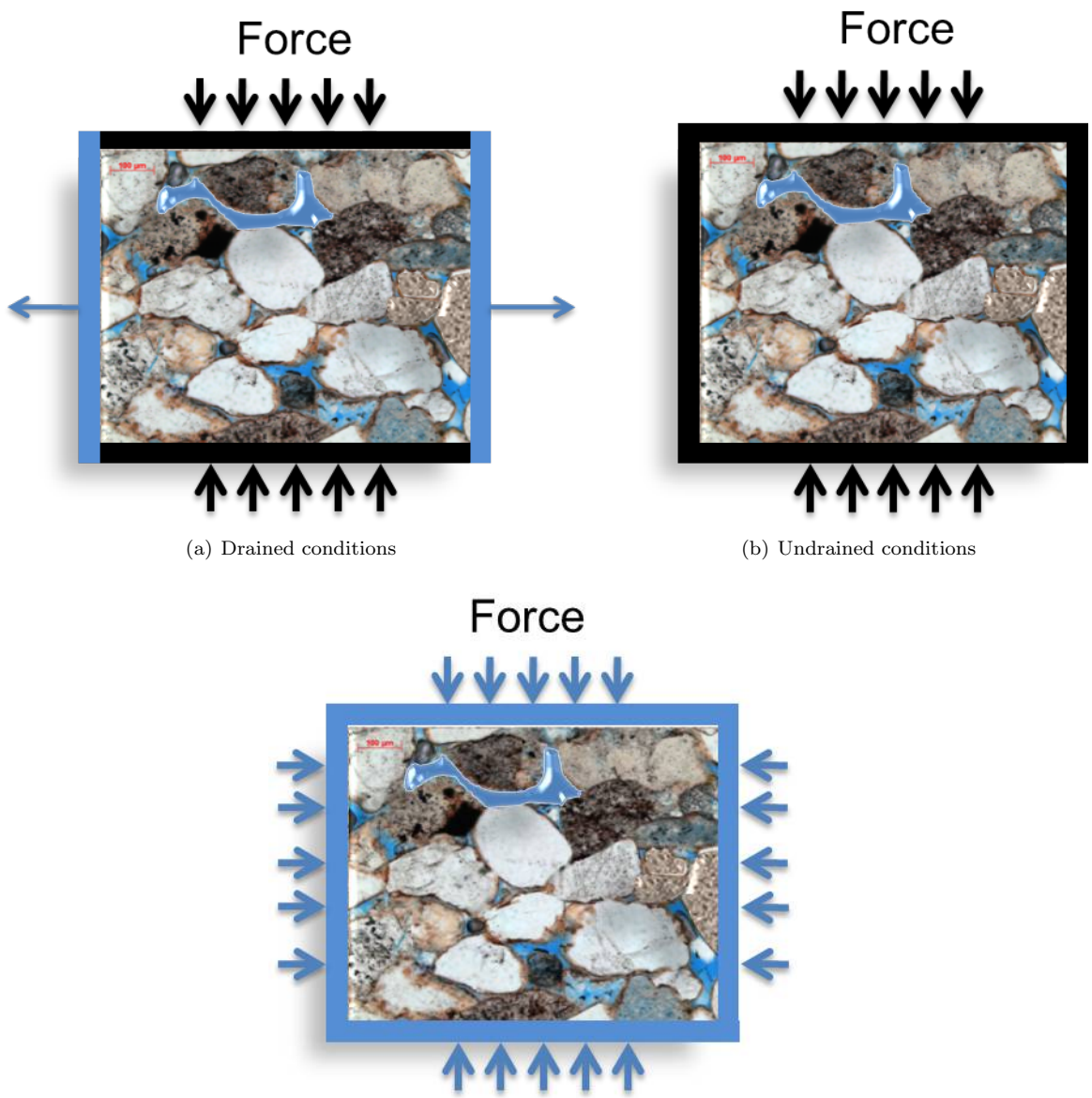

(a) Drained conditions

(b) Undrained conditions

(c) Unjacketed conditions

Figure 6: Two extreme cases can be distinguished whether the pore fluid is allowed to drained out (drained conditions) or when the fluid can not escape the porous rock (undrained conditions). The third case is when the internal pore pressure and external load are equal (unjacketed conditions).

which can be estimated in field scale or laboratory scale. In reservoir engineering, the permeability could be derived by direct and indirect methods. In indirect methods permeability could be estimated from porosity and water saturation correlation, lithology and porosity correlation, or Stoneley wave analysis (Economides and Nolte, 2000). The permeability may be estimated directly by formation tests or well tests. In the laboratory, there are two different approaches to estimate permeability: theoretical modeling based on the packing arrangement of the grains and pore structure, and the empirical relations (e.g. Darcy's law, porosity-permeability correlations, etc.). Renard and de Marsily (1997) explained various methods to calculate the equivalent permeability and block permeability where the permeability not only depends on boundary conditions but also on the permeabilities inside and outside the block. The dependency of permeability on porosity can be described by various pore space geometry attributes such as average pore diameter, grain size, hydraulic radius, tortuosity, internal pore surface, etc. Guéguen et al. (1996) described the main experimental methods to identify the characteristic length and reviewed the various models.

1.3 Thermoporomechanics

The main influence of changes in temperature is volume change. The induced thermal stress and volume changes depend on the applied mechanical boundary conditions. The effects of mechanical boundary have been illustrated in Figures 7(a) and 7(b). A free thermal expansion or contraction would occur when there is no external force acting on the surface boundary. In this case, increasing or decreasing of temperature causes material to expand or shrink, respectively. The thermal stress develops if a structure or member is completely constrained (not allowed to move at all). The thermal stress is a product of the coefficient of thermal expansion, the temperature change, and elastic modulus of the material.

(a) The movement joint expands or contracts due to temperature changes.

(b) The thermal stress which develops if a structure or member is completely constrained.

Figure 7: A temperature change may result in thermal expansion or thermal stress, depending on the applied boundary conditions.

A survey of geothermal properties exhibited a correlation between permeability, porosity of the rock and temperature. In general, temperature increases with depth and by increasing overburden pressure,

porosity and permeability decreases. A possible explanation is argued to be thermal expansion of the rock which has increased the number of closed void spaces. Another explanation is the clogging of pore space due to deposition of calcite, the solubility of calcite decreases with increasing temperature. Albeit, the in situ conditions may alter due to production and injection of water in a geothermal reservoir.

Injection of cold water results in an increase in pore pressure, a decrease in temperature and change in stress state, specially near the wellbore area (rock shrinkage may happen). The water will flow through a more conductive pathway to reach the production well. It has been recognized that there is a strong correlation between orientational frequency of major axes of breakthrough and maximum principal horizontal stress axis (Heffer, 2002). The time required is recognized as flood breakthrough time and the moment at which the temperature front reaches the production well is known as thermal breakthrough time. In this case water interacts with porous media and influences on thermoelastic, poroelastic and chemical properties.

The previous works have described the importance of heat and fluid flow and their coupling behavior for different rock types and how the thermoelasticity is controlled by diffusivity of fluid and heat into the formation. The material constants appearing in these equations can be organized into five groups:

1. Mechanical: shear modulus, drained bulk modulus.
2. Thermal: drained thermal expansivity, volumetric heat capacity, thermal conductivity.
3. Hydromechanical: Biot coefficient, Skempton coefficient, undrained bulk modulus.
4. Thermohydromechanical: thermal pressurization and hydrothermal coupling coefficients.
5. Transport phenomena: permeability, viscosity.

The conductive heat transfer process is already included in linear theory but the convection heat transfer is not included. McTigue (1990) employed an analytical approach to study the effect of convective heat transfer. The Peclet number, the ratio of convective to conductive heat flux, was calculated to be in order of 10^{-5} for Berea sandstone which suggests that convective heat transfer processes might be ignored (McTigue, 1990).

When thermal diffusivity is much lower than hydraulic diffusivity (e.g. high permeability rock), fluid flow accommodates thermal expansion of minerals. That is, the excess fluid pressure relaxes rapidly in comparison to the rate of temperature changes, the fluid pressure remains constant and the material exhibits a drained response. On the other hand, when thermal diffusivity is much higher than hydraulic diffusivity, e.g. very low permeability rock, a rapid heating occurs and porous rock exhibits an undrained response. At undrained conditions, the fluid is immobilized and the fluid mass content is constant. McTigue (1986) presents a general solution scheme in which both compressibility and thermal expansion coefficients of fluid and rock skeleton are different. This theory indicates that diffusion heat conduction process governs the pore pressure and mean total stress. The heat transfer boundary conditions were set either as a constant temperature at the boundary or a constant heat flux. For the drained boundary condition, solutions exhibit a peak in fluid pressure that propagates into the medium with time, resulting in flow both toward and away from the boundary. An impermeable boundary results to a pressure maximum at the boundary and flow into the half space; these limiting cases are strongly associated with the ratio of the fluid and thermal diffusivities χ/λ. Fluid diffusivity χ is defined to be the product of permeability k and bulk modulus K divided by fluid viscosity μ. When $\chi/\lambda \to \infty$ (e.g. for a large permeability), the fluid pressure relaxes rapidly in comparison to the rate of temperature change and the material exhibits a drained response. For $\chi/\lambda \to 0$ (e.g., for a very small permeability), the fluid is immobilized on the time scale of the heat transfer, and undrained behavior is obtained. In other words, in rocks with a low permeability and very compressible fluids, a change in temperature induces a change in pore pressure, while in permeable rocks, mechanical deformation, pore pressure and temperature are not coupled (McTigue, 1986).

The volume change in a thermal process is defined by the thermal expansion coefficient and under mechanical load is characterized by bulk modulus or incompressibility coefficient. The interaction between thermal and mechanical processes governs the induced thermal stresses and strains. Palciauskas and Domenico (1982) described the change in the volume of the rock when the stress, fluid pressure, and temperature are varied. McTigue (1986) presented a more general solution scheme in which both compressibility and thermal expansion coefficients of fluid and rock skeleton are different. Both studies distinguished two extreme cases: drained condition or long term response and undrained condition or short term response. Temperature effects not only change the in situ stress field and the productivity of a doublet geothermal system such as Groß Schönebeck (Huenges et al., 2006; Blöcher et al., 2008), but also induce nonlinearity due to the temperature dependence of physical properties. Of principal importance are bulk modulus and thermal expansion coefficient and their changes with pressure and temperature. In both linear theories of poroelasticity (Biot, 1941; Rice and Cleary, 1976; Detournay and Cheng, 1993) and thermoporoelasticity (Palciauskas and Domenico, 1982; McTigue, 1986) physical properties are constant; however, these properties are temperature and pressure dependent for a granular rock.

The thermal effects on mechanical behavior of a reservoir rock can be better described if the constitutive equations describe the microscopic physical processes at given conditions (Palciauskas and Domenico, 1988). Of main importance are the porosity and pore geometry evolution of the porous rock due to the applied pressure and thermal load. Palciauskas and Domenico (1982) and McTigue (1986) extended the poroelastic theory to consider thermal effects and derived the linear constitutive equations. McTigue (1986) derived a porosity evolution relationship which included the compressibility of the porous solid. He differentiated between the bulk moduli of the porous solid containing trapped pores (unconnected porosity) and the one which is only described by effective porosity (connected pores). In this model, the porosity may decrease or increase depending on the discrepancy between thermal expansion coefficients of the porous solid containing trapped pores and the effective ones. Angevine and Turcotte (1983) derived a viscoelastic model which predicted the porosity evolution of quartz arenite with a temperature dependent viscosity of an Arrhenius type. Somerton et al. (1981) observed a reduction in porosity with increasing temperature under drained conditions. He ascribed this behavior to a lateral deformation of grains within the pore space. The temperature alteration may affect both elastic properties and porosity, however no change in porosity is expected due to a change in temperature in an isotropic homogeneous porous medium, since an isotropic thermal expansion would cause a proportional change in every linear dimension of the body. Palciauskas and Domenico (1982) defined the bulk thermal expansion coefficient of the rock as a volume average of the pore thermal expansion coefficient and the thermal expansion coefficient of the polycrystalline solid grains.

In this work the thermal induced behavior of rock will be considered by describing a rock mass as a continuum which consists of pores and cracks (fractures) and the thermoporomechanical parameters will be investigated. Only a limited amount of information is available to identify the effect of temperature on the complete stress-strain curve and and mechanical properties of intact rock. The limited test data do however agree with one's intuition, that an increase in temperature reduces the elastic modulus and compressive strength. It is believed that changes in microcracks population alter the elastic moduli, strength and transport properties. (Zang, 1993a) numerically investigated in closure pressure of thermally induced microcracks in a Feldspar-Quartz composite. The effective Young's modulus and Poisson's ratio decreased with increasing crack length when the load was parallel to the crack normal. In contrast, the Poison's ratio slightly increased with increasing crack length when the load was perpendicular to the crack normal. The thermal microcracks were categorized in terms of their crack length, aperture and aspect ratios int three major types:(1)] 1. grain-boundary cracks, 2. inter-granular cracks and 3. transgranular cracks Zang (1993b). The closing pressure was calculated to be between 30 to 50 MPa. It was concluded that normalized crack closing pressure can be used to estimate the residual stress stored in the composite after cracking.

1.4 Laboratory Measurements

The laboratory work employs the hydrostatic deformation of Flechtinger sandstone, an outcropping equivalent of Rotliegend reservoir rock at different temperature levels. The experiments were carried out in a conventional triaxial testing system (Figure 8(a), Mechanical Testing System, MTS) for which a description is given by Heiland (2003) and Blöcher et al. (2007). The triaxial testing system includes an axial load, a triaxial cell, confining pressure system, pore pressure system, acoustic transducers and computer for recording and processing of data.

The volumetric strain was measured by axial and circumferential extensometers shown in Figure 8(b). In order to minimize the inelastic effects, preconditioning (seasoning) was applied according to Hart and Wang (1995) and Blöcher et al. (2007). Preconditioning was consisted of cycling confining pressure between 0 to 60 MPa at a rate of 1 MPa/min. Afterwards, confining pressure was cycled between 2 to 55 MPa at a rate of 0.1 MPa/min to simulate stress changes due to production and reinjection of water from/into the reservoir. The drained regime characterizes the long-term mechanical behavior of saturated rock and prevails in slow loading conditions (Roeloffs, 1988). The stationary effective mean stress is calculated to be 40.3 MPa and a fluctuation of 10 MPa in pressure due to production and injection of water is expected. Thus, the range of experimental effective pressure covers the expected stress changes within the reservoir. Each cycle was composed of an upward ramp, a 60 minutes plateau to equilibrate pore pressure, and a downward ramp. Having completed each pressure cycle, temperature was increased step wise to 30, 60, 90, 120 and 140°C. The experimental temperature levels lies between the initial reservoir temperature (147°C) and planned injected water temperature (70°C) in the Groß Schönebeck geothermal reservoir. A low heating rate of 0.1-0.2 °C/min was employed because high heating rates generate spatial temperature gradients in the sample that may produce microcracks or microstructural damage.

The Flechtinger sandstone, an equivalent outcrop of Rotliegend reservoir rock in North German Basin was employed to perform the experiments. Flechtinger sandstone is a fine layered sandstone mostly composed of quartz, feldspar and carbonates. Rock specimens of 50 mm in diameter and 100 mm length were employed to investigate the relation between temperature, pressure, rock volumetric deformation and fluid mass content variations. Porosity of the cores was measured to be between 9% to 11% using the dry and immersed weights. Its unconfined compressive strength at saturated state (UCS) was experimentally determined as 56.7 MPa. This is in agreement with what has been previously reported by Zang (1997) and Heiland and Raab (2001). Zang (1997) determined the dry and saturated UCS of Flechtinger sandstone to be 96±13 MPa and 59±10 MPa, respectively. The tensile strength of the Flechtinger sandstone was measured by Hecht et al. (2005) to be about 3.9 MPa.

Different load paths can be applied to measure stress-strain curves, including directions (loading and unloading) allows for many types of elastic moduli to be defined. For example, Figure 9 explains the definition of axial and lateral strains and elastic moduli (Young's modulus E, Poisson's ratio ν) of a specimen under uniaxial load.

The poroelastic experiments are employed to characterize the volumetric response of the rock. The stress can be applied to the outer boundary of the rock specimen if the boundary is in contact with a fluid. By pressurizing the confining fluid a hydrostatic pressure will be exerted. If the strain-stress response is linear, the slope of the line gives the bulk modulus of the rock. In case of nonlinear response, the poroelastic parameters could be interpreted as secant or tangent (incremental) moduli. Three types of tests can be utilized to determine the poroelastic parameters as given in Table 1. Biot coefficient α would be equal or close to one when the bulk skeleton is compliant in comparison to the solid constituents. It would be less than one if the bulk skeleton is stiff or solid constituents are compressible. The Skempton coefficient B is inversely proportional to the Biot coefficient. The Skempton coefficient is the ratio of induced pore pressure to the change in applied pressure in unstrained conditions, i.e. no fluid is allowed to drain out. It is close or equal to one for fluid-saturated unconsolidated sands and close to zero for a porous rock filled with an incompressible fluid. It is typically between 0.5 to 1.0 for fluid-statured rock. The superscript o refers to initial conditions (unstrained).

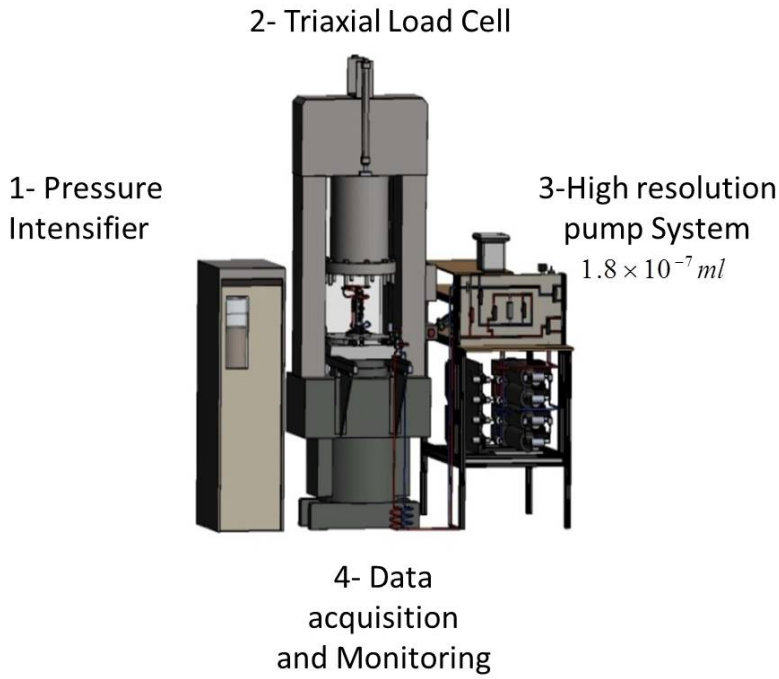

(a) A triaxial testing system was employed to carry out the experiments.

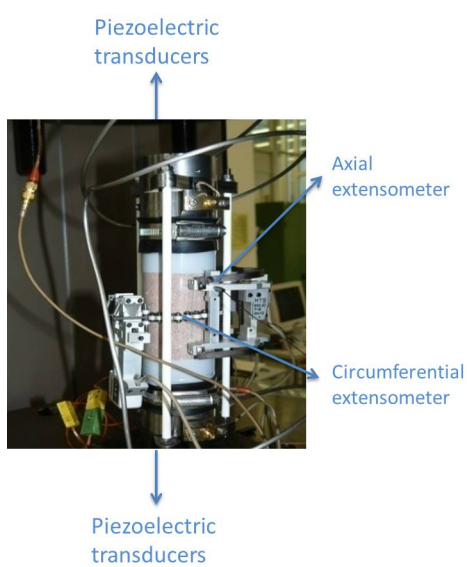

(b) Zoomed in picture of mounted specimen. The volumetric strain was measured by axial and circumferential extensometers.

Figure 8: The triaxial testing system includes an axial load, confining pressure system and pore pressure system.

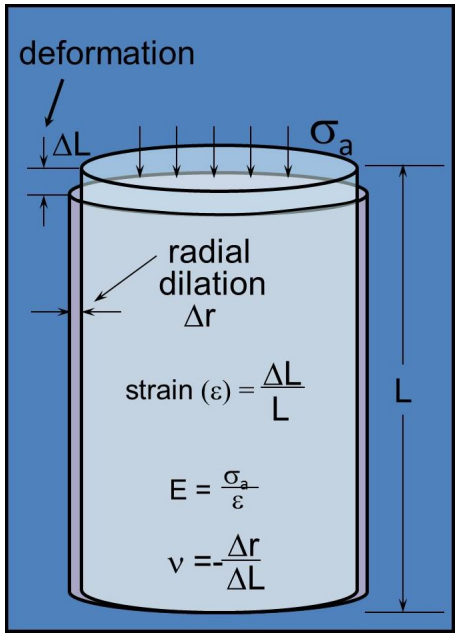

Figure 9: Elastic moduli and deformations defined under an uniaxial load

Table 1: Poroelastic tests

Test	Boundary conditions	Measurements	Poroelastic parameters
Drained	$P_c = P_c^0 + \Delta P_c$	$\Delta V_b/V_b$	K_d
	$P_p = P_p^0$	$\Delta V_f/V_b$	α
Undrained	$P_c = P_c^0 + \Delta P_c$	$\Delta V_b/V_b$	K_u
	$\zeta = 0$	$P_p \& P_c$	B
Unjacketed	$P_c = P_c^0 + \Delta P$	$\Delta V_b/V_b$	K_s

B	Skempton coefficient
K_d	drained bulk modulus
K_s	solid grain modulus
K_u	undrained bulk modulus
P_c	confining pressure
P_p	pore pressure
ΔP	change in pore pressure and confining pressure
V_b	bulk volume
V_f	pore fluid volume
α	Biot coefficient

A review on mechanical and fluid flow experiments in sandstone exhibits that elastic and transport properties of rock (e.g. porosity and permeability) are governed by the applied stress field and its geometry (David et al., 2001). A non linear stress-strain curve and permanent compaction can be recognized in mechanical behavior of sandstone rock (Brace, 1978). The other characteristic of non-linear response is pressure dependence of bulk modulus. Due to progressive crack closure, the slope of stress-strain curve and bulk moduli would increase and upon unloading the lower part of the stress-strain curve reveals a permanent deformation (Walsh, 1965). Moreover, the bulk volume and porosity will decrease upon loading and applied hydrostatic stress (David et al., 2001). Three different deformation regimes have been recognized in hydrostatic tests by David et al. (2001): the initial loading regime is characterized by a low bulk modulus, the transient regime is characterized by a linear evolution of porosity with stress and the third stage is identified by developing of inelastic deformation and pore collapse. Two empirical laws expressed the evolution of permeability; a decreasing exponential law and a power law (David et al., 2001).

The triaxial compaction tests, where the axial stress is higher than lateral stress, revealed a linear stress-strain curve at the start of the loading followed by an inelastic deformation in brittle regime. Heiland and Raab (2001) and Heiland (2003) studied the influence of stress, dilatancy, brittle deformation, strain rate, and formation of shear bands on permeability. Fortin et al. (2005) studied the strength of coupling between volumetric strain, elastic properties and permeability during the formation of compaction bands. They concluded that pore collapse pressure is governed by the composition of sandstone. They addressed pore collapse and grain crushing as mechanisms of increase and decrease in wave velocities, respectively. A new method for the evaluation of the porosity-permeability relationship is given by Ghabezloo et al. (2009) where the effect of creep on pore pressure and volume changes have been included.

The static elastic moduli of a porous rock can be derived from stress strain curves in rock mechanical tests and dynamic elastic moduli can be determined by acoustic wave velocity measurements. The static elastic moduli better represent the stress and strain changes within the reservoir, since the dynamic tests only capture the elastic part of the rock response (Yale and Jamieson, 1994). Therefore, it is required to correct the dynamic moduli to its equivalent static moduli. The quantitative correlation between static and dynamic moduli in combination with sonic log and seismic data provide the input elastic parameters to populate the geomechanical models. This geomechanical model can be employed to predict the induced thermoelastic and poroelastic stresses and the resulting deformation, caused by production and injection of water in underground reservoirs, e.g. geothermal reservoirs. The acoustic wave velocities in rocks mainly depend on bulk density (ρ_b) and fluid properties which can be characterized in terms of: porosity and pore geometry, stress state, temperature, saturation, pore pressure, fluid type, viscosity, lithology, clay content and frequency of the waves (Yale, 1985; Nur and Wang, 1989a).

The theory of drained deformation contains three poroelastic constants: the drained bulk modulus K_d, the shear modulus G, and Biot coefficient α, two of them, K_d and α, are measured at different temperature (Chapter 3). The first derivative of stress-strain curves are determined by tangent and mean value approach to investigate temperature dependence of drained bulk modulus at low and high confining pressures. Chapter 4 investigate on porosity evolution and employs the static and dynamic elastic moduli to investigate the rate of change of porosity with applied external pressure and temperature. Chapter 5 express the permeability evolution of Flechtinger sandstone at different temperatures. The permeability is measured by the steady state method and pressure drop is measured at a constant flow rate of 0.02 ml/min. The bulk moduli were fitted to exponential functions, aspect ratio distribution and crack porosity were determined for each stress-strain curve. A new model was suggested to estimate the pressure dependence of permeability which connects the permeability evolution to poroelasticity theory and porosity changes.

2 Summary

In this dissertation I focus on thermal effects on poroelasticity and transport properties. First, I made a reservoir model and simulate the reservoir behavior in macro scale to understand the mechanisms involved where I found that stress changes within the reservoir can be calculated if the appropriate hydraulic and poroelastic parameters are known. Afterwards, I performed several experiments using a conventional triaxial system and investigated in thermal effects on poroelastic and hydraulic properties.

In Chapter 2 I investigate in geomechanical response of the Groß Schönebeck geothermal reservoir by two approaches: reservoir simulation and analytical. I employ staggered approach to simulate the thermo-hydromechanical behavior of the reservoir. Then, I estimated analytically the magnitudes of induced thermoelastic and poroelastic stresses and the resulting reservoir deformation, caused by production and injection of water into Reservoir by assuming uniaxial boundary conditions. It is the effective stress which control both compressive and tensile failure and if the strains are high enough, the rock fails either in shear or in tension. The theoretical estimate of thermoelastic stress shows a much higher magnitude in comparison with poroelastic stress.

In Chapter 3 I study the thermo-mechanical behavior of Flechtinger sandstone experimentally and propose the physical mechanisms involved in elastic moduli evolution. The temperature effects on a granular rock such as Flechtinger sandstone can be described by interrelations between bulk modulus and thermal expansion coefficient. I explain the coupling between these physical properties based on thermodynamics. Both, stress dependence of the thermal expansion coefficient and path dependence of heat transfer processes influence the thermomechanical behavior of the rock. Hence, drained bulk modulus is strongly pressure dependent due to changes in contact area (Hertzian contact) and crack closure. The temperature dependence of drained bulk modullus is analyzed by considering tangent and mean value definition where two distinct regimes are found at low and high stresses. At low effective pressures, the temperature derivative of the drained bulk modulus is negative (more compliant), however at high effective pressures, it was positive (stiffer). The indirect measurement of the Biot coefficient rather describes matrix-bulk volume coupling, while the direct method highlights presence of the fluid and changes in micro-structure. Therefore, crack closure and thermal pressurization of trapped pore fluid are the mechanisms present in direct measurement of Biot coefficient. I distinguished two types of nonlinearity in mechanical behavior of granular rock, one due to Hertizan contacts and crack closure and the other due to the temperature and stress dependence of physical properties.

The experimental procedure in Chapter 4 is similar to Chapter 3. In addition to stress-strain data the acoustic velocities are also analyzed. I correlate the dynamic and static elastic moduli of the rock obtained at different temperatures by acoustic velocity measurements and mechanical tests. I find two inversion points, where the sign of the gradient changes, at effective pressures of 9 MPa and 25 MPa corresponds to the static and dynamic elastic moduli. Accordingly, the mechanical behavior of this sandstone can be categorized to low stress, a transitional, a high stress, and inelastic regimes. The porosity variation

had the same sign as the temperature dependence of the drained bulk modulus. Consequently, porosity variation decreased with an increase in temperature at low effective pressures and increased at high effective pressures.

Chapter 5 describes the interrelation between hydraulic and poroelastic properties (porosity, permeability) of Flechtinger sandstone. Moreover, I calculate the specific storage coefficient and crack porosity. I assumed that the rock has penny-shape cracks and I calculate the crack porosity by second derivative of the hydrostatic stress-strain curve. While the first derivative of stress-strain curves derives the bulk modulus, the second derivative can be assigned to crack aspect ratio and aspect ratio spectrum of pores with a given geometry. The bulk moduli are fitted to exponential functions, aspect ratio distribution and crack porosity are determined for each hydrostatic stress-strain curve. While, the pore volume of the cracks is not significant but controls the fluid flow pathways and consequently the permeability of the rock. Permeability is measured at a constant flow rate of 0.02 ml/min and keeping the downstream pore pressure at 1 MPa constant. A new model was suggested to estimate the pressure dependence of permeability which connects the permeability evolution to poroelasticity theory. The volumetric storage coefficient of the rock shows an inversion effect. The analyzing of unloading paths shows that crack porosity is increased and the distribution cracks aspect ratio moved towards lower aspect ratio and consequently lower effective pressure. The permeability decreased after each pressure cycle and rising the temperature due to inelastic porosity reduction.

Chapter 2

Originally published in the *Proceedings of Thirty-Sixth Workshop on Geothermal Reservoir Engineering*, 2011, Stanford University, Stanford, California

Induced stress in a doublet geothermal reservoir

A. Hassanzadegan, G. Blöcher, G. Zimmermann, H. Milsch, I. Moeck
Helmholtz Centre Potsdam - GFZ German Research Centre for Geosciences,
Telegrafenberg,
Potsdam, Brandenburg, D-1447, Germany
alireza.hassanzadegan@gfz-potsdam.de

Abstract

This paper presents the predicted magnitudes of induced thermoelastic and poroelastic stresses and the resulting reservoir deformation, caused by production and injection of water into Groß Schönebeck geothermal Reservoir. The Groß Schönebeck reservoir is a confined aquifer, located at about 4 km depth within the Lower Permian of the North East German Basin. The geological formation is composed from bottom to top of volcanic and siliciclastic rocks. Injection of cold water into a hot water reservoir will contract the rock, however the surrounding rock will constrain this contraction and thermal stress will be induced. This thermally induced stress not only influences the rock mechanical properties but also affects the poroelastic coefficients and consequently transport properties of the rock. While geomechanics in conventional reservoir simulator is often governed by change in pore compressibility and permeability as a function of pressure, a coupled mechanical and fluid flow simulator attempts to capture the alterations in reservoir properties (mainly porosity and permeability) due to changes in pressure, temperature and the induced stress and deformation.

In order to predict the thermal effects in reservoir scale, a static model which includes reservoir structure (geological units, faults and induced hydraulic fractures) was created. Thermo-hydro-mechanical analysis of the reservoir was performed for 30 years, the expected life cycle of the reservoir. A transition stress regime between normal faulting to strike-slip faulting is expected in Groß Schönebeck geothermal reservoir; hence different boundary conditions are employed. In particular, porosity and permeability were coupled through the changes in the strain and stress. The induced thermoelastic stress makes the minimum horizontal stress more tensile and pore pressure controls the effective stress. Fracturing would occur if the minimum principal effective stress becomes tensile and equal to tensile strength of the rock. A temperature decrease of 80° and an increase of 10 MPa in bottomhole pressure due to water injection, results in a change in minimum horizontal effective stress, such that it exceeds the tensile strength (3.9 MPa) of the rock.

1 Introduction

This study addresses the modeling of the geomechanical effects induced by reservoir production and reinjection and their influence on hydrothermal processes occurring in an enhanced geothermal system (EGS) during geothermal power production. While reservoir engineering attempts to provide answers on the extent of the reservoirs, the optimum production rate and the reservoir performance, reservoir geomechanics tries to capture rock-fluid interaction in terms of the stress and deformation and to characterize the failure of the rock. Geomechanical response may have a strong effect on the productivity and injectivity response of the reservoir. Due to pore pressure and temperature changes, the in situ stress will change and rock will deform. Coupling of deformation and pore pressure diffusion (Darcy's law) characterizes the mechanical

response of fluid-saturated porous rocks. Thermal stress may arise in a heated body either because of a non-uniform temperature distribution or external boundaries or a combination of both. A 30 years water cycling between production well and injection well was modeled using a 3D stress dependent reservoir simulator RGCOE (2010). The special focus will be on the modeling of the stress and displacement evolution during reservoir life cycle.

2 Geomechanical effects

In a doublet well system the in situ stress changes due to production and reinjection of cold water. Pore pressure alters the effective stresses acting on the rock. Two basic mechanics highlights poroelastic coupling: first, increase in pore pressure will dilate the rock and second a rapid loading or compression will increase the pressure in trapped fluid (undrained conditions). In drained conditions the pore pressure is dissipated according to the diffusion law. Furthermore, a pore pressure gradient results in seepage forces at steady state fluid flow. Seepage forces induce stresses within the porous body that should be take into account in the equilibrium of the effective stresses (Detournay and Cheng, 1993). It is the effective stress which controls both compressive and tensile failure. If the strains are high enough, the rock fails either in shear or in tension. Three stress regimes can be defined if the rock fails in shear: Normal fault regime, strike slip fault and thrust (reverse) fault (Fjaer et al., 1992). Segall and Fitzgerald (1998) investigated stress changes in hydrocarbon and geothermal reservoirs. According to this study, thermal stresses may exceed poroelastic stresses by a factor of 8 or more. This indicates that thermoelastic behavior of rock cannot be ignored. Stress changes within the reservoir can be calculated if the appropriate hydraulic and poroelastic parameters are known.The following equation can be employed to quantify the ratio between thermoelastic (σ_T) and poroelastic (σ_P) stresses due to injection and production in geothermal reservoirs:

$$\frac{\sigma_T}{\sigma_P} = \frac{3\beta K \Delta T}{\alpha \Delta P} \tag{1}$$

where α is Biot coefficient K is the bulk modulus, β is the linear thermal expansion coefficient and ΔT and ΔP are the change in temperature and pressure respectively. Uniaxial deformation assumption (sides and bottom of reservoir constrained) has been one of the most popular approaches to model the geomechanical behavior of reservoirs. Assuming uniaxial boundary conditions where no horizontal strain occurs the ratio of changes in horizontal stress due to changes in reservoir pressure and temperature can be estimated:

$$\frac{\Delta S_h}{\Delta P} = -\frac{1-2\nu}{1-\nu}\alpha \tag{2}$$

where S_h is the minimum horizontal stress, ν is the Poisson's ratio and the right hand side is equal to poroelastic stress coefficient. Thermoelastic stress and strain evolution due to temperature variations in uniaxial boundary conditions can be estimated according to the following equation:

$$\sigma_T = \frac{E\beta\Delta T}{1-\nu} \tag{3}$$

where E is the Young's modulus and $\frac{\beta E}{1-\nu}$ is the thermoelastic stress coefficient η_T. The volumetric strain would be:

$$\varepsilon = \frac{1+\nu}{1-\nu}\beta\Delta T \tag{4}$$

An increase in temperature causes an increase in volume and results in compressional thermoelastic stress. A decrease in temperature causes a reduction in volume and results in tensile stresses. Thermoelastic effects predominate in case of increase in rock mechanical stiffness, which could be due to an increase in

confining pressure. The Biot effective coefficient is defined as the contribution of pore pressure to the total stress, i.e. the efficiency of pore fluid in counteracting to the total applied stress.

$$\overline{\sigma} = \sigma - \alpha P_p \tag{5}$$

Rock will fail in tensile mode if the minimum effective principal stress becomes tensile and equal to the tensile strength of the rock (Fjaer et al., 1992):

$$\overline{\sigma} = \sigma_3 - \alpha P_p \gg \sigma_{tensile} \tag{6}$$

3 Groß Schönebeck Geothermal Reservoir

The Groß Schönebeck geothermal reservoir is a research site in the North German Basin. The technical feasibility of geothermal power production from a deep low-enthalpy reservoir will be evaluated by means of a doublet system consisting of a production and injection well. The research strategy and challenges while drilling the wells have already being discussed in previous works Legarth et al. (2005), Huenges et al. (2007) and Kwiatek et al. (2008).

An existing gas exploration well (GrSk3) was reopened and deepened up to a depth of approximately 4,300 m. Several hydraulic stimulations have been carried out in this well to serve as an injection well (Legarth et al., 2005). A deviated production well (GrSk4) has been drilled in the direction of minimum horizontal stress. Both wells are placed in one drilling site at a distance of 28 meters at surface. At the top of the reservoir the wells have a distance of 241 m. This distance is increasing to 470 meters by increasing the inclination of production well progressively from 18 to 48°. Three stimulation treatments have been performed to enhance the productivity of the production well. The induced hydraulic fractures have been propagating perpendicular to the well path (Zimmermann et al., 2007). The Groß Schönebeck reservoir is a faulted reservoir. The reservoir is located at a depth of 3700 to 4300 m subsea. The fault pattern was interpreted by 2D seismic data. The trend of major fault is N-W and minor faults are characterized by a NE-N direction (Figure 1).

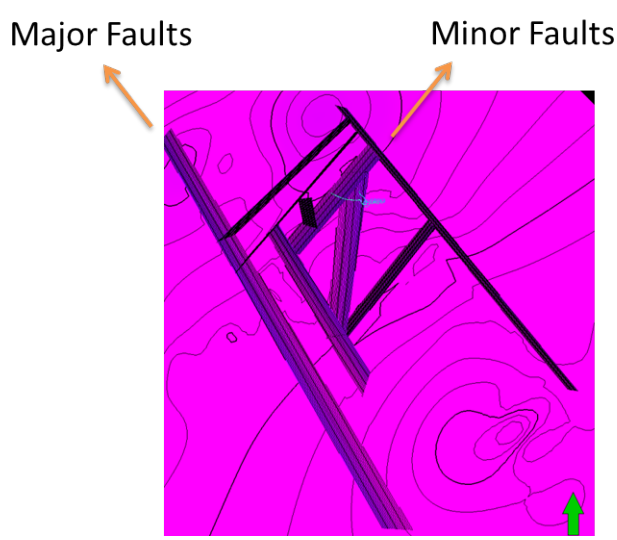

Figure 1: Top view of the fault pattern. Major faults have a trend of NW and minor faults have a trend of NE-N.

3.1 Reservoir geology

The reservoir formation consists of two different rock types: sedimentary sandstones and volcanic rocks. Lower Permian siliciclastic sediments and volcanic are widespread strata throughout Central Europe forming deeply buried aquifers in the North German Basin with formation temperatures of up to 150C. The average depth of these strata is 4000 m. The main reservoir interval is the sandstones of the Upper Rotliegend (Dethlingen Formation). A shale cap rock covers the reservoir. Underneath, the Hannover formation is placed which has a high concentration of silts and mudstones. The Dethlingen formation consists of three sub layers: (1) Elbe alternating sequence, mostly consists of silt to fine grained sandstone. (2) Elbe base sandstone- II composed of fine grained sandstone (3) Elbe base sandstone -I, consists of fine to middle grained sandstone. The Havel formation is the most lowest sedimentary geological unit, consisting of mainly conglomerates. Beneath the sedimentary strata, a volcanic formation is placed.

3.2 Initial conditions

The pore pressure was determined by production logs at stationary condition to be 43.8 MPa at a depth of 4220 mss (Legarth et al., 2005). The reservoir fluid is saline water with a density of 1109 kg/m3. The gas phase is dominated by N_2 (80 vol. %) and CH_4 (15 vol. %) which is typical for the natural gas composition found in the Rotliegend sandstones. The gas-water volume ratio in the sampled fluids was approximately 1 at ambient conditions. The temperature gradient in the reservoir is such that the Hannover formation has a temperature of 138°C and temperature increases continuously to 147°C for the volcanic rocks (Figure 2).

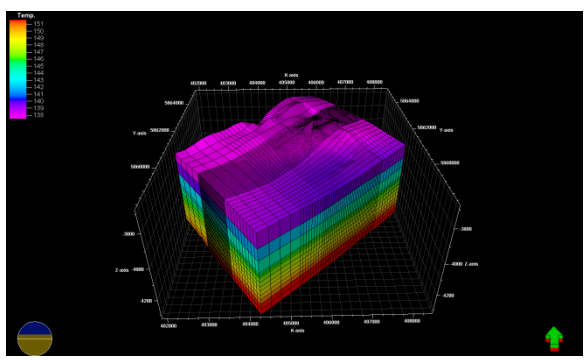

Figure 2: Reservoir temperature varies between 137°C at the cap rock to 151°C, at bottom hole.

3.3 In situ stress state

The in situ stress state was determined for this Lower Permian (Rotliegend) reservoir by an integrated approach of 3D structural modeling, 3D fault mapping and stress ratio definition based on frictional constraints, and slip-tendency analysis (Moeck et al., 2008). The azimuth of the maximum horizontal stress was obtained by analysing the acoustic borehole televiewer (ABF14) images and formation microimages (FMI) to be 18.5±3.7° (Holl et al., 2003). The minimum horizontal stress S_h magnitude is evaluated by hydraulic fracturing to be 54 MPa. The vertical stress S_v was estimated by considering the average weight of the overburden strata and the thickness of the rock units. An equivalent density of 2500 kg/m3 for the entire overburden was calculated. Consequently, vertical stress is equal to 100 MPa at a depth of 4100 meter. The most uncertain component of stress tensor is maximum horizontal stress S_H. Jaeger et al. (2007) derived the ratio between effective principal stresses as a function of sliding friction coefficient, which can be employed to give the bounds on S_H . Moeck et al. (2008) employed this approach and

stated that the maximum horizontal stress is equal or less than 0.78 S_v in normal faulting regime. In strike slip faulting regime it is equal or less than vertical stress S_v. A value of 95-100 MPa is confirmed by core tests and numerical modeling. Therefore, the stationary effective mean stress can be calculated by:

$$\overline{\sigma}_m = \frac{1}{3}(S_v + S_h + S_H) - P_p \tag{7}$$

to be 40.4 MPa. The effective Terzaghi stress is defined as $S' = S - Pp$, where Pp is pore pressure and S is a component of principal stress tensor. The NE-trending faults carry the highest ratio of shear to normal stresses. These faults exhibit a critically stress state in the sandstones and a highly stressed state in the volcanic layer. Since critically stressed faults are described as hydraulically conductive (Barton et al., 1995), these NE-N trending faults are expected to be the main fluid pathways in the reservoir (Moeck et al., 2008). During the hydraulic fracturing of production well microseismicity was monitored by a three-axis geophone, installed in the injection well (GrSk3) at a depth of 3735 m. The orientation of the seismic events is approximately in the north-south direction and hence similar to the maximum horizontal stress direction (Kwiatek et al., 2008).

4 Modeling

There are different approaches to analyze the geomechanical effects in a geothermal reservoir, categorized as analytical models, semi-analytical models and numerical models. Semi-analytical models are those which use analytical solutions including numerical integration procedures. Segall and Fitzgerald (1998) studied simple geometric reservoirs by employing semi analytical solutions to evaluate stress changes both within a reservoir and in the surrounding rocks. To analyze more complicated reservoirs, accounting for more realistic geometries and rock/fluid behavior, the use of numerical models is required. Moeck et al. (2008) provided a 3D regional model which includes the surface horizons, fault geometries and well trajectories. Blöcher et al. (2010) studied the coupling between hydrothermal processes by employing a finite element simulation. They have captured the structure of the reservoir using unstructured grids consisting of triangular prisms. His model captures the coupling of various petrophysical parameters and it includes pressure and temperature dependency of the heat conductivity, heat capacity, fluid density and viscosity. In this paper the corner point grid geometries capture the reservoir structure as it is convenient in many reservoir simulators. In order to construct the static model, horizon surfaces, well trajectories, faults and hydraulic induced fractures were implemented into the Flogrid-Petrel software and reservoir structure was captured (Figure 3). The faults are described using directional transmissibility multipliers for the fluid flow problem. The reservoir model was based on a single porosity description for fluid flow. The hydrothermal modeling was performed by employing Eclipse^{TM} software (GeoQuest, 2010). The Thermo-hydro-mechanical (THM) modeling was performed by employing Visage^{TM} (RGCOE, 2010).

4.1 Input parameters

In thermo-hydro-mechanical modeling different processes are involved and therefore different kind of material properties are required to characterize the reservoir. These properties can be categorized to hydraulical, thermal and mechanical properties. The highest reservoir permeability of 50 mD (1 mD is equal to 10-15 m2) was determined by laboratory experiments on core samples from of the Elbe basis sandstone (Trautwein and Huenges, 2005). Holl et al. (2003) confirmed these values by log interpretation. Milsch et al. (2009) studied the geochemistry of the reservoir fluid under initial pressure, temperature and fluid salt content. He concluded that matrix permeability is not influenced by long term production. A constant permeability of 2 mD (150 °C and 45 MPa effective mean stress) was measured. An overview of thermal parameters of the North German basin is given by Lotz (2004) and Gehrke (2006) which can be summarized in Table 1.

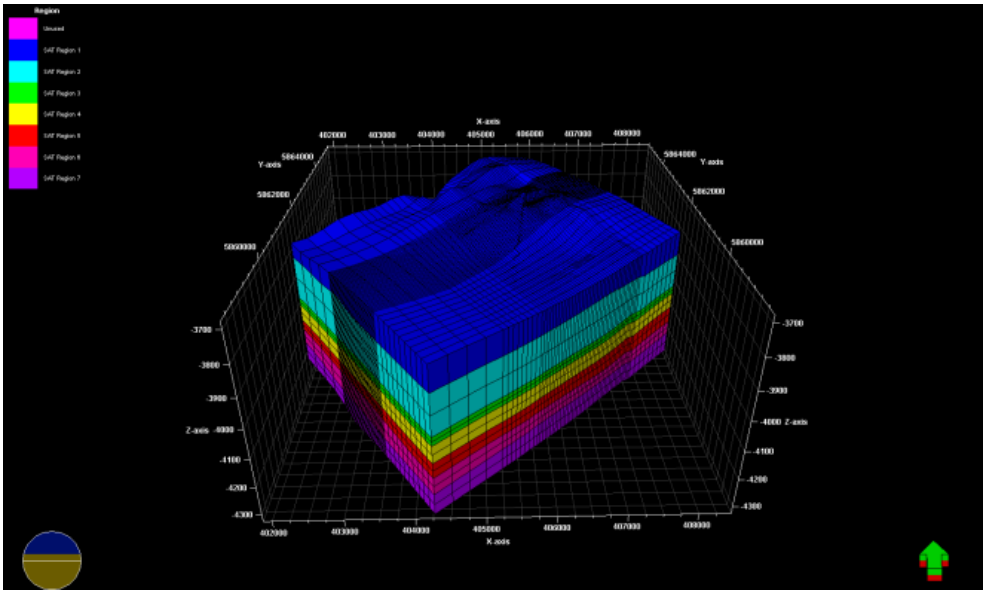

Figure 3: Reservoir structure build in Petrel. The boundary of models following the northwest major faults.

Table 1: Hydrothermal properties

Geological unit	Permeability	Porosity	Heat conductivity	Heat Capacity
	[mD]	[%]	[kj/(day*m*K)]	[kj/(day*m*K)]
Hannover	0.05	1	164.2	2438
Elbe alt.	12.5	3	164.2	2438
Elbe II	25	8	250.6	2438
Elbe I	50	15	241.9	2438
Havel	0.2	0.002	259.2	2650
Volcanic	0.2	0.5	198.7	3657

4.2 Mechanical Properties

When a material behaves linear elastically, two elastic moduli characterize its stress- strain behavior (e.g. Young's modulus and Poison's ratio) however; the constitutive equations in poroelasticity are described by four independent material properties (drained and undrained bulk moduli are also required). The elastic moduli of Rotliegend sandstone were investigated in the laboratory by employing an outcrop rock, equivalent to the reservoir rock (Flechtinger sandstone). Young's modulus, Poison's ratio and unconfined strength of the Flechtinger sandstone were obtained by performing a drained uniaxial test. Young's Modulus and Poisson's ratio were obtained at 50% axial peak stress. The deviation from elastic behavior (Yield point) was observed to be at 38 MPa. Flechtinger sandstone has a bulk modulus of 15.9 GPa. Not

Table 2: Mechanical properties of Flechtinger sandstone, an equivalent outcrop to reservoir rock, were measured under drained uniaxial condition.

Poisson's ratio	Young Modulus	Peak stress	Yield point	Tensile Strength
[-]	[GPa]	[MPa]	[MPa]	[MPa]
0.31	18	56.7	38	3.9

only deformation of Flechtinger sandstone is of interest but also its strength. Hecht et al. (2005) stated that strength properties mostly depend on the compositional order; however primary rock properties such as density and porosity depend on the grain distribution and the cementation grade of the rock. The tensile strength of the Flechtinger sandstone was measured to be about 3.9 MPa.

5 Simulation results

5.1 Hydro-thermal modeling

The hydro-thermal simulation was carried out using Eclipse 100. This hydrothermal reservoir model led to a total of 60*54*13 grid cells. The model reservoir includes one injection and one production well. In ECLIPSE 100 an energy conservation.equation is solved at the end of each converged time step, and the grid block temperatures are updated. The reservoir fluid defined to be pure water and a deterministic approach was employed to populate the reservoir properties. The planned production rate is 20 l/s. The simulation results show that temperature perturbation due to injection does not reach the boundaries of the model. The temperature front propagates through the reservoir, immediately after reinjection of the 70°C cold water into the reservoir. Fig. 4(a) shows the transition of the temperature front at different observation points between injection and production wells in the Dethlingen formation. Fig. 4(b) shows the final temperature field after 30 years of production and injection. The temperature close to the injection well will drop quite fast to 70°C. The thermal breakthrough occurs after 30 years of water cycling. The pressure profile between injection and production well and deviation of pressure from equilibrium are shown in Figures 5(a) and 5(b).

5.2 Thermo-hydro-mechanical coupling

The geomechanics module solves for the force equilibrium of the formation and calculates the displacements (volumetric dilation and compression). There are different approaches to solve and couple the partial differential equations which produce the fluid pressure, temperature and displacement field. For example, in one way coupling the changes in fluid pressure field produce stresses and strains but changes in stress and strain field are assumed not to influence on fluid pressure. Therefore, pressure field can be solved independently of the strain stress field. The same coupling approach can be described for one

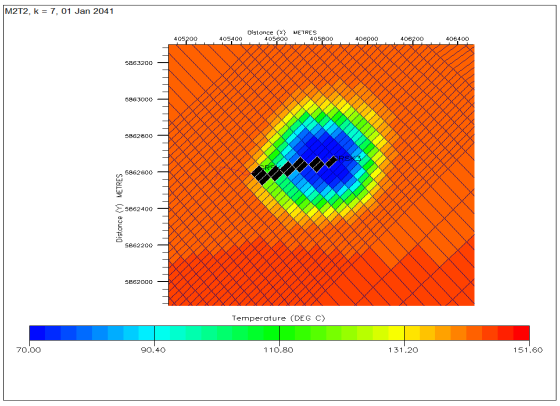

(a) A top view of temperature profile at the end of the simulation.

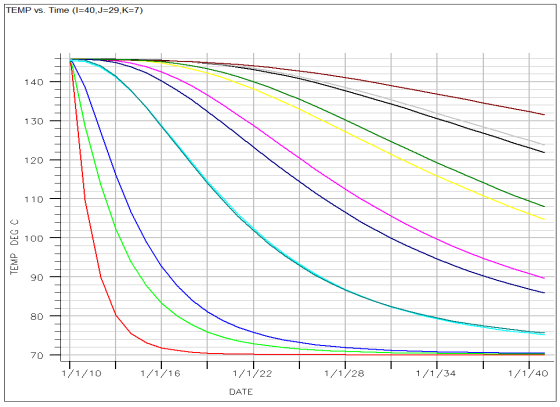

(b) Temperature profile vs. time at observation points shown in Fig.4(a).

Figure 4: Temperature front develops by diffusion and drops relatively fast close to the injection well.

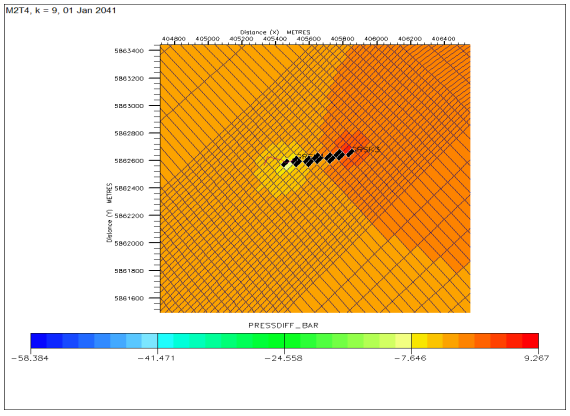

(a) Pressure profile between injection and production well at top of the Deth-Elbe Base sandstone II.

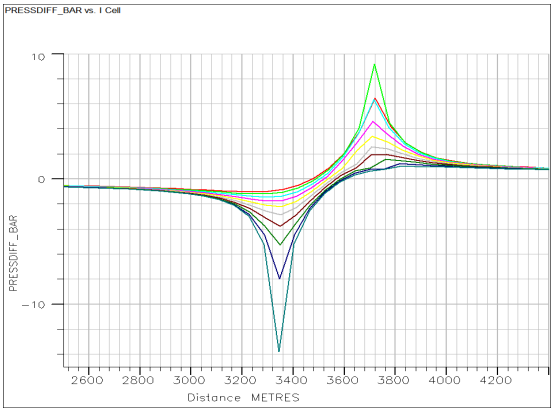

(b) Pressure as a function of distance.

Figure 5: Deviation of pressure from equilibrium across the injection and production wells

way thermoelasticity coupling. ECLIPSE^{TM} 100 calculates pore-pressure and temperature distributions which are used in the stress calculations to determine equilibrium levels of effective stress. In Visage^{TM} a staggered scheme is implemented which solves for stresses and updates the hydraulic properties as frequented by user (permeability or porosity). The finite element grid for the stress calculation is the same grid that is used when calculating fluid flow. Compressive stress is negative. The current model solves for the temperature distribution, however does not take into account the thermal stresses. The poroelastic and thermoelastic stresses were estimated based on the laboratory data. An analytical calculation of stress variation is presented in Table 3. A higher pore efficiency of 0.9 is required to make the horizontal minimum stress tensile and higher than strength of the rock. In some cases it is also essential to analyze

Table 3: Estimates of in situ stress changes.

ΔP_p	K	α	η_p	η_T	S_h
[MPa]	[GPa]	[-]	[MPa]	[MPa]	[MPa]
0.1	9.3	0.64	-0.35	16.7	-10.2
10	8.6	0.7	-3.85	15.4	-5.7
10	8.6	0.9	-4.95	15.45	3.92

the geomechanical behavior outside of the target fluid reservoir. For instance, lateral continuity of the overburden can influence estimates of the ground movement above the reservoir all the way to the surface. In this case, two different grids can be assigned: One which covers the volume of interest with regards to fluid flow and heat transfer (within the reservoir) and one which covers the volume of interest (extended or embedded grids). Poroelastic and thermo-elastic contraction or expansion of the zone from which the fluids are produce or injected changes the shear and normal stress in the reservoir. It also influences where the fluid mass content does not change. The geometry of the geomechanical model including overburden, underburden and sideburden is shown in Figure 6. The most pronounced stress changes are in the reservoir rock and in the vicinity of production well (Figure 7). The fluid reservoir considered here is of 3km $\times$ 4 km $\times$ 0.3 km in size which is surrounded by 8 overburden layers on top and 5 underburden layers at the bottom (both 3.7 km). The sideburden layers are extended up to 6 km.

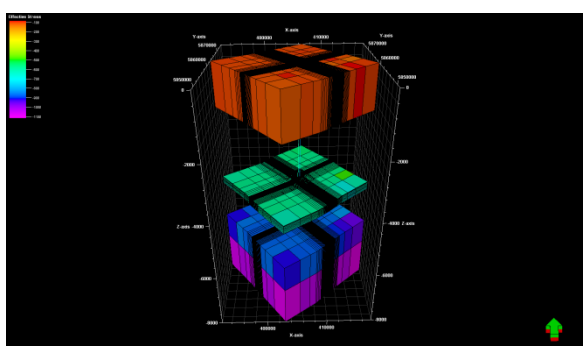

Figure 6: Embedded reservoir model has 66$\times$60$\times$23 cells.

In the surrounding rock the stress changes are much lower (Figure 8). In contrast, vertical elastic displacement is more pronounced at the most upper layer of the reservoir (Figure 9). The results show a maximum subsidence of 1.75 mm and a maximum uplift of 1.5 mm in the cap rock layer. These values in the volcanic rock are in the order of 0.5 mm (subsidence) and 0.05 mm (uplift). Figure 10 shows the vertical displacement at the end of simulation in volcanic layer. At the ground surface the displacement

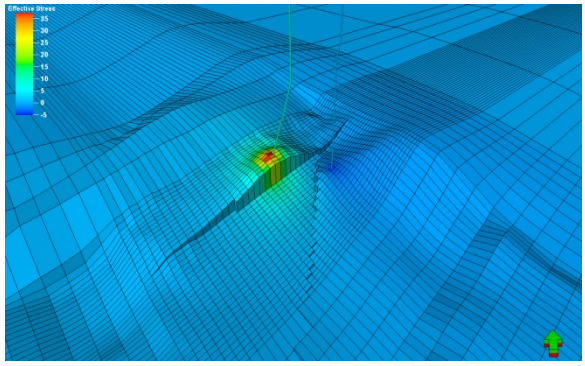

Figure 7: Maximum vertical effective stress change (bar) was observed at completion points in the volcanic rock.

of the rock is in order of micrometres (Figure 11).

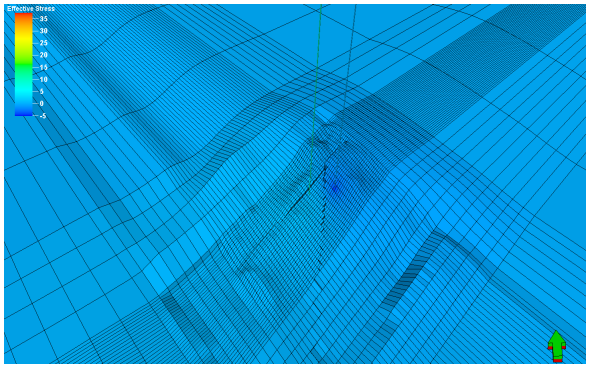

Figure 8: The change of vertical effective stress (bar) at the cap rock due to low porosity is negligible.

6 Conclusion

The thermo-hydromechanical modeling of a geothermal reservoir was achieved by employing staggered approach. The results show that effective vertical stress is expected to increase up to 3.5 MPa around the production well. It will decrease 0.5 MPa in the vicinity of injection well. Also a temperature change of 80°C occurs around the injection well. At this condition a high contribution of pore pressure in total stress (Biot coefficient) is required to fracture the rock, i.e. a Biot coefficient of 0.9. The maximum vertical effective stress changes takes place close to production well (especially at volcanic rocks), while the highest vertical displacement would occur at the cap rock. The theoretical estimate of thermoelastic stress shows a much higher magnitude in comparison with poroelastic stress.

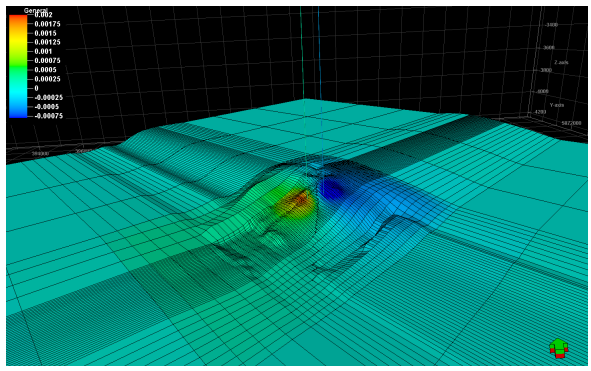

Figure 9: Vertical elastic displacement at the most upper layer of the reservoir (cap rock) at the end of the simulation.

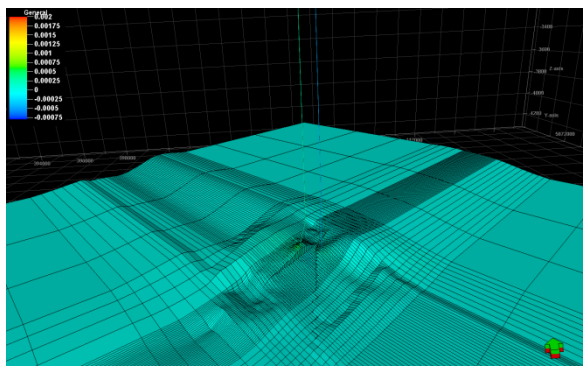

Figure 10: Vertical elastic displacement at the most lowest layer of the reservoir (volcanic rock) at the end of the simulation.

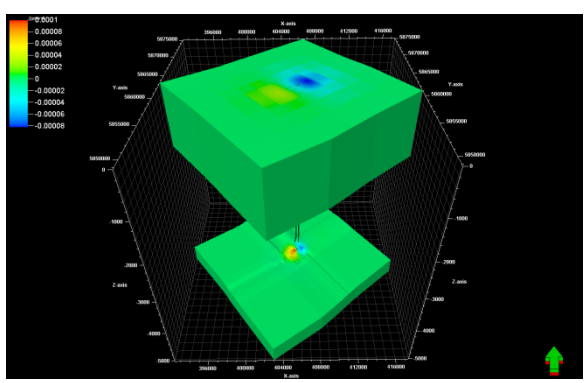

Figure 11: vertical deformation due to injection and production at the surface and below the reservoir (subsidence and uplift).

Chapter 3

Originally published in the *International Journal of Rock Mechanics and Mining Sciences*, 2012, 49, 94–104

Thermoporoelastic properties of Flechtinger sandstone

A. Hassanzadegan, G. Blöcher, H. Milsch, G. Zimmermann

Abstract

This research addresses the thermomechanical response of a saturated sandstone in a geothermal reservoir. Four experiments were performed using a triaxial testing system to investigate thermal effects on poroelastic parameters of Flechtinger sandstone, an outcropping equivalent of the (Rotliegend) reservoir rock. In drained experiments, confining pressure was cycled, pore pressure was maintained constant and temperature was increased step-wise. The temperature dependence of the drained bulk modulus differed at low and high effective pressures. The unloading drained bulk modulus increased from 10.25 GPa to 11.74 GPa with increasing temperature from 30°C to 120°C at high stresses and decreased from 3.39 to 3.05 GPa at low stresses. The Biot coefficient decreased with increasing effective pressure and temperature. The inelastic behavior of the rock, the interrelation between thermal expansion coefficient and bulk modulus, and the path dependence of heat transfer processes govern the temperature effect on granular rock and changes in pore geometry.

1 Introduction

The thermomechanical response of saturated porous rock is of interest in environmental geomechanics, greenhouse gas sequestration, oil and gas production and geothermal energy. Due to injection of cold water, pore pressure and temperature will change within the reservoir which results in a variation of the in situ stress. The stress changes within the reservoir can be evaluated if the appropriate poroelastic and thermoelastic parameters are known (Segall and Fitzgerald, 1998). Temperature effects not only change the in situ stress within a doublet geothermal system such as Groß Schönebeck (Huenges et al., 2006; Blöcher et al., 2008), but also induce nonlinearity due to the temperature dependence of physical properties. Of principal importance are bulk modulus and thermal expansion coefficient and their changes with pressure and temperature. In both linear theories of poroelasticity (Biot, 1941; Rice and Cleary, 1976; Detournay and Cheng, 1993) and thermoporoelasticity (Palciauskas and Domenico, 1982; McTigue, 1986) physical properties are constant; however, these properties are temperature and pressure dependent for a granular rock such as Flechtinger sandstone. The Flechtinger sandstone is a Lower Permian (Rotliegend) sedimentary rock, an outcropping equivalent of the Groß Schönebeck reservoir rock (Heiland, 2003).

Handin et al. (1963) studied the influence of pore pressure in combination with confining pressure and temperature by employing compression tests. Pore pressure influenced the ultimate strength, the deformation mechanisms involved and porosity. Hart and Wang (1995) measured poroelastic moduli of Berea sandstone as a function of confining pressure and pore pressure. Charlez and Heugas (1992) presented the thermoporoelasticity formulation and determined the Biot coefficient by measuring drained and undrained bulk moduli of Vosges sandstone at 1 and 15 MPa confining pressures. The Biot coefficient increased with decreasing effective pressures. Bouteca and Bary (1994) experimentally investigated Biot's semilinear theory by performing drained experiments at different pore pressures. Somerton (1980)

performed drained experiments at different temperatures. He concluded that drained bulk moduli and porosity were decreased by increasing temperature.

Handin and Hager (1957) studied the thermomechanical behavior of the Barns and Oil Creek sandstones. Heating reduced the strength and yield stress of the dry sandstones and induced little or no permanent deformation. Blacic et al. (1981) investigated in thermomechanical properties of Gallesville Sandstone while increasing the temperature from 37 to 204 °C and effective pressure from 0 to 31 MPa. The Young's modulus increased with increasing temperature and Poisson's ratio decreased (at high stresses). In contrast, the Young's modulus of the Champenay, Voltzia and Merlebach sandstones decreased with increasing temperature from 25 to 600 °C at zero confining pressure (Homand-Etienne and Houpert, 1987).

The aim of this research is to experimentally quantify the influence of temperature and pressure (Terzaghi effective pressure) on the poroelastic properties such as Biot coefficient and drained bulk modulus. Therefore, drained experiments were performed at different temperature levels. Meanwhile, confining pressure was cycled to simulate stress changes due to production and reinjection of water from/into the reservoir. The drained regime characterizes the long-term mechanical behavior of saturated rock and prevails in slow loading conditions (Roeloffs, 1988). In the following, nonisothermal poroelasticity formulations and different methods to measure Biot coefficient are described. This is followed by a short review of physical properties and their pressure and temperature dependence. Then, the experimental procedure and data processing approach is given. Finally, the results of the experiments are presented, interpreted and discussed.

2 Nonisothermal poroelasticity

The impact of temperature on the hydromechanical behavior of the rock can be described by employing thermoporoelastic theory (Charlez and Heugas, 1992). A temperature change in drained conditions results in rock thermal expansion and changes its fluid mass content (Guéguen and Boutéca, 2004; Zimmerman, 2000):

$$\varepsilon = \frac{P_e}{K_d} - \beta_b(T - T_o) \tag{1}$$

where ε is the volumetric strain, T_o is the reference temperature, $T - T_o$ is the temperature change, β_b is the bulk thermal expansion, and K_d is the drained bulk modulus. Following the convention used in rock mechanics the compression is positive and expansion is negative. Accordingly, the effective pressure P_e and effective stress σ_{ij}^{eff} are defined by the following equation:

$$P_e = P - \alpha p \tag{2}$$

$$\sigma_{ij}^{eff} = \sigma_{ij} - \alpha p \delta_{ij} \tag{3}$$

where P is the hydrostatic pressure, p is the pore pressure, σ_{ij} are the components of the total stress tensor and δ_{ij} is Kronecker delta. The Biot coefficient α is defined as the efficiency of pore fluid in counteracting the total applied stress. The concept of effective pressure in different applications has been reviewed and clarified by (Berryman, 1992; Guéguen and Boutéca, 1999). Zimmerman et al. (1986) provide the theoretical justification for the dependence of the effective bulk modulus on the Terzaghi effective pressure $(P - p)$. Bouteca et al. (1993) and Hart and Wang (1999) have reported similar experimental results. Therefore, here the pressure or stress dependency refers to the Terzaghi law which can be derived from energy consideration (thermodynamics) (Guéguen and Boutéca, 1999).

The thermal expansion coefficient of fluid β_f and pore thermal expansivity β_p describe thermal effects on fluid mass variation β_m:

$$\beta_m = \frac{1}{m}\left(\frac{\partial m}{\partial T}\right)_{P,p} = \frac{1}{\rho_f}\left(\frac{\partial \rho_f}{\partial T}\right)_{P,p} + \frac{1}{\phi}\left(\frac{\partial \phi}{\partial T}\right)_{P,p} = \beta_p - \beta_f \tag{4}$$

where ρ_f is fluid density, ϕ is the porosity, m is the fluid mass content (M_f) per reference rock bulk volume (V_b^o) and has the same dimension as density. In general β_p is smaller than β_f which results in a negative β_m and a decrease of fluid mass with increasing temperature (Palciauskas and Domenico, 1982). The pore fluid mass content varies not only as a result of changes in temperature but also due to induced pore pressure (Skempton effect) and rock deformation as described by Guéguen and Boutéca (2004):

$$\Delta m = m - m_o = -\alpha\rho_f^o\varepsilon + \frac{\alpha\rho_f^o p}{BK_u} + (\phi\beta_m - \alpha\beta_b)\rho_f^o(T - T_o) \tag{5}$$

where ρ_f^o is fluid density at reference state, B is the Skempton pore pressure coefficient, the ratio of a change in pore pressure due to changes in confining pressure at undrained conditions, and K_u is the undrained bulk modulus.

2.1 Biot coefficient

Franquet and Abass (1999) presented three experimental methods to measure Biot coefficient; direct, indirect and failure methods. Direct and indirect methods were employed to measure the Biot coefficient here. In the indirect method (Eq.6), two experiments are required: a hydrostatic compression test on a jacketed specimen to measure the drained bulk modulus of the framework K_d and a hydrostatic compression test on an unjacketed specimen to measure the bulk modulus of the solid grains K_s.

$$\alpha = 1 - \frac{K_d}{K_s} \tag{6}$$

The direct method (Eq.7) employs a jacketed specimen and the change in pore volume V_p and volumetric strain ε are measured:

$$\alpha = (\frac{\partial\zeta}{\partial\varepsilon})_p = 1/\rho_f^o(\frac{\partial m}{\partial\varepsilon})_p \tag{7}$$

$$\partial\zeta = \frac{m - m_o}{\rho_f^o} = \frac{1}{\rho_f^o}\left(\frac{M_f - M_f^o}{V_b^o}\right) \tag{8}$$

where ζ is the volumetric fluid content and dimensionless, m_0 is the initial fluid mass content (M_f^o) per reference bulk volume (V_b^o) in unstrained and ambient temperature conditions. Zimmerman (2000) described the relation between the change in pore volume (dV_p) and the change in volumetric fluid content (ζ):

$$\frac{dV_p}{V_b^o} = \frac{1}{V_b^o}\frac{dM}{\rho_f} - \frac{\phi}{K_f}dp \tag{9}$$

where K_f is the fluid bulk modulus. Eq.9 shows that the fluid exchange within the pore volume could be due to a mass transfer as a result of changes in the bulk volume or fluid compression and expansion as a result of changes in pore pressure (in the absence of any source or sink). At drained conditions, the change in pore volume and the changes in volumetric fluid content are only due to change in the bulk volume and equal.

$$\alpha = 1 - \frac{K_d}{K_s} = \phi\frac{K_d}{K_p} = \frac{\phi V_b}{V_p}\left(\frac{\partial V_p}{\partial V_b}\right)_p = \left(\frac{\partial V_p}{\partial V_b}\right)_p \tag{10}$$

where $K_p = -V_p\left(\frac{\partial P}{\partial V_p}\right)_p$ is the effective bulk modulus of the pore volume. Biot coefficient would be equal or close to one when the bulk skeleton is compliant in comparison to the solid constituents. It would be less than one if the bulk skeleton is stiff or solid constituents are compressible. Charlez and Heugas

(1992) measured the Biot coefficient by performing drained and undrained tests and by determining Skempton's coefficient, undrained and drained bulk moduli (Eq.11):

$$\alpha = \frac{1}{B}[1 - \frac{K_d}{K_u}] \tag{11}$$

The strength of poroelastic coupling is a product of Biot coefficient and Skempton coefficient (Zimmerman, 2000). Thus, the temperature effects in poroelasticity can be viewed as the effects of temperature at drained and undrained conditions. The effect of temperature on pore pressure is characterized by the thermal pressurization coefficient λ at undrained conditions:

$$\lambda = \frac{\beta_f - \beta_p}{1/K_f + 1/K_p} \tag{12}$$

Eq.12 highlights that the difference in thermal expansion coefficients of pore fluid β_f and pore volume β_p is responsible for thermal pressurization. Ghabezloo and Sulem (2008) experimentally investigated the thermal pressurization coefficient λ of a saturated rock (Eq.12). They concluded that the higher the temperature and effective stress, the higher is the thermal pressurization coefficient. The effect of temperature at drained condition is investigated here. The physical properties of the porous rock are defined in terms of effective properties of representative elementary volume (REV) due to a heterogeneity at the microscale. The complete thermo-physical description of an isotropic elastic solid rock requires knowing the isothermal bulk modulus K, the thermal coefficient of expansion β, and their pressure and temperature derivatives (Garaia and Laugier, 2007). The pressure derivative of the thermal expansion coefficient and the temperature derivative of the isothermal bulk modulus are not independent from each other (Garaia and Laugier, 2007):

$$\left(\frac{\partial \beta}{\partial P}\right)_T = \frac{1}{K^2}\left(\frac{\partial K}{\partial T}\right)_P \tag{13}$$

Another important interrelation is given by Maxwell's equation, where the product of the thermal expansion coefficient and isothermal bulk modulus βK is equal to the rate of change in pressure with respect to temperature $\left(\frac{\partial P}{\partial T}\right)_V$ (see Appendix A). The temperature dependence of this product is path dependent and can be considered at either constant pressure or constant volume (Anderson, 1989):

$$\left(\frac{\partial(\beta K)}{\partial T}\right)_V = \frac{1}{T}\left(\frac{\partial C_V}{\partial V}\right)_T = -\frac{\rho K}{T}\left(\frac{\partial C_V}{\partial P}\right)_T \tag{14}$$

$$\left(\frac{\partial(\beta K)}{\partial T}\right)_P = K\left(\frac{\partial \beta}{\partial T}\right)_V \tag{15}$$

where C_V is the specific heat capacity at constant volume. In other words, the path of heat transfer processes, whether the heat is transferred at constant pressure or constant volume, determines the rate of change in pressure (see Appendix A). Moreover, the temperature derivative of the bulk modulus at constant pressure is the summation of an intrinsic change (due to a temperature change at constant volume) and a extrinsic change (due to a volume change) (Manghnani et al., 1972; Kung et al., 2000):

$$\left(\frac{\partial K}{\partial T}\right)_P = \left(\frac{\partial K}{\partial T}\right)_V + \left(\frac{\partial K}{\partial V}\right)_T \left(\frac{\partial V}{\partial T}\right)_P \tag{16}$$

On the other hand, the stress dependence of the linear thermal expansion coefficient will be modified due to a temperature dependence of the elastic modulus (Eq.17 and Eq.18) (Taylor and Taylor, 1998):

$$\beta_a = \beta_0 - \frac{1}{E^2}\frac{\partial E}{\partial T}\sigma_a \tag{17}$$

where β_0 and β_a are the free and uniaxial thermal expansion coefficients, respectively. Uniaxial stress σ_a is positive in compression. The second term on the right hand side of Eq.17 shows that the material will change in length as a result of a temperature dependence of the Young's modulus. Eq.18 describes how the temperature dependence of elastic moduli influences the stress dependence of the uniaxial thermal expansion coefficient.

$$\left(\frac{\partial \beta_a}{\partial \sigma_a}\right)_T = \frac{1}{3K(1-2\nu)}\left[\frac{1}{K}\left(\frac{\partial K}{\partial T}\right)_P - \frac{2}{(1-2\nu)}\left(\frac{\partial \nu}{\partial T}\right)_{\sigma_a}\right] \tag{18}$$

2.2 Volumetric coefficient of thermal expansion

Many microstructure-independent exact relations for the effective thermal expansion coefficient of composites have been derived based on the uniform field assumptions (Voigt, 1928; Reuss, 1929) or by including boundary effects and shear moduli of constituents (Turner, 1946)(Kerner, 1956). For example, the effective thermal expansion coefficient of a two phase elastic composite (β_s^{eff}) can be estimated by the following equation (Levin, 1967; Berryman, 1995; Ghabezloo and Sulem, 2008):

$$\beta_s^{eff} = f_1\beta_1 + f_2\beta_2 + \frac{\frac{1}{K_s} - \left(\frac{f_1}{K_1} + \frac{f_2}{K_2}\right)}{\frac{1}{K_2} - \frac{1}{K_1}}(\beta_2 - \beta_1) \tag{19}$$

where K_i and β_i are the bulk modulus and thermal expansion of the ith constituent.

Campanella and Mitchell (1968) suggested that the bulk thermal expansion coefficient of the skeleton β_b may be taken as that of the solid constituents β_s. McTigue (1986) employed this idealized model at drained conditions. Palciauskas and Domenico (1982) expressed the bulk thermal expansion coefficient of the rock as a volume average of the pore thermal expansion coefficient β_p and the thermal expansion coefficient of the polycrystalline solid grain:

$$\beta_b = (1-\phi)\beta_s + \phi\beta_p \tag{20}$$

2.3 Bulk modulus of porous rock

In case of heterogeneous solid grains, the unjacketed modulus is a weighted average of the bulk modulus of the constituents, albeit an unusual one (Berryman, 1995). Hill (1952) showed that the arithmetic mean (Voigt average) and the harmonic mean (Reuss average) are the upper and lower bounds of effective elastic moduli, respectively. The Voigt-Reuss-Hill (VRH) average (Eq.21) is simply the arithmetic average of the upper and lower bounds and is used to estimate the effective elastic moduli of the rock in terms of its constituents. Brace (1965) found that for low porosity rocks at high pressure the VRH average confirms the experimental values:

$$K^{eff} = \frac{1}{2}\left[\sum f_i K_i + \left(\sum \frac{f_i}{K_i}\right)^{-1}\right] \tag{21}$$

where f_i is volume fraction and K_i is the bulk modulus of the constituents. A narrower range is given by Hashin-Shtrikman bounds (Hashin and Shtrikman, 1963) (see Appendix B).

3 Sample material and experimental procedure

3.1 Sample material

Several experiments were performed in order to study the thermoelastic response of saturated Flechtinger sandstone (Table 2), an outcropping equivalent of the Groß Shönebeck geothermal reservoir rock (Heiland

and Raab, 2001). The Flechtinger sandstone is a Lower Permian (Rotliegend) sedimentary rock. It crops out northwest of Magdeburg, Germany (Milsch et al., 2008). Rock specimens of 50 mm in diameter and 100 mm length were employed to investigate the relation between temperature, pressure, rock volumetric deformation and fluid mass content variations. Porosity of the cores was measured to be between 9% to 11% using the dry and immersed weights. Its unconfined compressive strength (UCS) was experimentally determined as 56.7 MPa. This is in agreement with what has been previously reported by Heiland and Raab (2001). The tensile strength of the Flechtinger sandstone was measured by Hecht et al. (2005) to be about 3.9 MPa. A detailed composition of Flechtinger sandstone (samples 1 and 2) and the selected elastic properties of the minerals are given in Table 1.

Table 1: Bulk and shear modulus of constituent minerals [GPa] (Schön, 2004; Mavko et al., 2003). The sample composition was provided by Schepers (personal communication).

mineral	volume fraction [sample 1]	volume fraction [sample 2]	bulk modulus [VRH average]	shear modulus [VRH average]
Quartz	63.98	67.51	37.85	44.3
Albite	10.27	10.45	55	29.5
Microcline	12.88	13.29	53.8	27.25
Orthoclase	2.02	1.75	48.15	26.45
Illite	7.38	3.79	23	8
Calcite	3.03	2.48	73	32
Hematite	0.42	0.72	97.5	92.8

3.2 Experimental procedure and data processing

The experiments were conducted in a conventional triaxial testing system (Mechanical Testing System, MTS) for which a description is given by Heiland (2003) and Blöcher et al. (2007). Following an uniaxial and an unjacketed test, poroelastic constants were measured under hydrostatic loading in a drained regime. First of all, the system was vacuumized and a dry specimen was saturated by flowing water through. Pore pressure was maintained constant through upper and lower pore fluid ports. In order to minimize the inelastic effects, preconditioning was applied according to Hart and Wang (1995) and Blöcher et al. (2007). Preconditioning consists of cycling confining pressure between 0 to 60 MPa at a rate of 1 MPa/min. During preconditioning of the sample, the pore fluid ports were open to the atmosphere and the cycles were repeated four times. After completion of preconditioning, the pore pressure was increased to 1 MPa. This pore pressure level is high enough to prevent steam generation, since the saturation pressure of water at 150°C is 0.476 MPa (Smith et al., 2001). Confining pressure was cycled between 2 to 55 MPa at a rate of 0.1 MPa/min (Fig.1). Each cycle was composed of an upward ramp, a 60 minutes plateau to equilibrate pore pressure, and a downward ramp. Having completed each pressure cycle, temperature was increased step wise to 30°C, 60°C, 90°C, 120°C and 140°C (see Fig.1). The temperature measurement showed ±2°C deviation from the set values. A low heating rate of 0.1-0.2 °C/min was employed because high heating rates generate spatial temperature gradients in the sample that may produce microcracks or microstructural damage. The theory of drained deformation contains three poroelastic constants: the drained bulk modulus K_d, the shear modulus G, and Biot coefficient α, two of them, K_d and α, were measured at different temperature levels.

Data was recorded every 15 seconds which corresponds to 25 KPa increase in confining pressure. The same sampling rate (four per minute) was employed for the pump system. In order to minimize the effect of small fluctuations of the recorded data two approaches are common Ghabezloo and Sulem (2008):

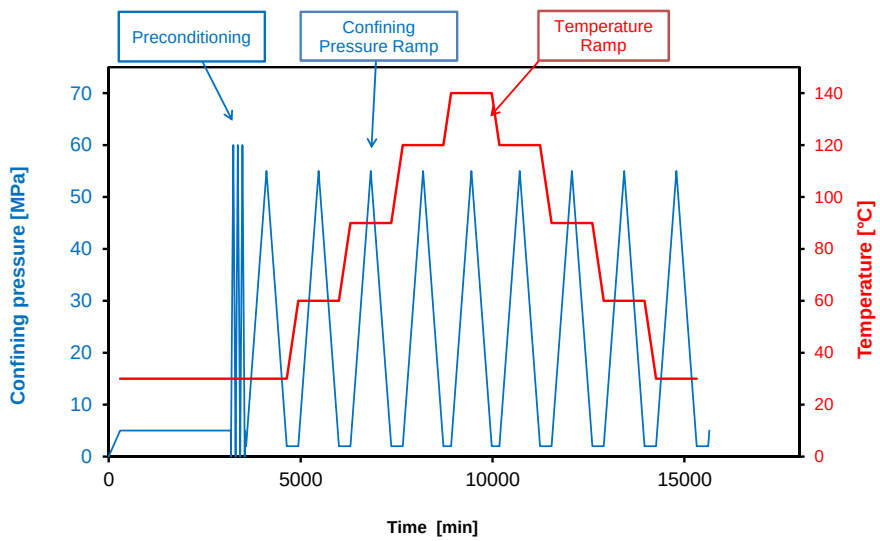

Figure 1: Following the axial and unjacketed tests, the drained poroelastic parameters were measured at hydrostatic conditions: first, preconditioning was applied and then confining pressure was cycled and finally temperature was increased step wise.

fitting data to a mathematical function or averaging the data. In our experiments, data was processed by averaging 15 raw data. Averaging has the advantage of defining the elastic moduli as secant, tangent or mean values more conveniently.

3.3 Corrections with respect to the drainage system

Drained conditions are defined as deformation of a saturated rock at constant pore pressure. While squeezing the rock sample, the pore fluid is expelled into the drainage system which itself experiences a volume change in case of changes in pressure or temperature. Ghabezloo and Sulem (2010) have given a correction method for measurements of undrained poroelastic parameters. The compressibility of the drainage system was constant, hence its temperature dependence was analysed by a solid dummy sample at different temperatures. The compressibility of the drainage system was measured to be approximately constant (0.477 GPA^{-1}) at different temperature levels.

Inside the cell, a uniform temperature distribution is a reasonable assumption. The effect of thermal expansion of the drainage system and the thermal variations of the fluid content during heating were excluded while analysing the raw data. Furthermore, the volume of the expelled water was brought to the reference conditions by introducing a volume factor B_v. Density of water at 1 MPa pressure was derived by employing the NIST REFPROP software and was written as a third order function of temperature (°C) Lemmon et al. (2007):

$$\rho_d(T) = 4.28 \times 10^{-6} T^3 - 0.003712 T^2 - 0.1076 T + 1002.5 \tag{22}$$

The cumulative volume of the expelled water was multiplied by a volume factor B_v:

$$B_v = \frac{V_{ref}}{V_d} = \frac{\rho_d}{\rho_f^{ref}} \tag{23}$$

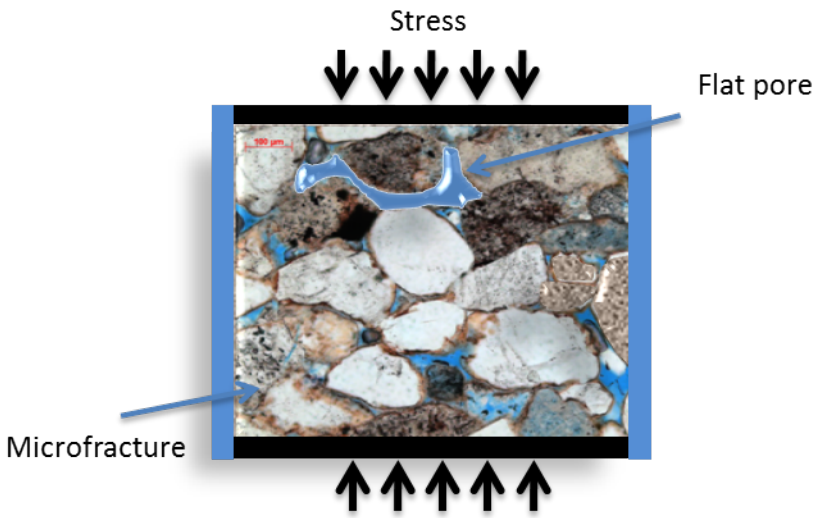

Figure 2: Micro image of Flechtinger sandstone. Two distinct features are recognizable: a high aspect ratio pore and an intergranular microfracture.

where V_{ref} and ρ_f^{ref} are volume and density of the fluid at reference pump conditions and V_d and ρ_d are volume and density of the fluid at drainage system conditions. Moreover, the heat transfer surface area was extended by employing fins and a spring shaped tube right after the downstream pore pressure port.

4 Experimental Results

The results of the experiments were interpreted in terms of the thermoporoelasticity theory. Following an uniaxial and an unjacketed experiment, drained experiments were performed at different temperature levels. That is, each drained test can be interpreted by isothermal theory of poroelasticity and temperature steps describe the thermal variation in fluid mass content (first and second terms on the right hand side of Eq.1, respectively). The measured properties are macroscopic properties. However, the micro scale study is important in case of changes in pore geometry or nonlinearity due to changes in grain to grain contact area. A microscopic image of the Flechtinger sandstone after thermal and mechanical loading is shown in Fig.2. Two distinct features are recognizable: a high aspect ratio pore and a microfracture within a grain. The microfractures within grains occur most likely close to the larger grains and at the boundaries between grains because of high stress concentrations.

4.1 Hydraulic properties

Porosity and permeability of the samples were measured before mechanical testing. Porosity varied between 9 to 11% and permeability was in the range of 0.17 to 0.36 mD (Table 2).

4.2 Young's modulus and Poisson's ratio: Uniaxial test

Table 3 presents elastic parameters of the Flechtinger sandstone (FLG02) which were obtained during a drained uniaxial test. Young's module E and Poisson's ratio ν were obtained at 50% axial peak stress. The lower and upper Hashin-Shtrikmann bounds (see Appendix B) of the water saturated bulk modulus range

Table 2: Specimen properties

	Porosity	Permeability	Grain density
Specimen	[%]	$[mD]^*$	[gr/cm^3]
FLG01	10.7	0.36	2.66
FLG02	10.8	0.34	2.66
FLG03	9.1	0.17	2.62
FLG04	10.1	-	2.64

$*1mD{=}10^{-15}m^2$

between 14 and 36 GPa. The difference between upper and lower bounds depends on how different the constituents are. Presence of water with properties different from solid minerals increases this difference. The saturated bulk modulus of Flechtinger sandstone was calculated ($K = E/3(1-2\nu)$) to be 15.9 GPa, which is closer to the lower bound of saturated bulk modulus (constant stress).

Table 3: Elastic parameters of Flechtinger sandstone (FLG02)

Poisson's ratio	Young's Modulus	Peak stress	Yield point
ν[-]	E[GPa]	UCS[MPa]	Y[MPa]
0.31	18.1	56.7	38

4.3 Grain bulk modulus: Unjacketed test

The indirect measurement of Biot coefficient (Eq.6) requires the drained and grain bulk moduli to be known. In order to determine the grain bulk modulus an unjacketed test can be employed. Two approaches have been suggested by Hart and Wang (1995); either employing a water saturated jacketed sample and increasing the pore pressure and confining pressure at the same time and the same amount or saturating the sample with the confining oil and applying hydrostatic pressure. The latter approach was employed to characterize the solid grain bulk modulus in Flechtinger sandstone (FLG04). The effective unjacketed bulk modulus of Flechtinger sandstone was estimated (Table 4) to range between 40.78 to 41.75 GPa which is in agreement with the experimentally measured value (41.2 GPa, Fig.3).

Table 4: Bounds of the effective bulk moduli based on different models [GPa]: (VRH: Voigt-Reuss-Hill average, HSH+:Upper Hashin-Shtrikman bound, HSH-:Lower Hashin-Shtrikman bound, HSH_{av}: arithmetic average)

	Voigt	Reuss	$HSH+$	$HSH-$	VRH	HSH_{av}
sample1	42.21	39.97	41.44	40.12	41.09	40.78
sample2	42.72	40.77	42.09	40.99	41.75	41.54

4.4 Drained bulk modulus and thermal expansion: Hydrostatic test

Figure 4 displays the evolution of volumetric strain, confining pressure and temperature while performing drained experiments. The volume of the fluid was measured with pumps and the volumetric strain of the rock was measured by a circumferential and two axial extensometers. The stress-strain curves (Fig.5) show

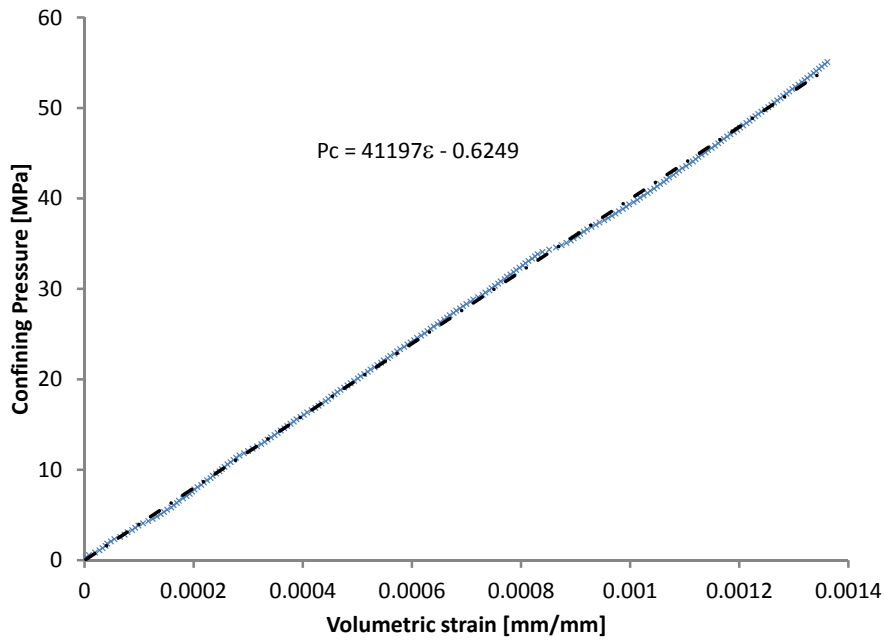

Figure 3: The unjacketed bulk modulus is the slope of confining pressure as a function of volumetric strain.

the characteristics which were previously discussed by Brace (1978) and Walsh (1965): the Flechtinger sandstone displayed nonlinearity and the loading-unloading cycles did not show reversibility. The higher the temperature, the more significant was the irreversible compaction of the sample (Fig.5). The change in volumetric fluid content while loading and unloading the Flechtinger sandstone sample is shown as a function of bulk volumetric strain (Fig.6). The bulk volume of the sample decreased due to inelastic effects after each pressure cycle. The inelastic strains (ε^p) are given in Table 5. The fluid volume was corrected for drainage system temperature effects. The temperature was increased between each isothermal step and the expelled fluid and the fluid mass content were observed to decrease. The thermal expansion coefficient β_m reflects the changes in mass fluid content at given constant stress and pore pressure (Eq.4). Ravalee and Guéguen (1994) reported a value of $\beta_m = -46 \times 10^{-5}$ K^{-1} for a low porosity ($\phi = 0.0018$) igneous rock. The value of β_m for Flechtinger sandstone was experimentally determined to be -14.8×10^{-4} K^{-1} while heating the sample from 30°C to 60°C (Table 5). The magnitude of β_m decreased to -3.7$\times 10^{-4}$K^{-1} while heating the sample from 120°C to 140°C.

Table 5: Inelastic strains ε^p after unloading and thermal variation in fluid content β_m while heating the sample at 1 MPa effective pressure.

	Inelastic strain	Thermal variation
Measured after	$\varepsilon^p \times 10^{-4}[mm/mm]$	$\beta_m \times 10^{-4}[\mathrm{K}^{-1}]$
Cycle 1	4.8	-14.8
Cycle 2	9.8	-11.2
Cycle 3	8.8	-11.5
Cycle 4	10.4	-3.7

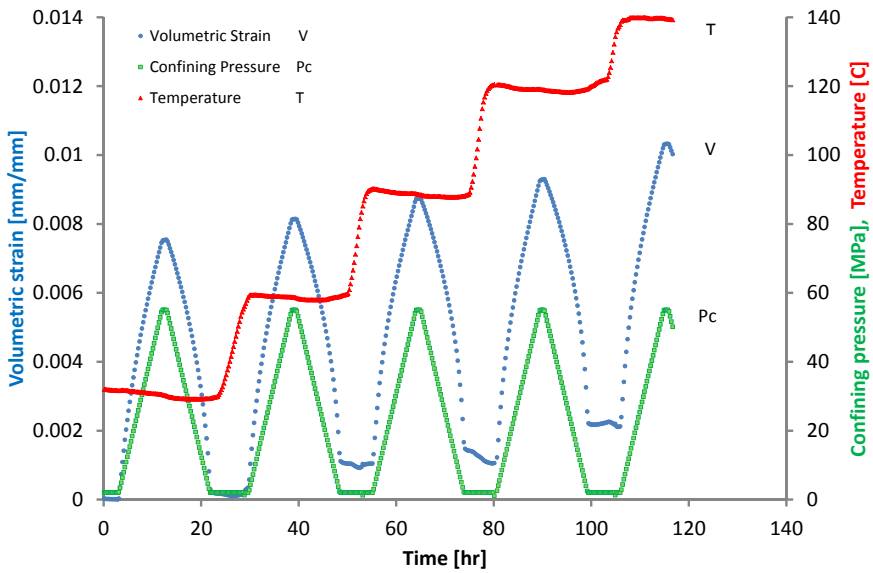

Figure 4: Drained experiments: Volumetric strain, confining pressure and temperature plotted as a function of elapsed time. The analysis was performed for the unloading paths where the unloading moduli can be approximated to be elastic moduli.

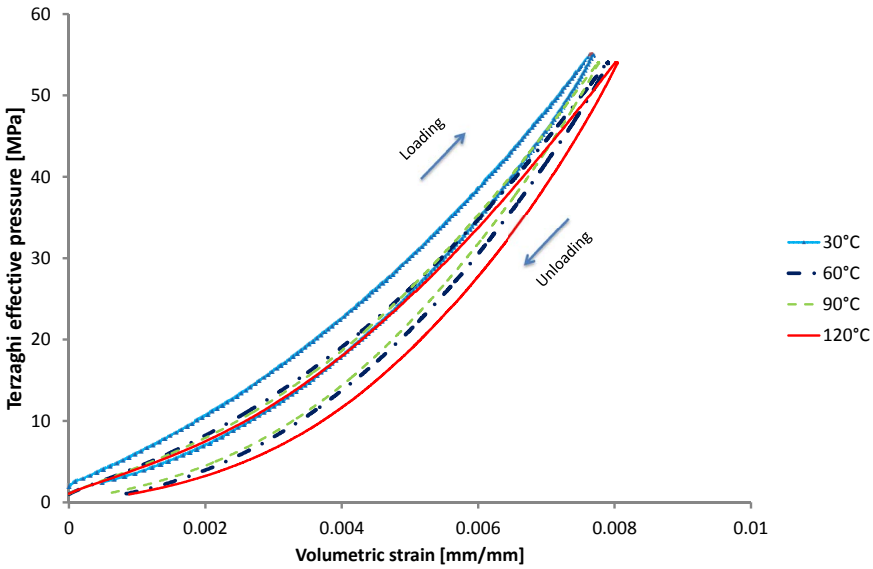

Figure 5: Terzaghi effective pressure as a function of volumetric strain. The stress-strain curves show nonlinearity and the loading-unloading cycles are irreversible.

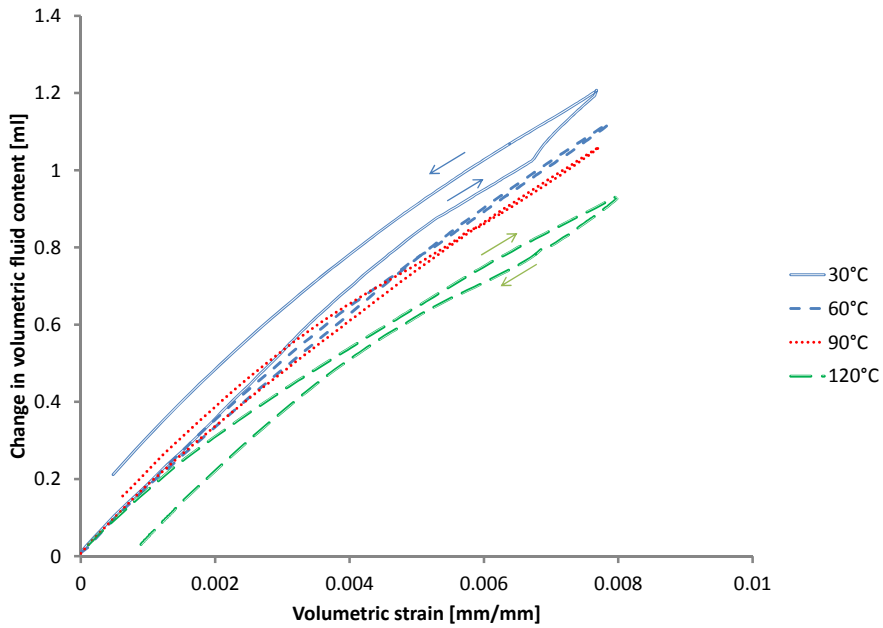

Figure 6: The change in volumetric fluid content as a function of the bulk volumetric strain. Opening and closing of the cracks and inelastic deformation created the nonlinearity and hysteresis in fluid cycles.

The volumetric thermal expansion coefficient of quartz is equal to 33.4×10^{-6} K^{-1} Palciauskas and Domenico (1982) and the average thermal expansion of feldspar is equal to 11.1×10^{-6} K^{-1} Ghabezloo and Sulem (2008). Thermal expansion of the bulk solid β_b was calculated as 27.2×10^{-6} K^{-1} (Eq.19). The bulk moduli of the constituents are given in Table 1. Ghabezloo and Sulem (2008) stated that estimated values by this approach are in agreement with experimentally measured values.

4.4.1 Tangent analysis

Both tangent and mean value definitions of unloading drained bulk modulus were employed to analyse the drained experiments. Figure 7 presents the evolution of the tangent drained bulk modulus $K_d = \left(\frac{\partial P_e}{\partial \varepsilon}\right)_T$ with respect to pressure and temperature while unloading the sample. The drained bulk modulus is a weak function of temperature and a strong function of effective pressure. Three phases have been recognized based on the temperature dependence of unloading drained bulk modulus: a low stress regime where the bulk modulus decreased with increasing temperature, a transition regime, and a high stress regime where the bulk modulus increased with increasing temperature. A transitional behavior was observed between 9 MPa and 20 MPa effective pressures. At effective pressures less than 9 MPa, the rock was more compliant at higher temperatures and above 20 MPa effective pressure, the rock was stiffer at higher temperatures. Figures 8 and 9 show the temperature dependence of tangent drained bulk modulus at low and high stress regimes, respectively. The pressure derivative of the unloading bulk modulus $(\partial K_d/\partial P_e)_T$ ranges from 182 to 224 MPa/MPa at high effective pressures and between 352 to 435 MPa/MPa at low effective pressures. The pressure derivative of drained bulk modulus was influenced by water bulk modulus at $60°C$ where the water has a higher bulk modulus Lemmon et al. (2007). Therefore, the pressure effect was less pronounced at $60°C$ and high stresses in comparison to other temperature levels.

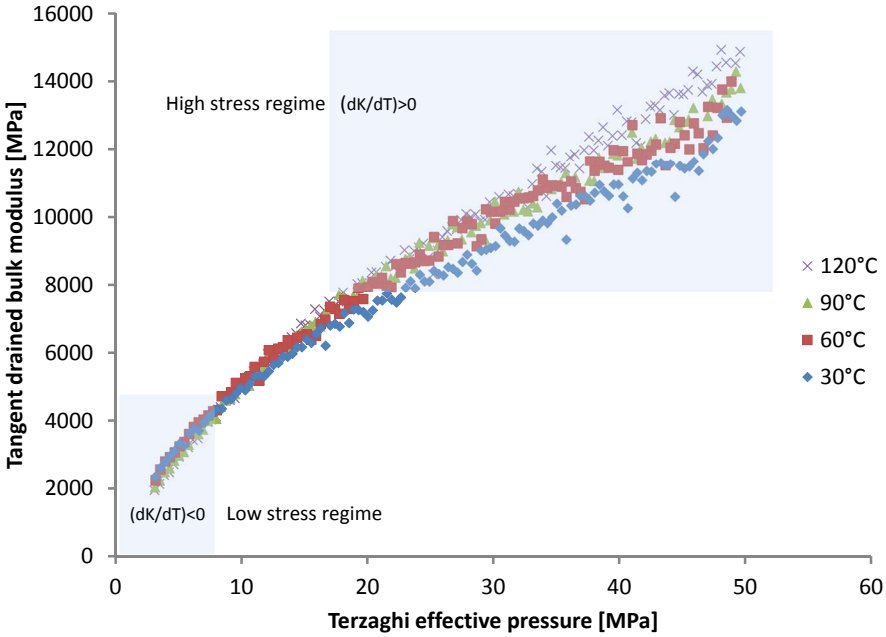

Figure 7: The tangent drained bulk modulus as a function of Terzaghi effective pressure at unloading path. Three different regimes were recognized based on the temperature dependence of the tangent drained bulk modulus. The drained bulk modulus is a weak function of temperature but it depends strongly on confining pressure.

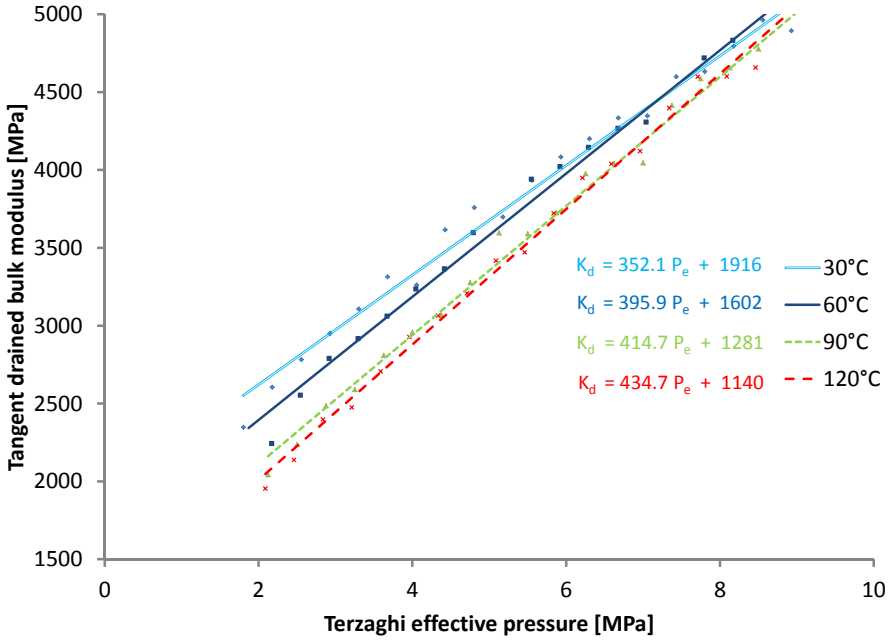

Figure 8: The tangent drained bulk modulus as a function of Terzaghi effective pressure at unloading path and the low stress regime.

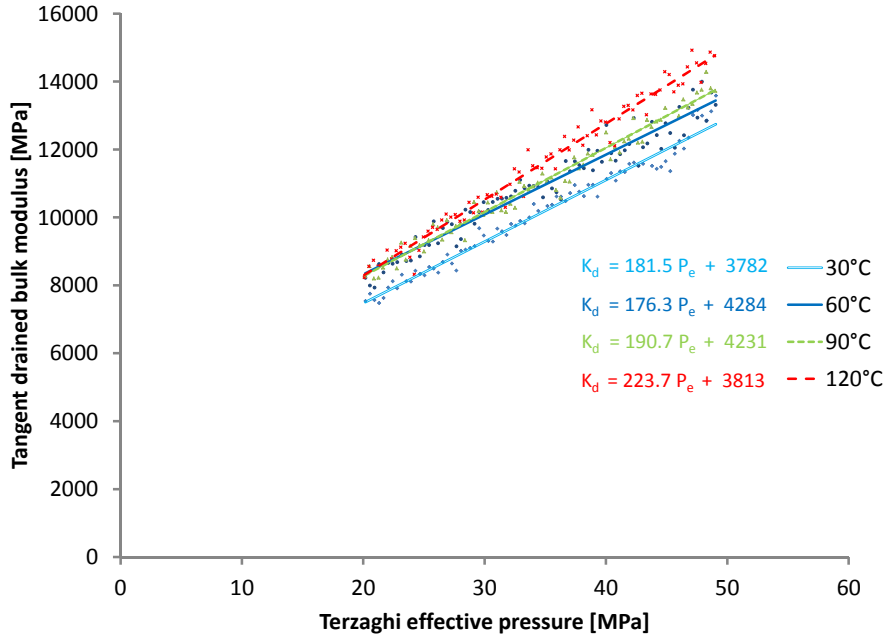

Figure 9: The tangent drained bulk modulus as a function of Terzaghi effective pressure at unloading path and the high stress regime.

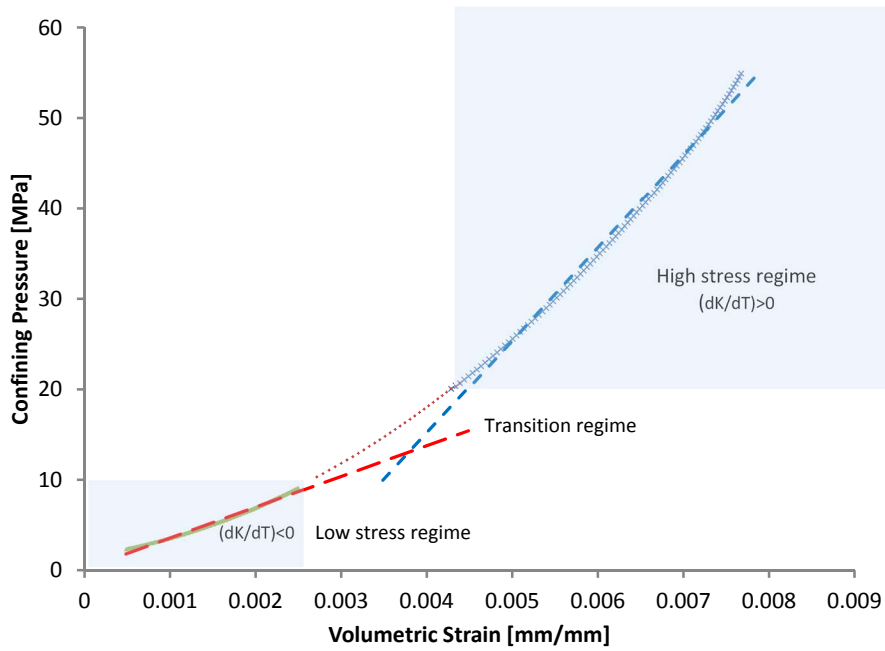

Figure 10: Confining pressure plotted as a function of volumetric strain. A bilinear model was employed to characterize the temperature dependence of drained bulk modulus. Three different regimes were recognized.

4.4.2 Mean value analysis

The mean value definition of drained bulk modulus $K_d = \left(\frac{\Delta P_e}{\Delta \varepsilon}\right)_T$ was employed to quantify the effect of temperature at low and high stress regimes. Each loading path was characterized by two bulk moduli, corresponding to the slope of the stress-strain curves at low and high stress regimes, respectively (see Fig.10). High effective pressure parts of the unloading curves approximate what can be assumed to be linear elastic behavior, however, the elastic constants were found to be better described by unloading path analysis (Table 6).

Table 6: Bulk modluli for unloading paths at low and high stresses.

Temperature [°C]	$\sigma < 9$ MPa	$\sigma > 20$ MPa
30	3390	10250
60	3320	11060
90	3120	11130
120	3050	11740

At low confining pressures, the drained bulk modulus decreased with increasing temperature ($\partial K_d/\partial T < 0$) at an average rate of -3.8 MPa K^{-1}. At high confining pressures, the bulk modulus increased ($\partial K_d/\partial T > 0$) at an average rate of 16.5 MPa K^{-1}.

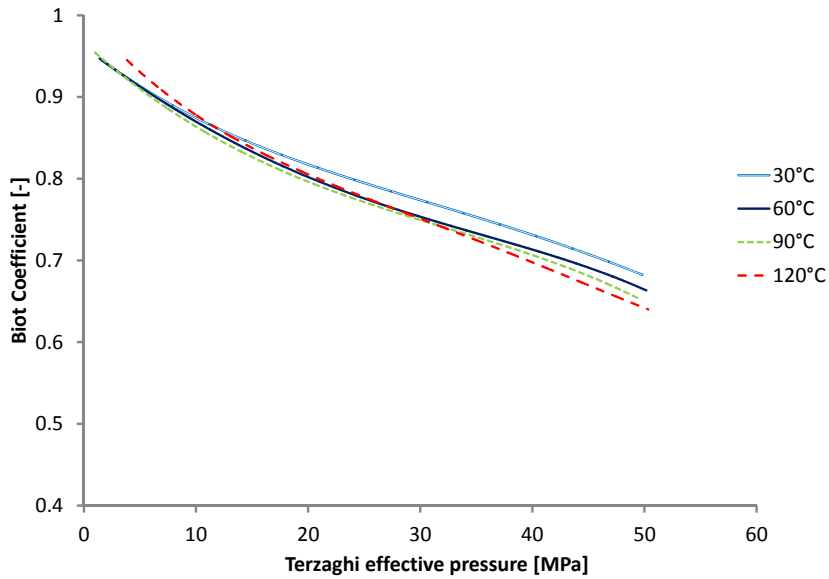

Figure 11: Biot coefficient as a function of Terzaghi effective pressure (indirect method, Eq.6).

4.5 Biot coefficient: direct and indirect method

Biot coefficient was measured by employing both direct and indirect methods. Two separate experiments are required in an indirect measurement of the Biot coefficient (Eq.6). Hence, two hydrostatic compression tests were performed on jacketed and unjacketed specimens in order to measure the drained bulk modulus of the framework K_d and the bulk modulus of the solid grains K_s, respectively. The unloading tangent drained bulk modulus and a constant unjacketed bulk modulus of 41.2 MPa were employed to calculate indirect Biot coefficient. The Biot coefficient decreased gradually by increasing Terzaghi effective pressure and temperature from 30°C to 140°C (Fig.11). Figure 12 shows the Biot coefficient measurement with the direct method at loading paths. The Biot coefficient decreased with increasing Terzaghi effective pressure. At lower effective pressures a nonlinear behavior was observed whereas the dependence of the Biot coefficient on confining pressure was approximately linear for higher effective pressures. The value of α ranges from 0.8 to 1 at 30°C. While increasing temperature the Biot coefficient decreased and at 120°C it ranged from 0.516 to 1. The evaluated Biot coefficients by employing the direct method were compatible with the results of the indirect method particulary at high effective pressures where the solid approached the linear elastic behavior. That is, for both methods, the measured Biot coefficient reacted to the rise in pressure and temperature in the same way.

4.6 Inelastic behavior of Flechtinger sandstone

The stress-strain curves showed that the Flechtinger sandstone suffered permanent deformation and inelastic behavior. The inelastic strains could be plastic or viscoelastic (creep). Hence, the deformation under constant stress (Fig.13) and the rate of deformation as a function of time were analysed. Each cycle was composed of a loading ramp, a 60 minutes plateau at 54 MPa effective pressure and an unloading ramp. The data at plateau time could represent the time dependent behavior of the sample under constant stress. Therefore, the volumetric strain at each temperature level was plotted as a function of time, pressure and temperature. The total change in the volumetric strain under constant stress is as high as 4×10^{-5}[mm/mm]. However, this amount of strain is almost within the accuracy of measurements

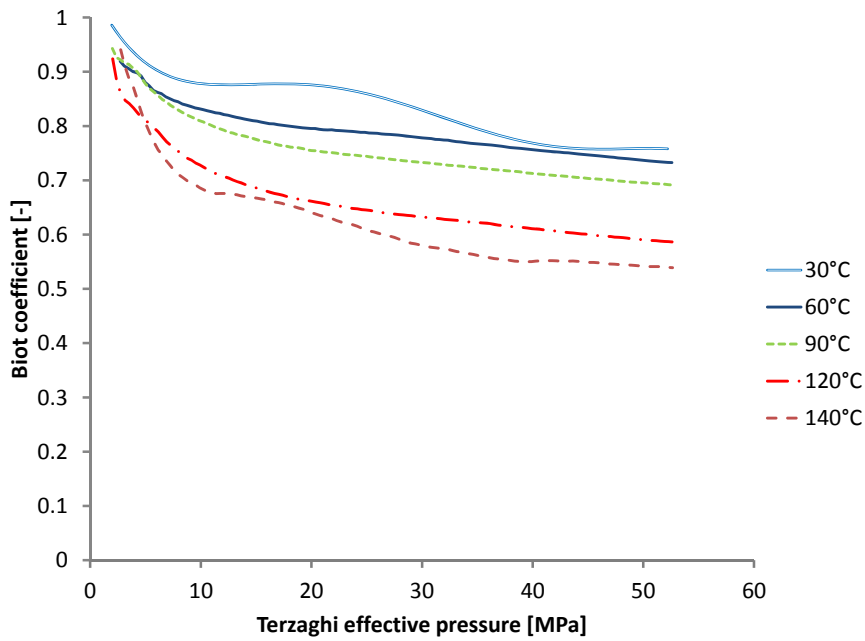

Figure 12: Biot coefficient as a function of Terzaghi effective pressure at different temperature level (direct method, Eq.10).

2×10^{-5}[mm/mm]. The total volumetric strain under constant stress decreased with increasing temperature from 30 to 90°C and increased afterwards. The rate of deformation at constant stress was as high as 1×10^{-8} [mm/mm/s].

5 Discussion

The temperature effects on a granular rock such as Flechtinger sandstone can be described by interrelations between bulk modulus and thermal expansion coefficient. Both, stress dependence of the thermal expansion coefficient and path dependence of heat transfer processes influence the thermomechanical behavior of the rock. For example, the temperature dependence of the bulk modulus of quartz depends on either the heat transfer performed at constant pressure or constant volume (Fig.14). The temperature derivative of the isothermal bulk modulus is positive at constant volume (strain) and negative at constant pressure (stress). That is, at constant pressure a thermal softening of quartz occurs and the bulk modulus decreases.

The experiments were performed at isothermal conditions, thus the thermodynamic state variables were effective pressure (stress) and bulk volume (strain). Consequently,

$$dK_d = \left(\frac{\partial K_d}{\partial P_e}\right)_{V_b} dP_e + \left(\frac{\partial K_d}{\partial V_b}\right)_{P_e} dV_b = \left(\frac{\partial K_d}{\partial P_e}\right)_{V_b} dP_e + \frac{1}{\beta V_b}\left(\frac{\partial K_d}{\partial T}\right)_{P_e} dV_b \tag{24}$$

and recalling Eq.16:

$$dK_d = \left(\frac{\partial K_d}{\partial P_e}\right)_{V_b} dP_e + \frac{1}{\beta V_b}\left[\left(\frac{\partial K_d}{\partial T}\right)_{V_b} + \left(\frac{\partial K_d}{\partial V_b}\right)_{T}\left(\frac{\partial V_b}{\partial T}\right)_{P_e}\right] dV_b \tag{25}$$

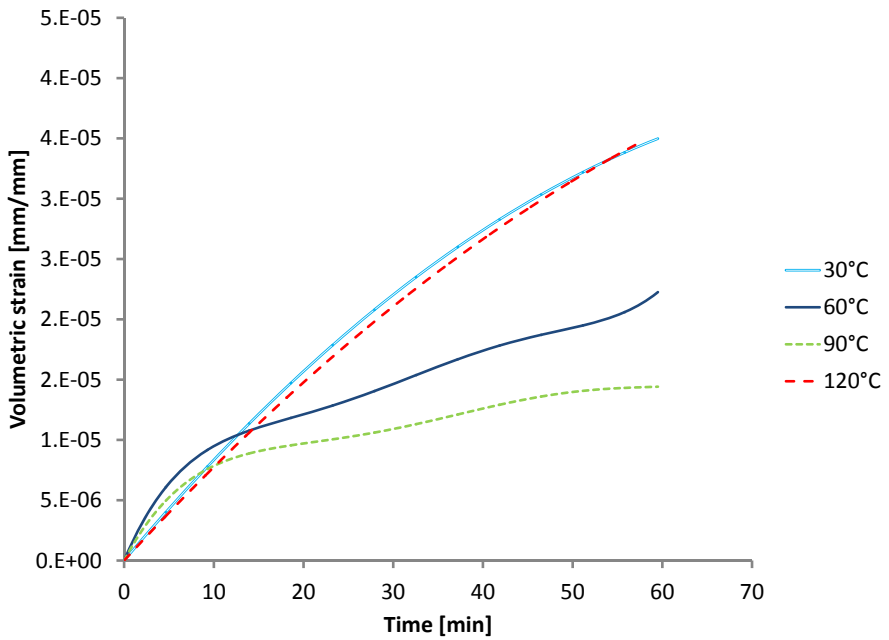

Figure 13: The time dependent behavior of Flechtinger sandstone (creep) was investigated by analyzing deformation under constant stress as a function of time.

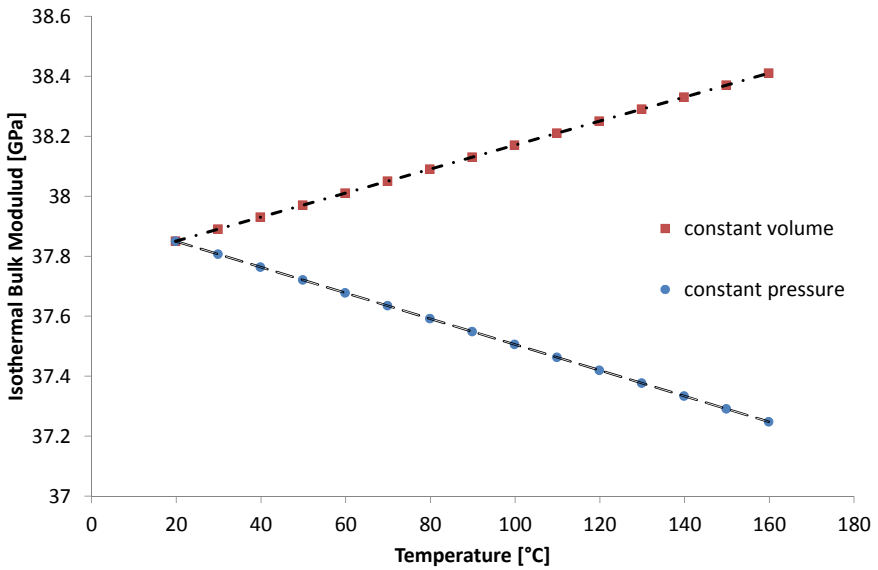

Figure 14: Isothermal bulk modulus of quartz. The applied mechanical boundaries influence on the thermo-mechanical behavior of the quartz. The temperature derivative of quartz bulk modulus is given by Carmichael (1989).

The temperature derivative of the bulk modulus at constant pressure is the summation of an extrinsic change and an intrinsic change. In general, the extrinsic effect is larger and makes the temperature derivative negative. However, in presence of active load, the pressure derivative of the bulk modulus is positive and always increasing the bulk modulus. The derivative of tangent bulk modulus of the Flechtinger sandstone was observed to be negative at stresses lower than 9 MPa and positive at stresses higher than 20 MPa. This behavior can be explained by considering a competition between volume and pressure with respect to temperature. At low stress regime, the volumetric effects (extrinsic changes) are dominant and soften the rock. However, at high stress regime, the pressure effects prevail and stiffen the rock.

The stress dependence of uniaxial thermal expansion induces an additional anisotropy at the microscale. The thermal expansion of the grains at the contact boundaries and the wetted area (the area which is in contact with fluid) will be modified due to changes in microstresses. For example, at contacts, due to higher stress concentrations the thermal expansion is lower while at the wetted area a free thermal expansion of a grain may occur. Consequently, the tendency of grains to expand into the pore space depends on the stress dependence of the thermal expansion coefficient which itself depends on the temperature dependence of Poisson's ratio $\left(\frac{\partial \nu}{\partial T}\right)_P$ and bulk modulus $\left(\frac{\partial K}{\partial T}\right)_P$. In addition, the temperature dependence of the bulk modulus is pressure dependent. If softening of solid grains is dominant (heat transfer at constant pressure) the grains expand laterally into the pore space as observed by Somerton (1992) and Blacic et al. (1981). In contrast, at higher effective pressures the hardening of the solid grains prevails which results in stiffening of sandstone.

The drained bulk modulus and thermal expansion of a rock are effective properties representing an imaginary homogeneous material. However, the change in local geometries due to crack closure and changes in pore geometry are important at the micro-scale. The drained bulk modulus of a porous rock depends on the effective matrix bulk modulus K_s and porosity ϕ as discussed by Guéguen and Palciauskas (1994). The porosity of a sedimentary rock is composed of cracks (high aspect ratio pores) and connected cavities. Cracks exposed to a pressure P will close easily if their aspect ratio is very small (very flat pores). In this case the pressure dependence of the effective bulk modulus is large. The nonlinear behavior of the Flechtinger sandstone at low stresses can be explained by a gradual closure/opening of the cracks while loading/unloading the sample. Moreover, the crack volume remaining open under applied Terzaghi effective pressure is decreasing and can modify the hydraulic properties of the rock (e.g. permeability).

The direct and indirect methods of measuring Biot coefficients are compatible particulary at high stresses and both methods show the same trend. However, the indirect measurement of the Biot coefficient rather describes matrix-bulk volume coupling, while the direct method highlights presence of the fluid and changes in micro-structure. For example, if a pore is open to the connected pore network the generated thermal pore pressure will be relaxed otherwise the pressure will rise and counteract the external load and consequently decreases the local effective stress. That is, the initial assumptions of drained deformation experiments (connected porosity and uniform pore pressure) have been violated due to crack closure and thermal pressurization of trapped pore fluid. Moreover, mechanical compaction of Flechtinger sandstone after each cycle induces inelastic deformation and changes the bulk and pore geometry (densification of the sample). In addition, thermal extraction of fluid decreases the fluid mass content and the potential to counteract the external load.

The poroelastic coupling parameter was derived theoretically by Zimmerman (2000) to be the product of Biot coefficient and Skempton coefficient. The effect of temperature on pore pressure can be described by a thermal pressurization coefficient which is governed by difference in thermal expansion coefficients of pore fluid β_f and pore volume β_p. This difference formerly appeared in the drained formulation as thermal expansion coefficient β_m (Eq. 4). This implies that discrepancies between fluid and rock properties govern the undrained and drained thermal behavior.

The stress strain curves showed that Flechtinger sandstone is subjected to permanent deformation and inelastic behavior. The inelastic behavior could be ascribed to the total deformation of the rock

skeleton, deformation of the solid matrix (solid compaction) or pore space deformation (pore collapse) (Carroll, 1980). It was found that inelasticity of the rock at low stresses is primarily due to opening and closing of cracks (Scholz, 1968; Cristescu, 1987). After unloading the sample the lower part of the stress-strain curves were strongly curved which represents the change in crack porosity and pore geometry as reported by others Brace (1978); Walsh (1980). In addition, the time dependent effects (plasticity or creep) are always present even at low stresses (Cristescu, 1987). The effect of temperature on creep strain rate is related to (T/T_o) or $(T/T_o)^{-1}$ where T_o is a reference temperature (Goetze and Evans, 1979; Evans and Kohlstedt, 1995). The inelastic strain rate in Flechtinger sandstone was decreased by increasing temperature up to 90°C and raised afterwards. While unloading the sample, the bulk volume was increasing due to elasticity. However, the local inelastic strains were compacting (creep) or had a plastic behavior. The plastic volumetric strains are also pressure dependent and differ at low and high stresses (Sulem et al., 1999). Both effects, creep or plasticity, could result in a higher unloading stiffness at high effective pressure. In conclusion, the inelastic behavior and the path dependency of the temperature derivative of the bulk modulus could explain the thermomechanical behavior of the Flechtinger sandstone and the related softening or hardening.

6 Summary and conclusions

The thermo-mechanical behavior of Flechtinger sandstone was investigated. The temperature and pressure dependence of the drained bulk modulus was studied by performing experiments at different temperature levels. The drained bulk modulus was strongly pressure dependent due to changes in contact area (Hertzian contact) and crack closure. The drained bulk modulus increased with increasing confining pressure from 3.39 GPa at low effective stresses to 10.25 GPa at high effective stresses. Moreover, the drained bulk modulus increased from 10.25 GPa to 11.74 GPa with increasing temperature from 30°C to 120°C at high effective stresses. Applying pressure always increased the drained bulk modulus of Flechtinger sandstone. In contrast, the effect of temperature was pressure dependent. A stress dependence of thermoelastic parameters arises as a result of the temperature dependence of the elastic moduli. At low effective pressures, the temperature derivative of the drained bulk modulus was negative (more compliant), however at high effective pressures, it was positive (stiffer). Flechtinger sandstone showed an inelastic behavior after unloading. The higher the temperature, the more significant was inelastic compaction of the bulk volume.

The evaluated Biot coefficients by employing the direct method were compatible with the results of the indirect method particulary at high effective pressures where the solid approached the linear elastic behavior. The Biot coefficient decreased with increasing temperature and effective pressure. It decreased from 1 to 0.735 by increasing effective pressure from 1 to 54 MPa at 60°C. Thermal variations of fluid mass content β_m were measured to be -14.8×10^{-4} K^{-1} while heating the sample from 30°C to 60°C. The measured unjacketed bulk modulus of Flechtinger sandstone is in agreement with theoretical values (41.2 GPa). The bulk thermal expansion coefficient of Flechtinger sandstone was theoretically calculated to be 27.2×10^{-6} K^{-1}.

Two types of nonlinearity in mechanical behavior of granular rock were distinguished in this study, one due to Hertizan contacts and crack closure and the other due to the temperature and stress dependence of physical properties. Both nonlinearities can influence the transport properties of a saturated sandstone, i.e., by crack closure or thermal expansion of the grains into the pore space. Moreover, the change in sign of the temperature derivative of the drained bulk modulus suggests that the temperature effects at shallow and deep geothermal reservoirs are different.

Appendixes

A Thermodynamics

Pressure P and isothermal bulk modulus K are volume derivatives of the Helmholtz free energy $F(V,T)$. Volume V and thermal expansion coefficient β are the first and second derivative of the Gibbs free energy $G(P,T)$, respectively Anderson (1989). Another important interrelation between β and K can be obtained by classic thermodynamics Anderson (1989); Boley and Weiner (1988):

$$dU = dQ + dW = TdS + \sigma_{ij}d\varepsilon_{ij} = Tds - PdV \tag{26}$$

where U is internal energy, S is entropy, dQ is the amount of heat added to the system, and W work done on the system, ε_{ij} and σ_{ij} are the strain and stress tensor components, respectively.

$$\left(\frac{\partial U}{\partial V}\right)_T = T\left(\frac{\partial S}{\partial V}\right)_T - P = T\left(\frac{\partial P}{\partial T}\right)_V - P \tag{27}$$

$$\left(\frac{\partial P}{\partial T}\right)_V = \left(\frac{\partial S}{\partial V}\right)_T = \beta K \tag{28}$$

Eq.27 and Maxwell's relation (Eq.28) describe how the change in internal energy due to added heat at isothermal conditions increases the pressure by a rate of $\left(\frac{\partial P}{\partial T}\right)_V$, which is equal to the product of the thermal expansion coefficient and the isothermal bulk modulus.

B Hashin-Shtrikman functions

The volumetric average over the medium is defined as the average of constituents weighted by their volume fractions:

$$\langle Q \rangle = \sum_{i=1}^{n} f_i Q_i \tag{29}$$

where Q_i is the elastic modulus in the i-th component. Berryman (1995) developed a more general form, which can be applied to more than two phases, including pore fluid properties. He introduced certain functions of the constituents' constants:

$$\Lambda(u) = \left\langle \frac{1}{K(r) + \frac{4}{3}u} \right\rangle^{-1} - \frac{4}{3}u = \left(\sum_{i=1}^{n} \frac{f_i}{K_i + \frac{4}{3}u} \right)^{-1} - \frac{4}{3}u \tag{30}$$

$$\Gamma(u) = \left\langle \frac{1}{G(r) + u} \right\rangle^{-1} - u = \left(\sum_{i=1}^{n} \frac{f_i}{G_i + u} \right)^{-1} - u \tag{31}$$

$$\zeta(K,G) = \frac{G}{6}\left(\frac{9K + 8G}{K + 2G}\right) \tag{32}$$

$$\begin{array}{lclcrcl} K_{HS}^{+} & = & \Lambda(G_{max}) & , & K_{HS}^{-} & = & \Lambda(G_{min}) \\ G_{HS}^{+} & = & \Gamma(\zeta(K_{max}, G_{max})) & , & G_{HS}^{-} & = & \Gamma(\zeta(K_{min}, G_{min})) \end{array}$$

CHAPTER 4

Originally published in the *Rock mechanics and Rock Engineering*

The effects of temperature and pressure on the porosity evolution of Flechtinger sandstone

Alireza Hassanzadegan, Guido Blöcher, Harald Milsch, Luca Urpi, Günter Zimmermann

Abstract

A porosity change influences the transport properties and the elastic moduli of rock while circulating water in a geothermal reservoir. The static and dynamic elastic moduli can be derived from the slope of stress-strain curves and velocity measurements, respectively. Consequently, the acoustic velocities were measured while performing hydrostatic drained tests. The effect of temperature on static and dynamic elastic moduli and porosity variations of Flechtinger sandstone was investigated in a wide range of confining pressure from 2 to 55 MPa. The experiments were carried out in a conventional triaxial system whereas the pore pressure remained constant, confining pressure was cycled, and temperature was increased step wise (25, 60, 90, 120, and 140°C). The porosity variation was calculated by employing two different theories: poroelasticity and crack closure. The porosity variation and crack porosity were determined by the first derivative of stress-strain curves and the integral of the second derivative of stress-strain curves, respectively. The crack porosity analysis confirms the creation of new cracks at high temperatures. The porosity variation was increasing with an increase in temperature at low effective pressures and was decreasing with a rise in temperature at high effective pressures. Both compressional and shear wave velocities were increasing with increasing pressure due to progressive crack closure. Furthermore, the thermomechanical behavior of Flechtinger sandstone was characterized by an inversion effect where the sign of the temperature derivative of the drained bulk modulus changes.

1 Introduction

The elastic properties of porous media and their pressure and temperature dependence are of interest in many research areas including material science, design of foundations, mine openings, geophysical exploration and reservoir geomechanics. The static elastic moduli of a porous rock can be derived from stress-strain curves in rock mechanical tests and dynamic elastic moduli can be determined by acoustic wave velocity measurements. The static elastic moduli better represent the stress and strain changes within the reservoir, since the dynamic tests only capture the elastic part of the rock response (Yale and Jamieson, 1994). The dynamic and static moduli depend on porosity, pore geometry, pressure, temperature and fluid saturations. Circulation of water in geothermal reservoirs will alter these parameters and consequently rock properties. The associated thermal and mechanical effects on rock properties are the subject of this study.

The thermal effects on mechanical behavior of a reservoir rock can be better described if the constitutive equations describe the microscopic physical processes at given conditions (Palciauskas and Domenico, 1988). Of main importance are the porosity and pore geometry evolution of the porous rock due to the applied pressure and thermal load, since the effective elastic properties of crustal rock are controlled to a large extent by porosity (Walsh, 1980). The porosity of rock has been divided by Walsh (1980) into two categories: equant dimension pores and flat pores (cracks or low aspect ratio pores). The low aspect ratio pores (long and narrow cracks) particularly reduce the effective moduli of rocks. The pores with a

circular shape are the stiffest type of elliptical pores and become compliant if their elliptical aspect ratio decreases. Biot theory of poroelasticity (Biot, 1941) assumes a granular porous medium with connected pores and crack closure theory assumes that rock contains a distribution of crack-like pores. Palciauskas and Domenico (1982) and McTigue (1986) extended the poroelastic theory to consider thermal effects and derived the linear constitutive equations. Zimmerman (1991) employed the method of Morlier (1971) to characterize the pore aspect ratio distribution of Boise, Berea and Bandera sandstones.

This study investigated the effects of temperature and pressure on porosity evolution, static and dynamic elastic moduli of Flechtinger sandstone, a representative of a Rotliegend reservoir rock in the North German Basin. The influence of temperature on strength of the rock have been experimentally investigated by other researchers, e.g. Handin and Hager (1957); Araujo et al. (1997); Vishal et al. (2011). Accordingly, the isothermal static and dynamic elastic moduli of the Flechtinger sandstone were measured at drained conditions and different temperature levels. The experimental data were analysed by employing two different effective medium theories: Biot poroelasticity theory (Biot, 1941) and crack closure theory (Walsh, 1980). The results are useful to describe the thermoporoelastic behavior of the rock, especially the effect of temperature and pressure on porosity and crack porosity. Moreover, the results are useful to understand the mechanisms of changes in static and dynamic elastic moduli due to circulation of water in underground reservoirs.

1.1 Static elastic moduli: triaxial tests

Effective medium theories provide an appropriate tool to calculate macroscale effective properties from microscale variables. The Biot's theory was formulated by employing irreversible thermodynamics and energy consideration, therefore the effective bulk moduli are independent of pore geometry. Walsh (1965) and Zimmerman (2000) employed a micro-mechanical approach to formulate the effective bulk modulus where the pore geometry should be specified. In this formulation, the calculation of effective bulk modulus can be reduced to the calculation of pore stiffness:

$$\frac{1}{K_d} = \frac{1}{K_s} + \frac{\phi}{K_\phi} \tag{1}$$

where K_s and K_d are the solid grain modulus and drained bulk modulus respectively. ϕ is the Eulerian porosity and K_ϕ is pore stiffness. In crack closure theory (Walsh, 1965) rock is portrayed as an elastic isotropic material that contains randomly oriented narrow cracks. In the following, first the Biot's theory of poroelasticity would be briefly described. Afterwards, the crack closure theory and aspect ratio distribution of porosity function would be explained.

1.1.1 Biot's theory of poroelasticity

The constitutive models in poroelasticity can be either described by energy consideration, Biot's theory (Biot, 1941, 1956, 1973; Rice and Cleary, 1976; Guéguen and Boutéca, 2004) or by micromechanics (Nur and Byerlee, 1971; Carroll, 1980). The thermal effects result in a thermal expansion of the solid grains and skeleton and a variation of fluid mass content at drained conditions (Palciauskas and Domenico, 1982; Guéguen and Boutéca, 2004).

The Biot coefficient α can be determined either by considering the stress-strain behavior of the rock and performing jacketed and unjacketed experiments (indirect method Eq. 2a) or by analyzing the change in the volumetric fluid content with respect to the volumetric strain of the rock (direct method Eq. 2b) at drained conditions (Hassanzadegan et al., 2012):

$$\alpha = 1 - \frac{K_d}{K_s} \tag{2a}$$

$$\alpha = -\frac{\zeta}{\varepsilon_b} = -\frac{dV_p}{V_b^o \varepsilon_b} \tag{2b}$$

where V_p is the pore volume, V_b^o is the reference bulk volume, ε_b is volumetric bulk strain, and ζ is the volumetric increment of fluid content normalized by the reference bulk volume. ζ is positive when the fluid is transferred into the reference volume and can be derived by analyzing the changes in pore volume (Zimmerman, 2000). In an isothermal drained process, pore pressure u is constant, thus fluid compression and expansion are absent and the only active mechanism is the bulk deformation which results in a volumetric mass transfer ζ.

The evolution in Lagrangian porosity n can be derived by the following equation (compactive ε_b is positive):

$$n = \phi^o - \alpha\varepsilon_b \tag{3}$$

The relation between Lagrangian porosity n and the Eulerian porosity ϕ can be described by the following equation:

$$n = \frac{V_p}{V_b^o} = \phi(1 - \varepsilon_b) \tag{4}$$

Carroll and Katsube (1983) developed the poroelastic theory in terms of the Eulerian porosity ϕ and the solid grain volume V_s:

$$d\phi = \left(\frac{1-\phi^o}{K_d} - \frac{1}{K_s}\right) dP' \tag{5}$$

where $P' = P - u$ is the Terzaghi effective pressure.

1.1.2 crack closure

The rock appears homogeneous at macro scale and heterogeneous at micro scale. The rock may contain pores and cracks which both have a strong influence on mechanical and transport properties. When the void space in the rock is consisted of randomly oriented penny shaped cracks, the crack porosity ϕ_c can be defined by a dimensionless crack density parameter Γ:

$$\phi_c = \frac{N}{V_b}\frac{4\pi l^2 w}{3} = \frac{4\pi N l^3 a}{3V_b} = \frac{4\pi a}{3}\Gamma \tag{6}$$

where l and w are semimajor axis length and semiminor axis length of penny shaped cracks ($w << l$) respectively. The ratio between semiminor axis to semimajor axis lengths w/l is the aspect ratio a, $\frac{N}{V_b}$ is the crack density, the number of cracks N in a representative elementary volume of the rock V_b, and $\Gamma = \frac{Nl^3}{V_b}$. In case of equant pores ($a = 1$), the the porosity would be qual to $4\pi\Gamma/3$.

The rate of change in porosity can be determined by first derivative of stress-strain curves (bulk modulus) when the porosity occurs as narrow cracks (Walsh, 1965). Zimmerman (1991) suggested an exponentially decreasing function for evolution of drained bulk modulus as a function of pressure:

$$\frac{1}{K_d} = \frac{1}{K_d^\infty} + \left[\frac{1}{K_d^i} - \frac{1}{K_d^\infty}\right]\exp(-\frac{P'}{\hat{P}}) \tag{7}$$

The superscript i represents the initial value at relaxed conditions and the superscript ∞ represents the value at confined conditions (high effective pressures). The distribution of penny shaped cracks as a function of aspect ratio is characterized by a distribution function $\gamma(a)$. The peak of distribution function corresponds to a pressure $\hat{P}$, at which cracks with a higher population are closed. That is, $\hat{P}$ is a characteristic closure pressure at which high density cracks are closed.

Morlier (1971) developed an inversion method that extracts the microstructure of porosity by introducing an aspect ratio distribution function $\gamma(a)$ and a crack density parameter $d\Gamma$. The aspect ratio

distribution function $\gamma(a)$ was related to the second derivative of the hydrostatic strain-stress curve which describes the microstructure of porosity:

$$\gamma(a) = -\frac{d\Gamma(a)}{da} = \frac{3}{4\pi V_0}\left[\frac{3\pi K_s(1-2\nu_s)}{4(1-\nu_s^2)}\right]^2\left[\frac{d^2V}{dP^2}\right]_{P^*} \tag{8}$$

It was assumed that the media is composed of the randomly distributed penny shaped cracks, where there is no interaction between them. This assumption is valid when the cracks are sufficiently far from each other or when the crack density is low. Moreover, the penny shaped cracks can close in aperture direction w, but their length (radius) l remains constant. That is, the penny shaped cracks cannot be shortened.

Morlier (1971) defined the density of penny shaped cracks whose initial aspect ratio lies between a and $a + da$ to be $d\Gamma(a) = -\gamma(a)da$. $\Gamma(a)$ is the density parameter of open cracks, the penny-shaped cracks whose aspect ratios is greater than the given aspect ratio a. The derivative of strain-stress curve should be evaluated at the crack closing pressure P^*:

$$P^* = \left[\frac{3\pi a K_s(1-2\nu_s)}{4(1-\nu_s^2)}\right] = K_\phi \tag{9}$$

where ν_s is solid grain Poisson's ratio. K_ϕ is defined in 2-D to be $\left(A_c^0 \frac{\partial P}{\partial A_c}\right)$ and in 3-D to be $\left(\phi_c^0 \frac{\partial P}{\partial \phi_c}\right)$, where A_c^0 and ϕ_c^0 are the reference area and reference porosity of the cracks, respectively. The rate of crack porosity change with aspect ratio is characterized by the aspect ratio distribution function of porosity $C(a)$ which can be written as:

$$C(a) = \frac{d\phi_c}{da} = \frac{4\pi a}{3}\gamma(a) = \left[\frac{3\pi K_s(1-2\nu_s)}{4(1-\nu_s^2)}\right]\left[\frac{1}{K_d^i} - \frac{1}{K_d^\infty}\right]\frac{a}{\hat{a}}\exp(-\frac{a}{\hat{a}}) \tag{10}$$

where $\hat{a}$ is the aspect ratio of penny shaped cracks at characteristic closure pressure. Consequently, the crack porosity can be calculated by the following formula (Jaeger et al., 2007):

$$\phi_{crack} = \int_0^\infty c(a)da = \left(\frac{1}{K_d^i} - \frac{1}{K_d^\infty}\right)\hat{P} \tag{11}$$

While the tangent drained bulk modulus K_d of Flechtinger sandstone was always an increasing function of effective pressure, its temperature dependence was pressure dependent during cyclic and thermal loading (Hassanzadegan et al., 2012). The softening of Flechtinger sandstone ($\partial K_d/\partial T < 0$) was occurred at relaxed state (effective pressures of less than 9 MPa) and stiffening ($\partial K_d/\partial T > 0$) was occurred at confined state (effective pressures more than 20 MPa).

1.2 Dynamic elastic moduli: acoustic velocity measurement

The acoustic wave velocities in rocks mainly depend on bulk density (ρ_b) and fluid properties which can be characterized in terms of: porosity and pore geometry, stress state, temperature, saturation, pore pressure, fluid type, viscosity, lithology, clay content and frequency of the waves (Yale, 1985; Nur and Wang, 1989a). The influence of effective pressure on compressional v_p and shear wave v_s velocities is generally represented by an equation of the form (Somerton, 1980):

$$v_{p,s} = AP'^{\frac{1}{e}} \tag{12}$$

The parameter A is varying widely according to Palen (1978) between 500 for soft rock to 3000 for hard rock. The exponent e varies between a value of six for unconsolidated sands to 40 for hard rocks (Palen, 1978).

The velocity change is a result of changes in effective pressure and bulk modulus of the rock skeleton. The efficiency of pore pressure and confining pressure to alter the acoustic velocities have been studied by Hearst and Nelson (1985). Schön et al. (1998) stated that v_p and v_s are generally increasing with an increase in confining pressure due to decrease of porosity and rearrangement of contacts (grain contacts and crack closure). Both effects are due to changes of rock skeleton properties (extrinsic properties) and not due to changes of intrinsic properties (elastic properties of minerals).

Increasing the temperature generally results in decreasing the velocities, however the effect of temperature in comparison to porosity and saturation is less pronounced (Hearst and Nelson, 1985). The velocity drop with increasing temperature was explained by the creation of microcracks during heating (Kern, 1978). In general, the temperature dependence of velocities can be ascribed to a temperature dependence of elastic moduli of the minerals and the pore fluid (intrinsic properties) and to changes in pore geometry (Hertzian contact and crack closure). Scheu et al. (2006) found an inverse behavior in volcanic rock. In contrast to the majority of rocks, increasing the temperature resulted in higher dynamic wave velocities. This phenomenon was linked to the thermal expansion of grains into the pore space which resulted in a reduction of pore volume.

2 Materials and methods

2.1 Materials

The Flechtinger sandstone is a Rotliegend sandstone of permian age, representative of a reservoir rock in geothermal reservoirs of the North German Basin. It is a consolidated, cross-bedded sandstone which is mainly composed of quartz, illite, carbonate and feldspar. It crops out near Magdeburg, in the northern part of Germany (Heiland, 2003). A detailed composition of the Flechtinger sandstone is given in Figure 1 (Schepers, 2012). The experiments were performed by employing cylindrical samples of 10 cm in length and 5 cm in diameter in a conventional triaxial testing system. The experiments were primarily designed to simulate the changes in effective stress due to water production and reinjection in deep geothermal reservoirs, e.g. Blöcher et al. (2010). Two specimens named as FLG04 and FLG05 (FLG stands for Flechtinger) were employed to perform unjacketed and jacketed experiments, respectively (Table 1). The initial porosity and grain density were measured by weighting the sample at dry and saturated conditions and permeability was measured at a constant flow rate of 0.25 ml/min and atmospheric downstream pressure.

The porosity of Flechtinger sandstone is between 9 to 11% and its permeability ranges between 10-1000 μD according to Heiland (2003) and Blöcher et al. (2010). The drained Young's modulus and Poisson's ratio of Flechtinger sandstone were measured to be 18.1 GPa and 0.31, respectively. The saturated bulk modulus was calculated to be 15.9 GPa. Its unconfined compressive strength (UCS) was experimentally determined by Hassanzadegan et al. (2012) to be 56.7 MPa. This is in agreement with what has been reported by Zang (1997). Having provided the hydraulic properties the elastic properties namely, static and dynamic moduli, were measured at drained conditions.

Table 1: Sample properties.

Specimen	Experiment Type	Porosity [%]	Permeability $[mD]^*$	Grain density $[g/cm^3]$
FLG04	Unjacketed	10.1	-	2.64
FLG05	Jacketed	10.7	0.67	2.66

$*1mD{=}10^{-15}m^2$

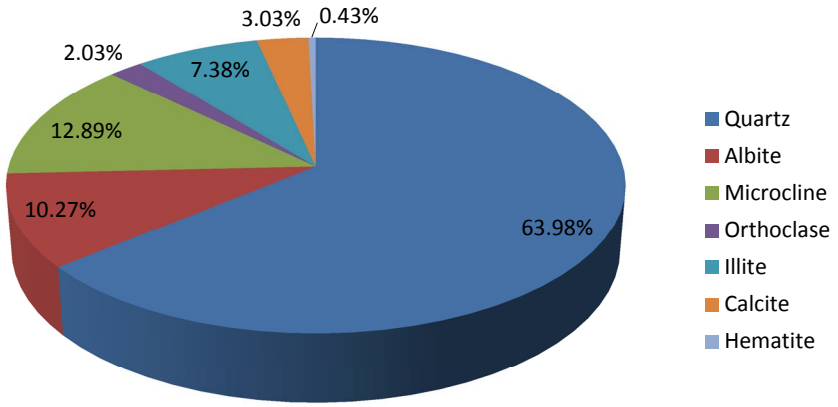

Figure 1: Composition of Flechtinger sandstone. The mineralogical composition is given by Schepers (2012) and were derived from X-ray powder diffraction (XRD), X-ray fluorescence spectroscopy (XRF), and electron microprobe analysis (EMPA) measurements.

2.2 Experimental procedures and analysis methods

A conventional mechanical testing system (MTS) was employed to measure the static and dynamic elastic moduli. The static moduli were derived by analyzing stress-strain curves and dynamic moduli were obtained by first arrival time analysis. The detailed description of the setup is given by Heiland and Raab (2001) and Blöcher et al. (2007). The set up is composed of two set of equipments; triaxial testing system and ultrasonic system. The triaxial testing system is composed of a triaxial cell, a pressure intensifier which allows to increase the confining pressure up to 140 MPa, a digital monitoring and recording system, and four water pumps which can provide up to 75 MPa pore pressure. The ultrasonic system consists of an oscilloscope, piezoelectric transducers placed at the endcaps and recording system.

2.2.1 Static tests

The experiments were carried out at drained conditions in the conventional triaxial testing system. The endcaps were placed on top and bottom of the sample and were connected to the pore fluid capillaries. First, the system was vacuumized and dry specimen was saturated by flowing water through it. A constant flow rate of 0.25 ml/min was applied. In order to minimize inelastic effects due to microcracks, preconditioning was applied according to Hart and Wang (1995) and Blöcher et al. (2007). Preconditioning consisted of cycling confining pressure between 0 to 60 MPa at a rate of 1 MPa/min. During preconditioning of the sample, the pore fluid ports were open to the atmosphere and the cycles were repeated four times. After completion of preconditioning, the water pumps were employed to increase the pore pressure to 1 MPa. The upstream and down stream capillaries were connected to the lower and upper endcaps, respectively. The axial and radial strains were measured by dual-axial and circumferential extensometers. The pump pressure, pump fluid volume, internal and external temperatures were recorded at a sampling

rate of four per minute in both triaxial and pump monitoring systems. Processing of the stress-strain data was accomplished by averaging every 15 raw data points.

The tests were performed while the confining pressure was cycled between 2 to 55 MPa at a rate of 0.1 MPa/min (Fig.2). Pore pressure was maintained at a constant pressure of 1 MPa through upper and lower pore fluid ports and within the capillaries. Each confining pressure cycle was composed of an upward ramp, a 120 minutes plateau to equilibrate pore pressure and a downward ramp. Having completed each pressure cycle, temperature was increased step-wise and stayed at constant temperatures of 25, 60, 90, 120, and 140°C while cycling confining pressure. That is, after each cycle the confining pressure was maintained at a constant pressure of 2 MPa, the pore pressure was kept at a constant pressure of 1 MPa and temperature was increased to the next level and stayed constant. A low heating rate of 0.1-0.2°C/min was applied. The temperature inside the triaxial cell was monitored by two thermocouples within ±1°C. The heat was provided by three heater bands which were attached to the triaxial cell assembly.

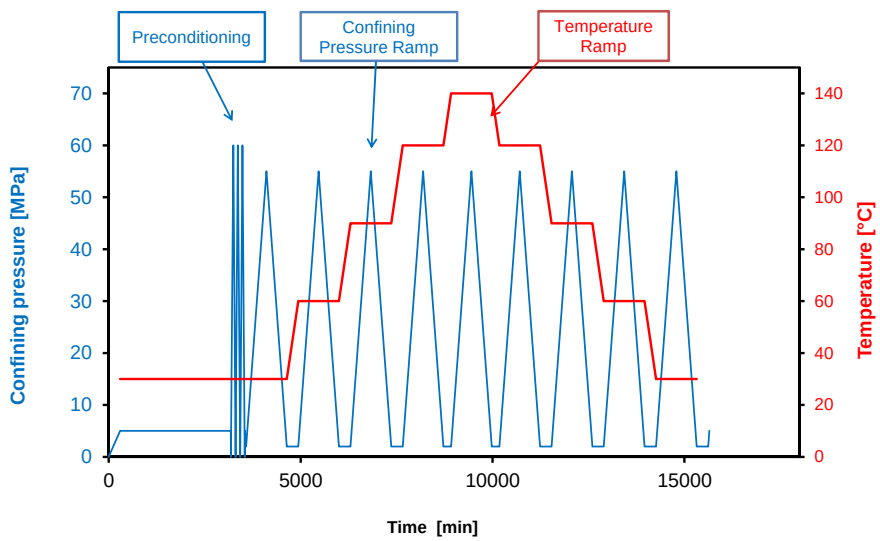

Figure 2: Experimental procedure. The confining pressure was cycled from 2 to 55 MPa and pore pressure maintained at constant pore pressure of 1 MPa. Each pressure cycle is composed of an upward ramp, a plateau and a downward ramp. The temperature increased step wise and stayed constant when cycling confining pressure.

2.2.2 Dynamic tests

The ultrasonic sources and detectors were piezoelectric transducers and were mounted on the upper and lower endcaps. The compressional and shear wavelets were recorded in the axial direction, while performing the static tests, at steps of 5 MPa. A 500 kHz sinusoidal perturbation voltage pulse to the transmitting transducer generated the acoustic signal. A calibration experiment was performed to control the coupling between transducers and the sample and to determine the delay times. Aluminium samples with different length of 40, 60, 80, and 100 mm were employed to measure the transient time. The delay times (t_{op}) and (t_{os}) for v_p and v_s were calculated by extrapolation of travel times to zero length. Measured waveform arrival times contain a system delay time that depends on the wiring configuration, endcap, and crystal pair. First, the onset time of arrival for compressional and shear waves were determined using the Akaike Information Criterion (AIC) as described by Akazawa (2004) and Kurz et al. (2005). The

AIC-picker is a statistical function for which its global minimum defines the onset time of the signal (see Fig.3):

$$AIC(J) = J.\log(var(R(1,J))) + (N-J-1).\log(var(R(1+J,N))) \tag{13}$$

This formulation applies two sliding ranges (windows) to the signal, where J is a counter range through the signal and N is the total number of data. log and var denote the logarithm and variance functions and $R(a,b)$ determines the interval range of recorded voltage. Therefore, a program was written to detect

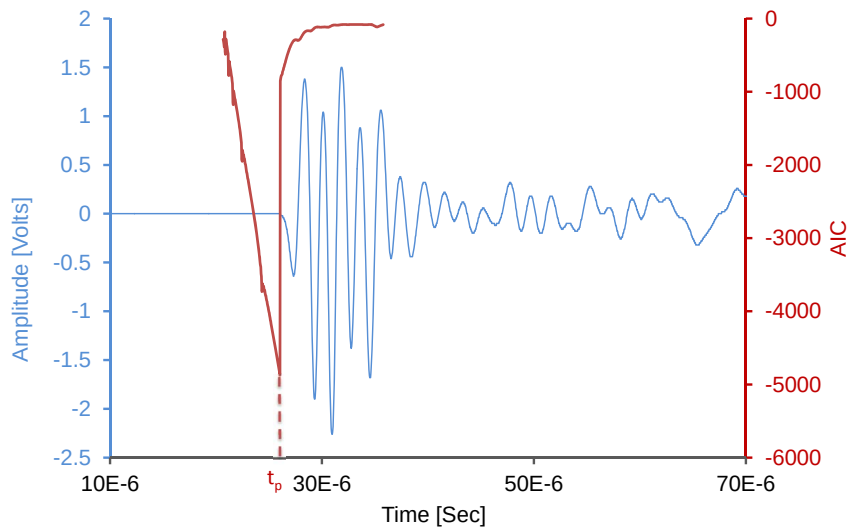

Figure 3: Detecting the onset time of arrival was performed by employing the Akaike Information Criterion (AIC). The minimum value of the AIC function corresponds to the first motion of the wave.

the arrival times automatically. The accuracy of arrival times was examined by plotting all the wavelets together and by tracking the onset times. Afterwards, the net arrival times through the sample were determined by correcting for delay times. Then, the velocities were calculated by the strain-corrected length divided by the net traveltimes.

The dynamic elastic moduli, acoustic velocities and density, for homogeneous isotropic elastic materials, are related by the following equations: the Poisson's ratio is expressed as:

$$\nu = \frac{v_p^2 - 2v_s^2}{2(v_p^2 - v_s^2)} \tag{14}$$

The Young modulus is:

$$E = \frac{\rho_b v_s^2 (3v_p^2 - 4v_s^2)}{v_p^2 - v_s^2} \tag{15}$$

The bulk modulus is:

$$K = \rho_b v_p^2 - 4/3\rho_b v_s^2 \tag{16}$$

3 Results

The drained hydrostatic experiments were employed to investigate the static and dynamic elastic moduli of Flechtinger sandstone at different temperature levels of 25, 60, 90, 120, and 140°C. Figure 4 shows

the microscopic image of Flechtinger sandstone after performing the experiment. Two features are distinguishable: narrow pores and induced cracks due to thermal and mechanical loading. The static bulk moduli were determined by calculating the tangent slope of stress-strain curves $K_d = \left(\partial \hat{P}/\partial \varepsilon\right)_T$. The dynamic elastic moduli were determined by the velocity of acoustic waves (Eqs. 14, 15, 16). In the following, first the analysis of the static elastic moduli will be presented, then the results of the dynamic tests will be illustrated, and finally the results will be discussed.

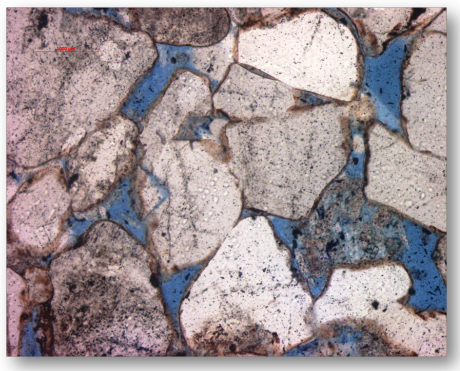

Figure 4: Evidence of induced cracks and damage in a thin section of Flechtinger sandstone after performing the experiment. The visible pores are often flat and narrow.

3.1 Static elastic moduli and poroelastic constants

The drained poroelastic parameters were obtained by performing an hydrostatic tests at isothermal conditions. The unjacketed bulk modulus K_s was theoretically and experimentally examined to be 41.2 GPa (Hassanzadegan et al., 2012). Figure 5 shows the stress-strain curves at different temperature levels. The stress-strain curves are nonlinear and follow the behavior described by Brace (1965) and Walsh (1965). The Flechtinger sandstone showed inelastic behavior. The higher the temperature, the more significant was the inelastic behavior. Figure 6 shows the volumetric variation in the fluid content of the rock at different temperatures as a function of volumetric strain. At 120°C and 140°C the slope of the unloading path was higher than the loading path at high stress regime.

The tangent drained bulk modulus was derived by the derivative of effective pressure with respect to strain. At the initial part of the unloading path, the drained bulk modulus of the rock appeared to be stiffer (Figure 7). The strain measurement accuracy meets the requirement for calibration according to ISO 9513 class 0.5, where the strain measurement accuracy is ± 0.5% of reading or ± 1μm of the indicated value, whichever is larger. The pressure measurement was quite precise with 0.001 MPa deviation. The error involved in calculating drained bulk modulus was estimated by Eq. 17 to vary between 22 to 35 MPa .

$$\left(\frac{\Delta K_d}{K_d}\right)^2 = \left(\frac{\Delta P}{P}\right)^2 + \left(\frac{\Delta \varepsilon_b}{\varepsilon_b}\right)^2 \tag{17}$$

The porosity evolution was measured by two methods: (I) An indirect measurement (Eq. 5), where the porosity is characterized by the compression of the bulk volume V_b and the solid grain volume V_s, and (II) a direct method (Eq. 3) which monitors the pore volume evolution by direct measurement of expelled pore fluid into the water pumps. Figure 8 shows a comparison between direct and indirect porosity at 25 °C. The direct measurement of porosity shows a larger amount of variation in porosity. A comparison

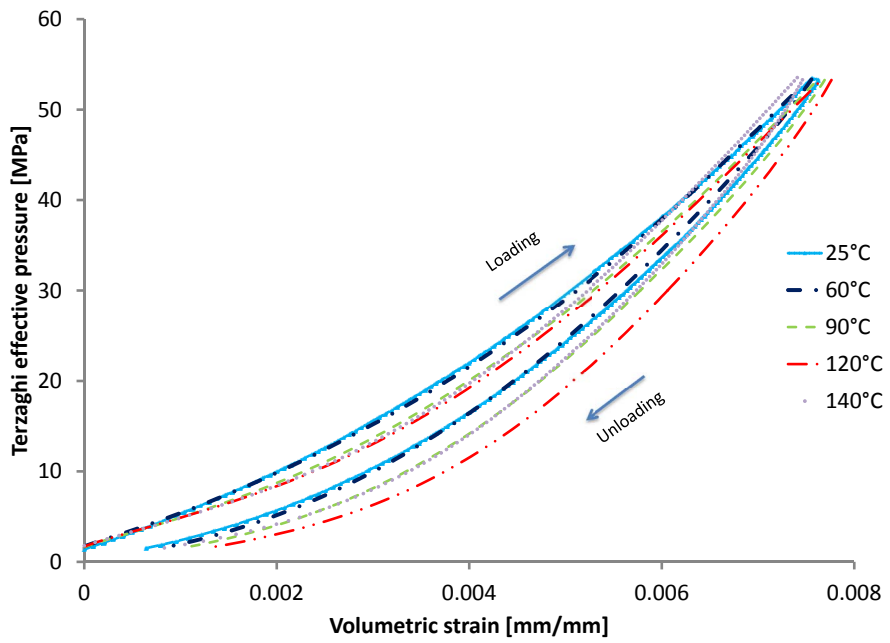

Figure 5: Terzaghi effective pressure versus volumetric strain. The pore pressure was maintained constant at a value of 1 MPa and confining pressure was cycled to 55 MPa.

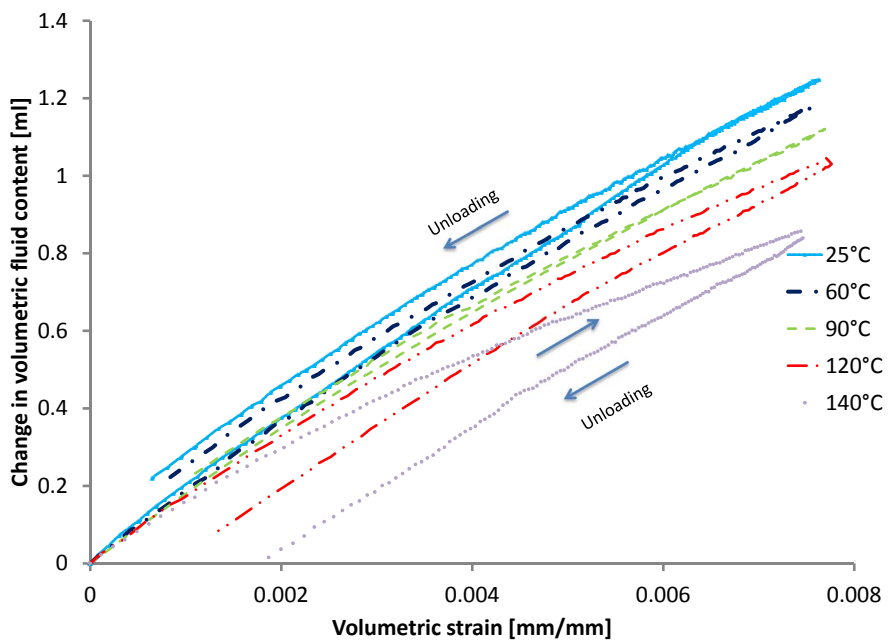

Figure 6: Change in the volumetric content due to changes in the bulk volumetric strain at a constant pore pressure of 1 MPa.

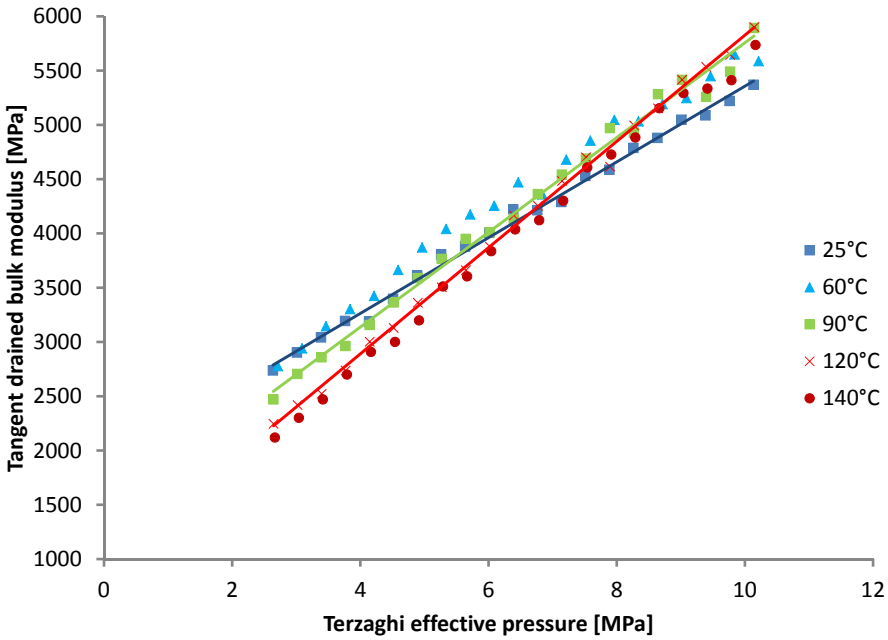

(a) The unloading tangent drained bulk modulus in low stress regime.

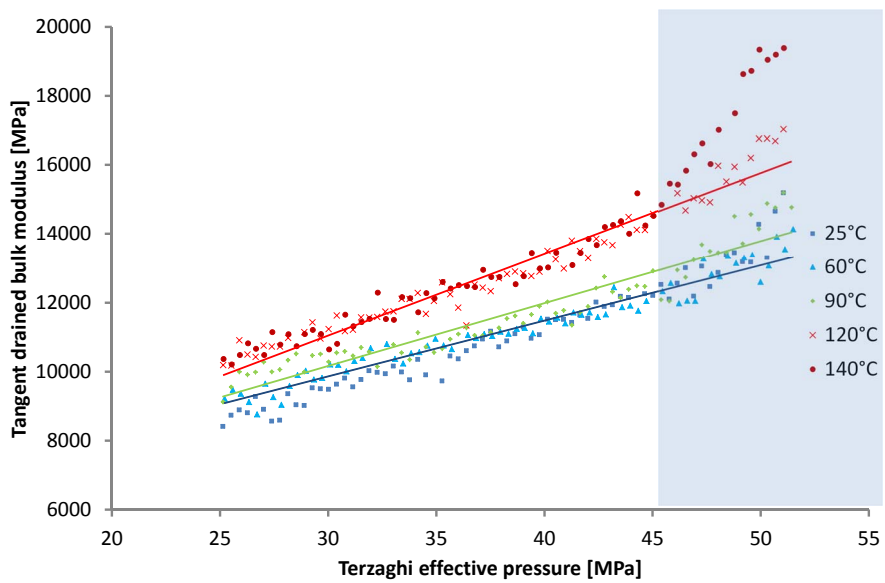

(b) The unloading tangent drained bulk modulus in high stress regime.

Figure 7: The unloading tangent drained bulk modulus as a function of effective pressure. The temperature dependence of the drained bulk modulus was different at low and high effective pressures (relaxed and confined states).

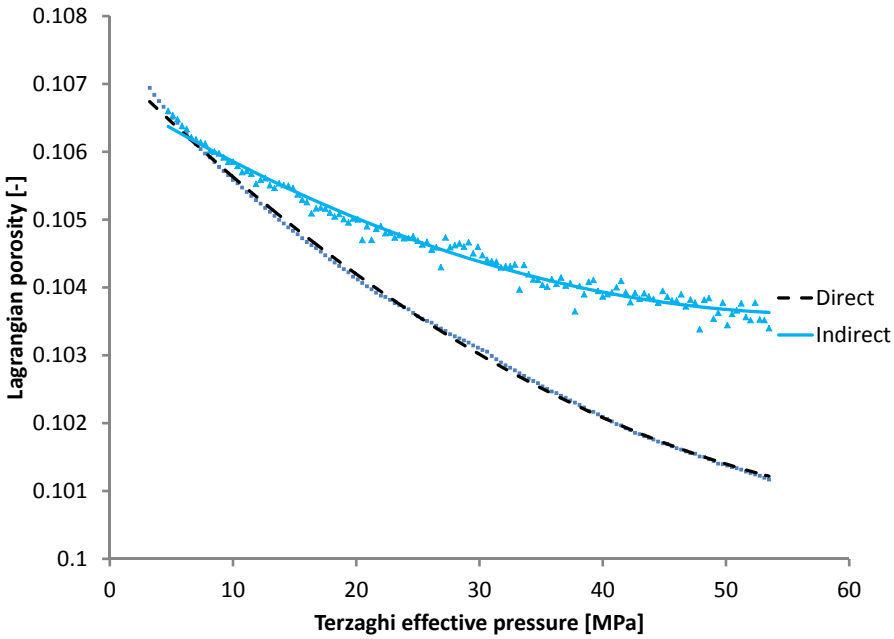

Figure 8: A comparison between direct (Eq. 3) and indirect porosity (Eq. 5) as a function of Terzaghi effective pressure for the loading path and 25 °C. Pore pressure was maintained constant at 1 MPa.

between loading and unloading porosity evolution (indirect method) is displayed in Figures 9(a) and 9(b).

It was assumed that inelastic bulk strain ε_b^{in} and pore strain are equal and the initial porosity was corrected for inelastic deformation in both samples ($V_p = V_p^i - \varepsilon_b^{in} \times V_p^i$). V_p^i is the initial pore volume at the beginning of each cycle (see Table 2).

Table 2: The inelastic deformation of Flechtinger sandstone specimen (FLG05).

Temperature [°C]	Bulk inelastic strain ε_b[-]$\times 10^{-4}$	Porosity n[%]
25	5.08	10.75
60	9.14	10.71
90	9.07	10.63
120	12.3	10.54
140	9.4	10.43

Figure 10 shows the loading spectrums, i.e. the aspect ratio distribution function of porosity $C(a)$, at different temperatures. The shape of the spectrums is similar to log-normal distribution functions. Figure 10 shows that the peaks of spectrums at 25, 60 and 90 °C are identical while at 120 and 140 °C the peak of the spectrum shifts towards the lower aspect ratio. That is, the density of the narrow or flat cracks was increasing with increasing temperature at low pressures. Moreover, the spectrum curves cross each other at an aspect ratios approximately equal to 0.00033. Each crack with an initial aspect ratio a is related to a minimum pressure which is required to close it. That is, the 0.00033 aspect ratio corresponds

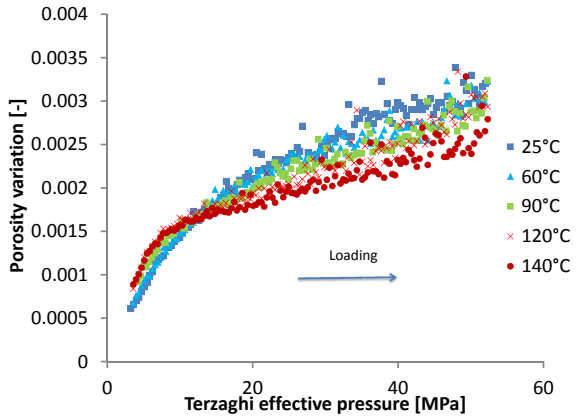

(a) The porosity variation for the loading path

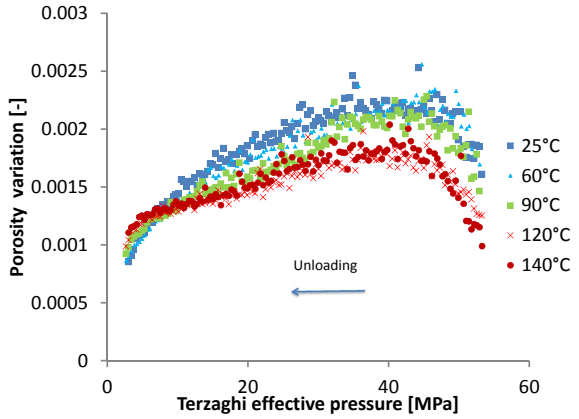

(b) The porosity variation for the unloading path

Figure 9: The indirect measurement of porosity variation ($\phi^0 - \phi$) as a function of Terzaghi effective pressure (Eq. 5).

to a 25 MPa closing pressure. A closure pressure of 25 MPa and an aspect ratio of 0.00033 characterize the thermoelastic inversion point where the temperature dependence of drained bulk modulus changes its sign.

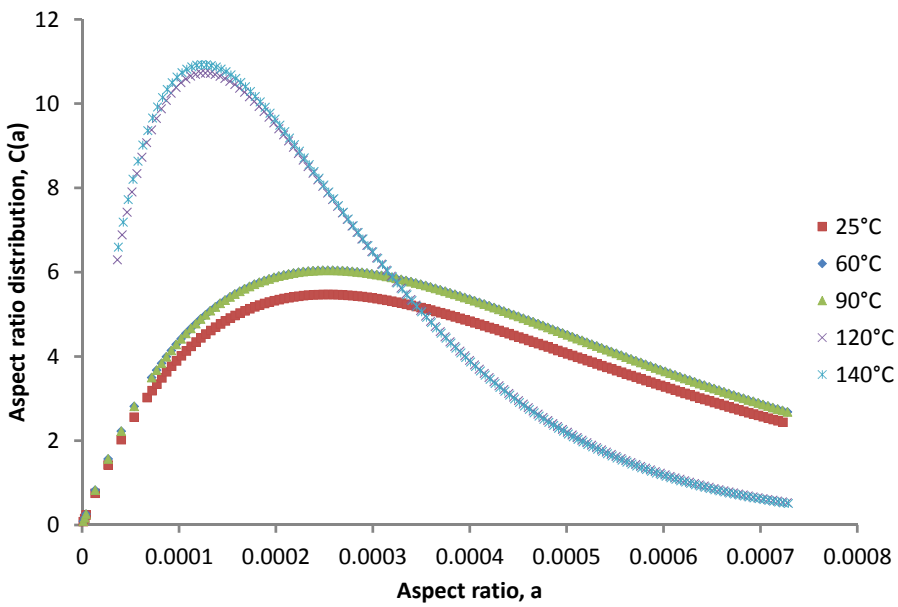

Figure 10: Loading aspect ratio distribution function at different temperatures (Eq. 10). The distribution function shifted towards lower aspect ratios at 120 and 140 °C.

Table 3 presents the loading drained bulk modulus parameters. The analysis of loading stress-strain curves (Eqs. 9 and 10) shows that the loading characteristic closure pressure is higher at 25, 60 and 90 °C and decreases at 120 and 140 °C (see Table 3).

Table 3: Loading bulk modulus parameters of Flechtinger sandstone (FLG05) at given temperatures. The description of parameters is given at section 1.1.2.

Temperature	K_d^∞	K_d^i	$\hat{P}$	$\hat{a}$	ϕ_{crack}
[°C]	[GPa]	[GPa]	[MPa]	[-]	[-]
25	11.70	3.50	18.80	0.000253	0.00376
60	13.07	3.36	18.88	0.000254	0.00417
90	13.07	3.36	18.88	0.000254	0.00417
120	10.56	2.05	9.40	0.000126	0.00369
140	11.19	2.04	9.30	0.000125	0.00372

Figure 11 shows the unloading spectrums at different temperatures. The peak of $C(a)$ increases with increasing temperature at the unloading path. Moreover, the inversion of the spectrum curves appears at a lower aspect ratio of approximately 0.0002 corresponding to 14.9 MPa. Except for 60 °C the crack porosity was increasing when the temperature was increased (see Table 4). The loading and unloading thermoelastic inversion pressures were higher than characteristic closure pressures. The crack porosity and its evolution was approximated by numerical integration and calculation of the area under spectrum

curve (Eq. 11). First of all, the total crack porosity was calculated by employing fitting parameters K_d^i, K_d^∞ and $\hat{P}$. At each pressure level the surface area (definite integral) was calculated by the trapezoidal rule $(C(a_1) + C(a_2)) \times (a_2 - a_1)/2$ for all data points. Then, the porosity of closed cracks was calculated by passing through pressure levels. Having obtained the total crack porosity and cumulative porosity of the closed cracks, the porosity of cracks which are open at each pressure level can be obtained. Figure 12 shows the unloading crack porosity as a function of confining pressure. The crack porosity decreased with increasing confining pressure and most of the cracks were closed at initial part of unloading. At confining pressures higher than 30 MPa the crack porosity was higher for higher temperatures. At pressures lower than 30 MPa, the crack porosity was decreased by increasing temperature at a given confining pressure (25, 60 and 90 °C spectrums). The 120 and 140 °C spectrums show that initial crack porosities have been increased (see Fig.10).

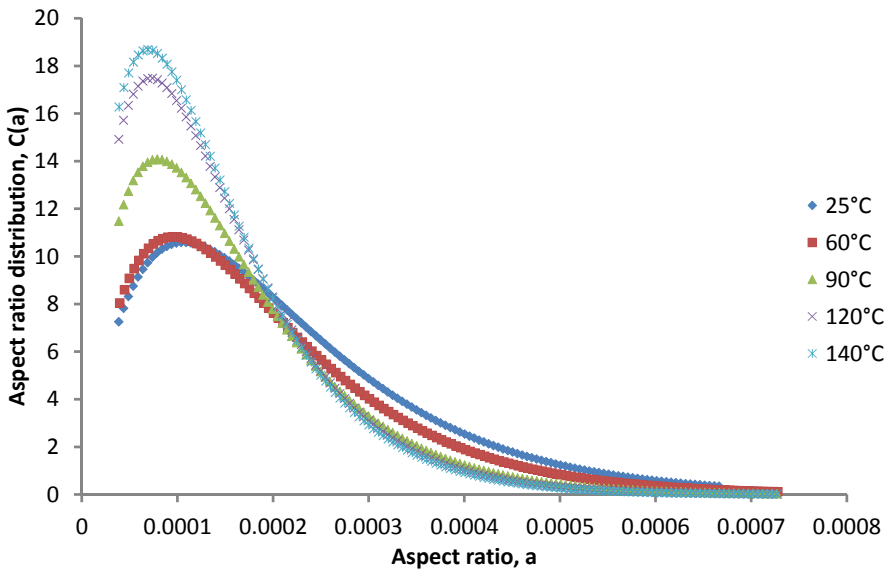

Figure 11: Unloading aspect ratio distribution function at different temperatures (Eq. 10).

Table 4: Unloading bulk modulus parameters of Flechtinger sandstone (FLG05) at given temperatures (see section 1.1.2 for description of parameters.)

Temperature	K_d^∞	K_d^i	$\hat{P}$	$\hat{a}$	ϕ_{crack}
[°C]	[GPa]	[GPa]	[MPa]	[-]	[-]
25	11.25	2.15	8.57	0.000107	0.00323
60	10.69	2.05	7.17	0.000096	0.00283
90	10.77	1.65	5.92	0.000079	0.00304
120	11.63	1.38	5.40	0.000072	0.00343
140	11.22	1.30	5.19	0.000070	0.00353

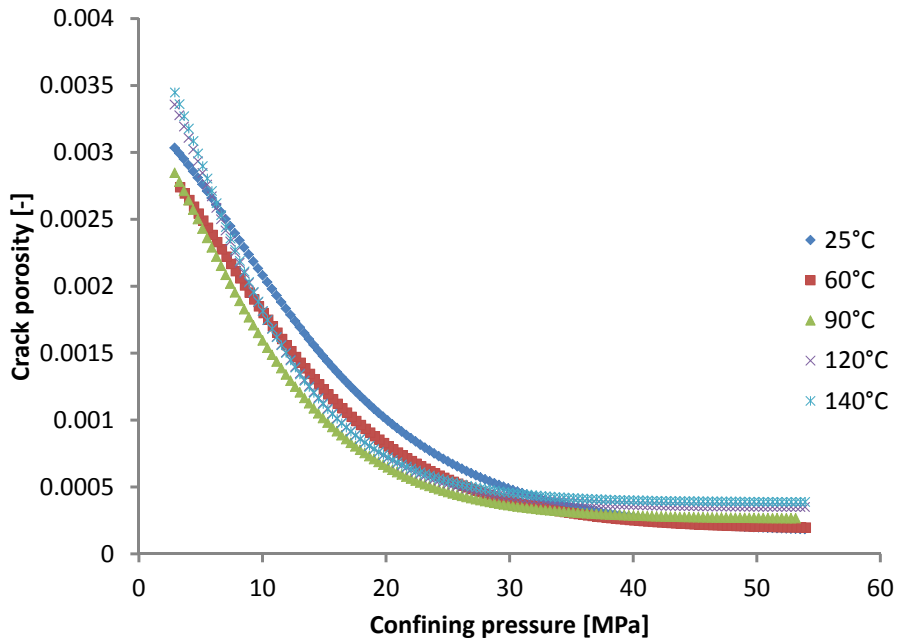

Figure 12: Unloading crack porosity as a function of confining pressure at different temperatures (Eq. 11).

3.2 Dynamic elastic moduli

Acoustic velocities (v_p and v_s) in concert with bulk density provide the essential information to determine the dynamic elastic parameters of ideal isotropic materials (Simmons and Brace, 1965). Figures 13(a) and 13(b) illustrate the increase in v_p and v_s with increasing effective pressure and the irreversibility during loading and unloading. The compressional wave velocity is inversely proportional to porosity. Thus, when effective pressure increases, porosity decreases and accordingly the compressional wave velocity increases. The hysteresis in acoustic velocity measurements was less pronounced than for stress-strain curves. The evolution of acoustic velocities with respect to effective pressure was nonlinear and both v_p and v_s changes became progressively smaller with increasing effective pressure. A power law equation (Eq. 12) according to Somerton (1980) was found to be the best fit to the laboratory data. The exponent e was calculated to be approximately 30, classifying the Flechtinger sandstone as a fairly hard rock.

The dynamic elastic moduli changed with temperature and effective pressure. Figures 14(a) and 14(b) show the evolution of Poisson's ratio with respect to effective pressure and temperature for the loading and unloading paths, respectively. The dynamic Poisson's ratio was derived from acoustic velocities (Eq. 14). Poisson's ratio decreased sharply in the low stress regime and linearly in the high stress regime. While Poisson's ratio was decreasing with increasing pressure, its temperature dependence was pressure dependent. Furthermore, the value of dynamic drained Poisson's ratio was found to be lower than the value of static Poisson's ratio. The loading and unloading dynamic Poisson's ratios were compatible.

As effective pressure increased the Young's modulus increased sharply at relaxed state and gradually afterwards (Fig.15(a)). The loading isotherms were converging up to a transition point and diverging afterwards. The unloading dynamic Young's moduli (Fig.15(b)) were determined at effective pressures lower than 25 MPa and were compatible with the loading isotherms.

Figures 16(a) and 16(b) show the loading and unloading bulk modulus as a function of effective pressure at different temperatures.

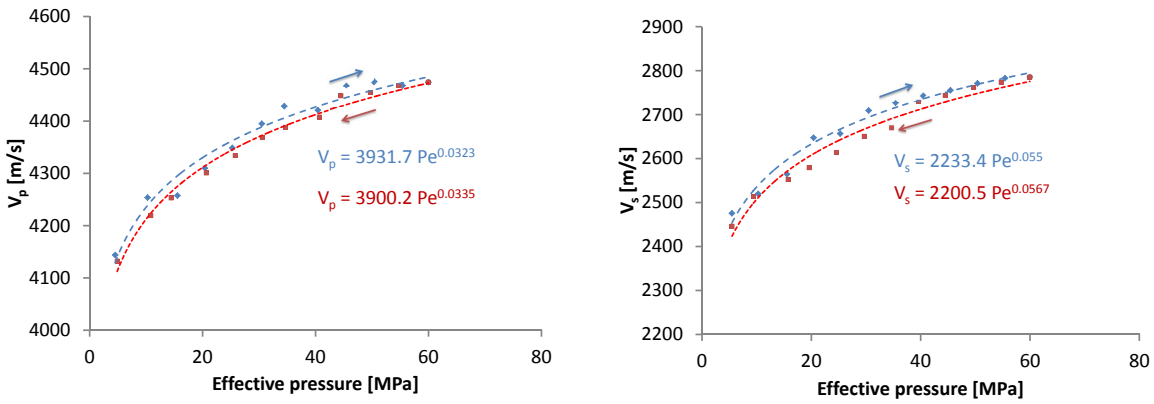

(a) Compressional wave velocity.

(b) Shear wave velocity.

Figure 13: Acoustic wave velocities as a function of Terzaghi effective pressure at loading and unloading paths. The sample was water saturated and the experiment was performed at a constant temperature of 25°C.

4 Discussion

In general, rock can be portrayed either as a granular porous medium or a cracked medium. Accordingly, different effective medium theories can be employed to relate the macroscopic and microscopic properties of the rock (Nur and Wang, 1989b). Walsh (1973) stated that stress field within a porous rock subjected to a uniform applied stress or temperature change is non-uniform and elastic deformation differs from grain to grain due to anistropic properties and composition. The Hertizan contact theory predicts the stiffening of compliant grain contacts. Similarly, when a compressive hydrostatic stress is acting on the rock, the cracks tend to close and increase the effective elastic moduli of the rock. The theory of poroelasticity describes the stress-strain relations in a saturated porous medium, however, irrespective of pore geometry. The essential assumptions in drained poroelasticity theory are the connectivity of pore network and a constant pore pressure. In contrast, the crack closure theory formulates the effective properties, e.g. bulk modulus, by considering the pore geometry and its elastic deformation.

The mechanical response of the rock can be characterized either by static or dynamic elastic moduli. Yale and Nieto (1995) investigated the micromechanical basis for the difference between static and dynamic elastic moduli of Flechtinger sandstone. They stated that this difference is primary due to the hysteresis at grain contacts and the type of cementation. While the acoustic waves deform the high aspect ratio pores slightly, because of small strain amplitudes, the large strain amplitudes in static measurements create large deformation of these pores. Therefore, the rock appears stiffer and more rigid in dynamic tests and more compliant and less rigid in static tests (Nur and Wang, 1989b).

The stress-strain curves in static tests (Fig. 5) showed nonlinear mechanical behavior and not all the strains were recovered after unloading (i.e., inelastic deformation). During unloading the strains followed a different path (hysteresis), where some energy dissipates. In summary, the nonlinearity can be assigned to pressure and temperature dependence of material properties, changes in pore geometry, and the applied boundary conditions (Hassanzadegan et al., 2012). Figure 6 shows the volumetric variation in the fluid content. At 120°C and 140°C the slope of the unloading path was higher than for the loading path. The unloading crack porosity and aspect ratio analysis showed that the crack porosity has increased at these temperatures (see Table 4).

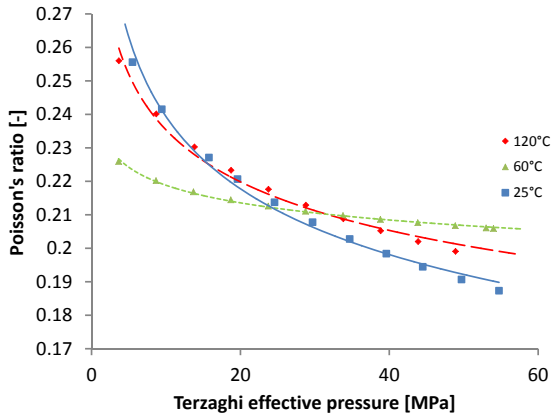

(a) Loading Poisson's ratio.

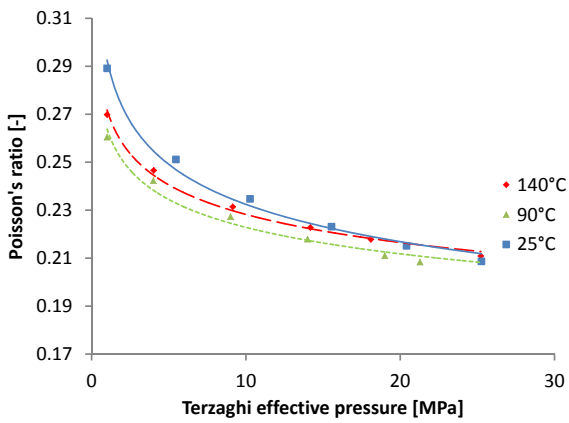

(b) Unloading Poisson's ratio.

Figure 14: Dynamic Poisson's ratio as a function of Terzaghi effective pressure.

4.1 Temperature dependence of the drained bulk modulus

The thermomechanical response of the Flechtinger sandstone can be categorized into four different regimes, a low stress regime (effective pressures less than 9 MPa), a transitional regime, a high stress regime (effective pressures higher than 25 MPa), and an inelastic regime at the initial part of the unloading path (Fig. 17). The low stress regime is characterized by the opening and closing of the low aspect ratio pores (cracks) where narrow cracks are compliant and close easily compared to rounded pores. The volumetric deformation of the skeleton (extrinsic property) is dominant in the low stress regime, however the compression of solid grains does not prevail. In addition, the tangent drained bulk modulus decreased with increasing temperature ($\frac{\partial K_d}{\partial T} < 0$). The other characteristics of the low stress regime is a steepened variation in acoustic velocities and dynamic moduli. The high stress regime is better characterized by the dynamic Poisson's ratio where the temperature dependence of Poisson's ratio changes its sign at approximately 25 MPa effective pressures. The high stress regime can be recognized by a positive temperature dependence of the drained bulk modulus ($\frac{\partial K_d}{\partial T} > 0$), where the the narrow cracks are closed and the rounded pores are stiffer.

Each pressure cycle consisted of a loading path, a plateau, and an unloading path. Therefore, the initial part of the unloading path (55 MPa to 45 MPa) is rather influenced by an inelastic behavior of the

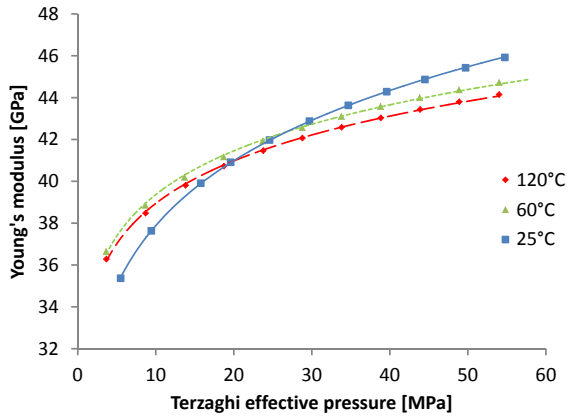

(a) Loading Young modulus.

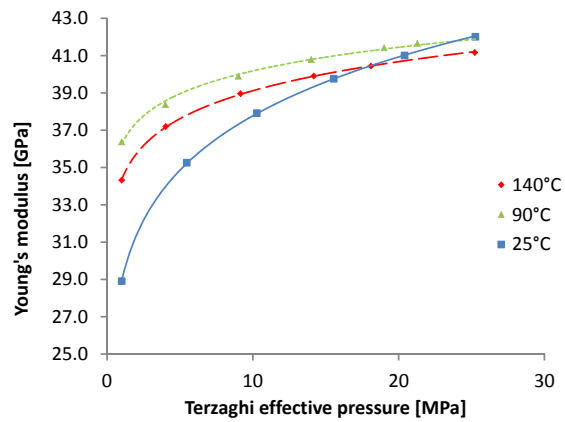

(b) Unloading Young modulus.

Figure 15: Dynamic Young's modulus as a function of Terzaghi effective pressure.

sandstone. The unloading aspect ratio distribution functions (Fig. 11) and crack porosity isotherms (Fig. 12) confirm that a higher density of cracks are closed at high pressures. Thus, during the initial part of the unloading path the porosity change was influenced (Fig. 9(b)).

4.2 Porosity and crack porosity

Three mechanisms control the fluid mass content variation within the saturated porous rock: elastic deformation, variations in pore pressure and thermal expansion. The direct porosity measurement was performed under the assumption that changes in pore fluid volume are equal to changes in pore volume. A comparison between porosity change derived by Biot-theory (Eq. 3) and the micromechanics theory (Eq. 5) shows that the porosity change predicted by the direct measurement of the expelled fluid is higher (see Fig. 8). This can be explained by the fact that applying external load will induce some pore pressure within the sample (Skempton effect) and bulk deformation is not the only mechanism affecting the variations in fluid content. Both porosities were decreasing by increasing effective pressure.

The porosity variation and crack porosity were calculated by employing theory of poroelasticity and theory of crack closure. The porosity variation ($\phi^0 - \phi$) during loading and for different temperature

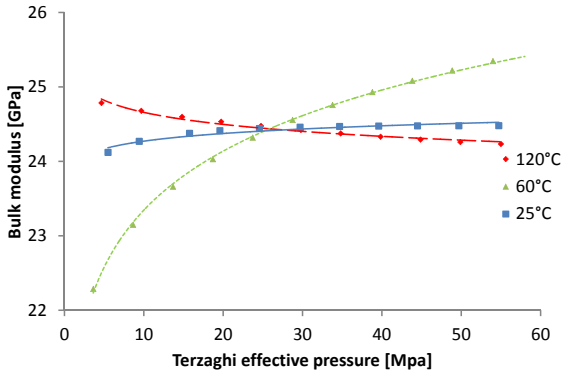

(a) Loading Bulk modulus.

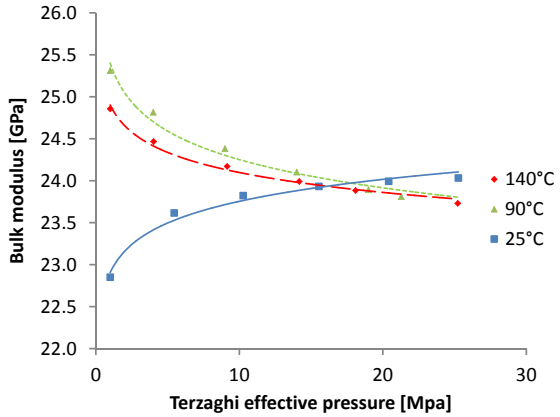

(b) Unloading Bulk modulus.

Figure 16: Dynamic bulk modulus as a function of Terzaghi effective pressure.

levels is shown in Figure 10. The increase in temperature in the low stress regime was accompanied by an increase in porosity variation, while in the high stress regime, the porosity variation decreased with increasing temperature. A comparison of unloading crack porosity concluded that crack porosity was increasing with increasing temperature (Table 4). The determined pore aspect ratio distributions were compatible with those reported for of Boise, Berea and Bandera sandstones (Zimmerman, 1991). However, during cataclastic compaction of Vosges sandstone, the value of aspect ratio was an order of magnitude higher (10^{-3}) due to pore collapse and grain crushing (David and Zimmerman, 2012).

The maximum porosity variation (Fig. 9) and the total crack porosity (Fig. 12) were in the same order of magnitude and were confirming each other. The characteristic closure pressures at loading conditions were higher than at unloading conditions and were decreasing with increasing temperature. That is, the crack distribution shifted towards narrower cracks where they are compliant and would be closed at lower pressures (Fig. 11). The loading and unloading distribution of the aspect ratios could explain the transitional behavior from the low stress regime (crack dominated) to the high stress regime (solid grain deformation) at loading and unloading conditions. The characteristic closure pressures for the loading path (13.8 MPa) was higher than for the unloading path (8.6 MPa) at 25°C. The crack porosity analysis predicted a thermal inversion pressure of approximately 30 MPa (Fig. 12). At pressure higher than 30 MPa, most of the compliant cracks were closed and the stress-strain relation is linear.

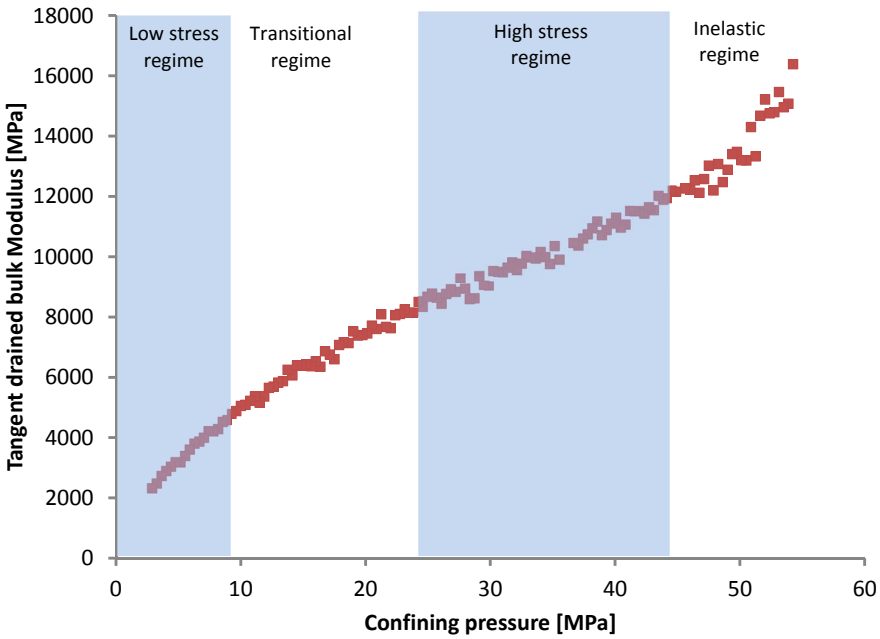

Figure 17: The temperature and pressure dependence of static and dynamic elastic moduli classifies the thermomechanical behavior of Flechtinger sandstone into four different regimes.

4.3 Dynamic moduli

Zang and Berckhemer (1993) investigated the source of anisotropy in physical properties of different rock types. The main sources were found to be the crack induced anisotropy and textural induced anisotropy. Dillen (2000) observed a transition in mechanical behavior of Flechtinger sandstone while investigating the dynamic elastic moduli in hydrostatic tests. He distinguished two approximately linear regimes with a transition at 27 MPa during the loading and unloading paths. He discussed it in terms of progressive crack closure or sliding of cracks that allowed this transitional behavior. Moreover, he analyzed the P-wave anisotropy and concluded that at effective pressures less than 10 MPa, the anisotropy due to opening and closure of cracks is dominant (stress induced anisotropy), while at higher effective pressures, the anisotropy due to layering of the Flechtinger sandstone (texture induced anisotropy) prevails.

The acoustic velocities changed rapidly at low effective pressures of up to 9 MPa which can be assigned to a rapid closure of cracks and low aspect ratio pores due to a volumetric change in skeleton properties (extrinsic properties). The temperature dependence of Poisson's ratio was investigated by measuring the dynamic elastic moduli (see Fig. 14(a)). The change in Poisson's ratio was more pronounced at lower effective pressures of 25 MPa and was approximately constant afterwards. The temperature dependence of loading Poisson's ratio, Young's modulus and bulk modulus differed at low and high effective pressures i.e. below and above 25 MPa. The observed transition in thermo-mechanical behavior is compatible with what has been reported by Dillen (2000).

5 Conclusion

The analysis of acoustic velocity measurements, crack porosity and tangent drained bulk modulus was performed for Flechtinger sandstone. First, the temperature dependence of the bulk modulus was de-

termined by the drained bulk modulus analysis. In conclusion, the mechanical behavior of Flechtinger sandstone was categorized in a low stress, a transitional, a high stress, and an inelastic regime. The crack porosity analysis showed that the aspect ratio distribution functions are different during loading and unloading. The low aspect ratio cracks (narrow cracks) are more compliant and would close at lower effective pressure, however the high aspect ratio cracks are stiffer. The characteristic closure pressure during loading (13.8 MPa) was higher than during unloading (8.6 MPa).

The effect of temperature on crack porosity was quantified where the crack porosity increased with increasing temperature due to a mismatch between thermal expansions of adjacent minerals. The porosity variation derived by poroelastic theory was in the same range as obtained by the crack porosity analysis. The porosity variation showed an inversion behavior, i.e. the porosity variation increased with an increase in temperature at low effective pressures and decreased at high effective pressures. The inversion pressure was higher than loading and unloading characteristic closure pressures.

The static isotherms at 120°C and 140°C showed the creation of narrow cracks which resulted in a decrease of the dynamic bulk moduli. Moreover, both compressional and shear wave velocities were increasing with increasing pressure. The temperature derivative of the static unloading drained bulk modulus and the loading dynamic moduli changed the sign at an effective pressure of 25 MPa.

Chapter 5

Originally published in the *Pure and Applied Geophysics*

The poroelastic description of permeability evolution

Alireza Hassanzadegan, Günter Zimmermann

Abstract

The pore pressure changes, due to injection and production of water into a geothermal reservoir, result in changes of stress acting on reservoir rock and consequently changes in mechanical and transport properties of the rock. The bulk modulus and permeability were measured at different pressures and temperatures. An outcropping equivalent of Rotliegend reservoir rock in North German Basin (Flechtinger sandstone) was employed to perform hydrostatic tests and steady state fluid flow tests. Permeability measurements were carried out while cycling confining pressure at a constant downstream pressure of 1 MPa where the stress dependence of permeability was determined. Meanwhile the temperature was increased stepwise from 30 °C to 140 °C. The crack porosity was calculated at various temperatures. While the pore volume changes of the cracks are not significant but control fluid flow pathways and consequently the permeability of the rock. A new model was derived which relates the microstructure of porosity, stress-strain curve and permeability. The porosity change was described by the first derivative of stress-strain curve and permeability evolution was ascribed to crack closure and was related to the second derivative of strain-stress curve. The porosity and permeability of Flechtinger sandstone decreased by increasing the effective pressure and after each pressure cycle.

1 Introduction

There is a long-standing interest in understanding the interrelation between deformation and transport properties of porous rock in civil and reservoir engineering. The permeability is quite challenging as it varies more than 11 orders of magnitudes for different rock types and stress conditions (Brace, 1980). The stress dependence of permeability has been studied experimentally by some researchers (Zoback and Byerlee, 1975; Bernabe, 1986, 1987; David et al., 1994). Bernabe (1986, 1987) observed a large hysteresis in permeability at loading and unloading paths for different rock types. David et al. (2001) reported a rapid reduction in permeability evolution between 15 to 40 MPa which was assigned to the closure of the cracks. Guéguen et al. (1996) assigned the pressure dependence of permeability of cracked rocks to elastic closure of cracks and crack roughness, where the cracks are compliant and close easily compared to rounded pores.

The interrelation between elastic rock deformation and pore fluid in porous media has been described by poroelasticity theory. Biot (1941, 1956, 1973); Rice and Cleary (1976) derived the constitutive equations that govern the elastic behavior of the saturated porous rock. The poroelasticity theory provides a very useful relationship between effective pressure, strain and porosity change (Carroll, 1980). The inelastic deformation and its relation to permeability have been the subject of many studies. David et al. (2001) stated that increase in crack density during the loading path contributes to the bulk porosity but has no enhancement effect on the permeability beyond the grain crushing. Heiland and Raab (2001) and Heiland (2003) studied the influence of stress, dilatancy, brittle deformation, strain rate, and formation of shear bands on permeability. Fortin et al. (2005) studied the strength of coupling between volumetric strain, elastic properties and permeability during the formation of compaction bands. They concluded that pore collapse pressure is governed by composition of sandstone. A new method for the evaluation

of the porosity-permeability relationship is given by Ghabezloo et al. (2009) where the effect of creep on pore pressure and volume changes has been included.

The correlation between porosity and permeability requires that microstructure of porosity to be known (Guéguen and Dienes, 1989). Morlier (1971) developed a method to relate strain to microstructure of porosity. However, no interrelation between permeability and strain has been developed. The aim of this study is to develop an interrelation between strain, permeability, microstructure of porosity and stress. A new permeability model is introduced which is characterized by spherical pores and penny-shaped cracks imbedded into a solid phase. The permeability model assumes that spherical pores are connected by cracks.

2 Theoretical background

The poroelastic theory assumes a quasi static deformation where the state variables (temperature, pressure, etc.) are in thermodynamic equilibrium. However, if the state variables vary with time the system undergoes a process. The number of state variables required to characterize a process might be larger than thermodynamic equilibrium, for example in describing the fluid flow in porous media, viscosity and permeability are required. Viscosity is a physical property of the fluid and permeability is a property of porous media.

2.1 Permeability

Permeability is a transport property which allows to quantify the fluid flow in porous media and is a measure of how easily fluid flows through a rock (Guéguen et al., 1996). Furthermore, permeability is a measure of the geometry of the pores (pore dimension) and their interconnections (Brace, 1978). It is the intricate relation between the pore geometries and their interconnectivity which makes the permeability modeling in terms of microstructure a challenging task (Sarout, 2012).

Bear (1988) described the conceptual models employed to derive Darcy's law:

$$q = -\frac{k}{\eta}\nabla(P_p - \rho_f g z) \tag{1}$$

where ∇ is a vector differential operator (gradient). z is the vertical distance and points downward. The proportionality constant $\frac{k}{\eta}$, mobility, includes the fluid viscosity η and intrinsic permeability k. q is the fluid flux vector,g is the gravity acceleration and ρ_f is fluid density. If the fluid density considered to be constant, a potential energy function $\varphi = \frac{P_p}{\rho} - gz$, energy per unit mass of the fluid, can be defined such that

$$q = -(\frac{k\rho_f}{\eta})\nabla\varphi \tag{2}$$

A general relation between porosity and permeability is given by Bear (1988):

$$k = f(s)f(\phi)R^2 \tag{3}$$

where $f(s)$ is a shape function, $f(\phi)$ is a porosity function and R is a hydraulic radius defined as cross sectional area divided by wetted perimeter (Sisavath et al., 2000). The Kozeny-Carman permeability (Carman, 1956) was derived by employing Hagen-Poiseuille equation for steady laminar flow through a bundle of capillary tubes where the permeability can be expressed in terms of porosity ϕ, specific surface area S or a flow path characteristic length d, and tortuosity τ :

$$k = \frac{c\phi^3}{\tau^2 S^2} \tag{4}$$

where c is a geometric factor. The specific surface area, the pore surface per bulk volume of porous media, is a dominant parameter in permeability models which contributes in shape factor. A particular extension of this equation is to consider a packed bed of spheres with $S = \frac{3}{2}\frac{1-\phi}{d}$ and $\tau = 1$, which results in:

$$k = c_1 \frac{\phi^3}{(1-\phi)^2} d^2 \tag{5}$$

where c_1 includes the geometric factor and the factor of $(\frac{3}{2})^2$. The assumption $\tau = 1$, laterally states that all the pores are part of a connected network (infinite path).

2.2 Poroelasticity

The key concepts in poroelasticity theory underly the following equations, describing the evolution of two kinematic quantities: bulk strain of the porous rock ε_b and change in fluid mass content m in terms of their conjugate dynamic quantities: confining pressure P_c and pore pressure P_p (Detournay and Cheng, 1993):

$$\varepsilon_b = \frac{P_c - \alpha P_p}{K_d} \tag{6a}$$

$$m - m_0 = -\frac{\alpha \rho_0}{K_d}\left[P_c - \frac{1}{B}P_p\right] \tag{6b}$$

B and α are Skempton and Biot coefficients, respectively. K_d is drained bulk modulus and ρ_0 is fluid density at reference condition. These two equations describe the fluid rock interaction under quasistatic conditions for a representative elementary volume (REV). That is, an increase in pore pressure dilates the rock, an increase in fluid mass content causes a rise in pore pressure and the fluid mass content decreases due to applied pressure which results in volume compression (Detournay and Cheng, 1993). The inertial forces and other high frequency effects are neglected and it is assumed that the characteristic length of REV is much larger than pore scale. Carroll and Katsube (1983) described the porosity evolution in terms of the drained bulk modulus and effective pressure:

$$d\phi = \left(\frac{1-\phi^i}{K_d} - \frac{1}{K_s}\right) dP' \tag{7}$$

where $P' = P_c - P_p$ is Terzaghi effective pressure and ϕ^i is initial porosity.

2.3 Crack closure and porosity

In a porous rock, the bulk modulus is no longer equal to the bulk modulus of solid grains K_s but are a function of porosity ϕ. Walsh (1965) derived the effective bulk modulus of the rock in terms of the bulk modulus of solid phase K_s and the rate of change in porosity with external pressure. For a two phase porous rock which is consisted of penny shaped cracks imbedded into the solid phase, the effective bulk modulus of the porous media K_d was derived by Walsh (1965) to be:

$$K_d = K_s / \left[1 + \left(\frac{16}{9}\right)\left(\frac{1-\nu_s^2}{1-2\nu_s}\right)\sum \frac{c^3}{V_b}\right] \tag{8}$$

where ν_s is the Poisson's ratio of the solid grains and V_b is the bulk volume. The summation in Eq.8 is over all open cracks. The aspect ratio of penny-shaped (oblate spheroid) cracks, $a = b/c$ with $b << c$, contains the microstructural information of the pore geometry, with semi minor axis b (crack aperture) and semi major axis c (crack radius).

The change in aperture of a 2D-penny shaped crack can be derived by elasticity theory (Walsh, 1965):

$$b = b_0 \left[1 - \frac{2(1-\nu_s^2)}{aE} P\right] \tag{9}$$

where E is the Young's modulus. The Eq.9 suggests that a penny-shaped crack of initial aspect ratio $a_0 = b_0/c_0$ will fully close when pressure reaches a closure pressure P^*.

Having the hydrostatic compression test performed, the initial crack porosity and crack porosity change can be calculated from deviation of bulk volumetric strain from the volumetric strain of the solid matrix (Walsh, 1965):

$$\Delta\phi_c = \frac{\Delta V_c}{V_b} = \int \frac{1}{K_d} dP' - \int \frac{1}{K_s} dP' = \varepsilon_b(P') - \varepsilon_s(P') \tag{10}$$

The crack porosity at each pressure level, less than that required to close all the cracks, can be calculated by determining how many is closed in passing through each pressure level. Morlier (1971) developed a method to derive the aspect ratio distribution function where the crack density whose initial aspect ratio lies between a and $a + da$ is given by $d\Gamma(a) = -\gamma(a)da$. $\gamma(a)$ and $\Gamma(a)$ represent the aspect ratio distribution function and the cumulative distribution function of open cracks, respectively.

$$\gamma(a) = -\frac{d\Gamma(a)}{da} = \frac{-3}{4\pi}\left[\frac{3\pi K_s(1-2\nu_s)}{4(1-\nu_s^2)}\right]^2 \left[\frac{d^2V}{dP^2}\right]_{P^*} \tag{11}$$

where the derivative $\left[\frac{d^2V}{dP^2}\right]_{P^*}$ should be evaluated at the crack closing pressure P^*:

$$P^* = \left[\frac{3\pi a K_s(1-2\nu_s)}{4(1-\nu_s^2)}\right] \tag{12}$$

Zimmerman (1991) proposed an exponentially decreasing function for evolution of bulk modulus (first derivative of strain-stress curve):

$$\frac{1}{K_d} = \frac{1}{K_d^\infty} + \left[\frac{1}{K_d^i} - \frac{1}{K_d^\infty}\right] \exp(-\frac{P'}{\hat{P}}) \tag{13}$$

where $\hat{P}$ is a characteristic closure pressure corresponding to an aspect ratio at the maximum of $\gamma(a)$. The peak of $\gamma(a)$ represents the cracks with a higher population. The superscript i refers to relaxed state at low effective pressures and the superscript ∞ refers to confined state at high effective pressures. The second derivative of strain-stress curve can be derived by differentiation of Eq.13 with respect to pressure at corresponding closing pressure (Eq.12). Inserting the second derivative in Eq.11 leads to:

$$\gamma(a) = \left[\frac{9K_s(1-2\nu_s)}{16\hat{a}(1-\nu_s^2)}\right] \left[\frac{1}{K_d^i} - \frac{1}{K_d^\infty}\right] \exp(-\frac{a}{\hat{a}}) \tag{14}$$

where $\hat{a}$ is the characteristic aspect ratio evaluated at $\hat{P}$.

Thus, the crack porosity function can be written as:

$$C(a) = \frac{d\phi}{da} = \frac{4\pi a}{3}\gamma(a) = \left[\frac{3\pi K_s(1-2\nu_s)}{4(1-\nu_s^2)}\right] \left[\frac{1}{K_d^i} - \frac{1}{K_d^\infty}\right] \frac{a}{\hat{a}} \exp(-\frac{a}{\hat{a}}) \tag{15}$$

Consequently, the crack porosity can be calculated by the following formula (Jaeger et al., 2007):

$$\phi_{crack} = \int_0^\infty C(a)da = \left(\frac{1}{K_d^i} - \frac{1}{K_d^\infty}\right) \hat{P} \tag{16}$$

The correlation between porosity and permeability requires that a detailed description of pore geometry at micro scale is given.The following section describes a new permeability model which relates the permeability of porous medium to its microstructure through evolution of bulk modulus.

3 Permeability modeling

The permeability of the rock is a macroscopic concept defined at a Representative Elementary Volume (REV). The mathematical description of permeability requires that microstructure of the porosity to be well-defined. According to Scheidegger (1974), Guéguen and Dienes (1989) the porosity and permeability could be correlated if the microstructure of the porosity is described by a set of statistical distribution functions that describe pore geometry and pore size distribution. The pore geometry can be divided roughly into two categories: equant pores and cracks. Albeit, there is no clear division between these two categories. The low aspect ratio pores at grained contacts can be viewed as crack porosity and the high aspect ratio pores may represent the equant pores. In granular materials such as sandstone, both equant pores and cracks coexist.

Bernabe (1986) assumed that permeability k is a single valued function of P_c and P_p. It was assumed that the knowledge of permeability as a function of confining pressure and zero pore pressure is enough to predict the value of permeability at any pair of (P_c, P_p) and effective pressure P_{eff} was defined as confining pressure that would result in the same permeability $k(P_{eff}) = k(P_c, 0)$. If the effective pressure defined as a linear combination of P_c and P_p, the $k(P_c, P_p)$ would be a family of curves that can be approximated by parallel straight lines. Bernabe (1986) suggested a differential form of the permeability evolution:

$$dk = \left(\frac{\partial k}{\partial P_c}\right)_{P_p} dP_c + \left(\frac{\partial k}{\partial P_p}\right)_{P_c} dP_p \tag{17}$$

Here, the permeability would be approximated as a function of Terzaghi effective pressure:

$$k(P') = k(P^\infty) - \int_{P'}^{P^\infty} \left(\frac{\partial k}{\partial P'}\right)_T dP' = k^\infty - \int_{P'}^{\infty} \left(\frac{\partial k}{\partial \phi}\right)\left(\frac{\partial \phi}{\partial P'}\right) dP' \tag{18}$$

where k^∞ is intact rock permeability where all the cracks are closed and subscript T represents a constant temperature. The porosity dependence of permeability can be derived by employing Kozeny-Carman equation (Eq.5):

$$\frac{dk}{d\phi} = c_1 d^2 (3e^2 + 2e^3) \tag{19}$$

where e is the void ratio defined as $e = \frac{\phi}{1-\phi}$. It is assumed that porosity dependence of permeability $\frac{dk}{d\phi}$ is governed by equant pores and is independent of pressure, therefore can be taken out of the integral. The assumption that pressure dependence of porosity is governed by cracks requires that $\frac{\partial \phi}{\partial P'}$ is given by Eq.7 where the tangent drained bulk modulus can be estimated by Eq.13:

$$\begin{aligned} k(P') &= k^\infty - \int_{P'}^{\infty} \left(\frac{\partial k}{\partial \phi}\right)\left(\frac{\partial \phi}{\partial P'}\right) dP' \\ &= k^\infty - C_{kc} d^2 (3e^2 + 2e^3) \\ &\quad \int_{P'}^{\infty} \left\{ (1-\phi_0) \left[\frac{1}{K_d^\infty} + \left(\frac{1}{K_d^i} - \frac{1}{K_d^\infty} \right) \exp\left(-\frac{P'}{\hat{P}} \right) \right] - \frac{1}{K_s} \right\} dP' \end{aligned} \tag{20}$$

the integral could be divided into two parts:

$$\begin{aligned}&\int_{P'}^{\infty}\left(\frac{1-\phi_0}{K_d^{\infty}}-\frac{1}{K_s}\right)dP'\\&+\int_{P'}^{\infty}\left\{(1-\phi_0)\left(\frac{1}{K_d^{i}}-\frac{1}{K_d^{\infty}}\right)\exp\left(-\frac{P'}{\hat{P}}\right)\right\}dP'\end{aligned} \tag{21}$$

The upper bound of the drained bulk modulus is given by Berryman (1992) to be $(1-\phi_0)K_s$, hence the first integral is equal to $-P'\left(\frac{1-\phi_0}{K_d^{\infty}}-\frac{1}{K_s}\right)$. The second integral contains an exponential term $\exp(-\frac{P'}{\hat{P}})$ where its closed form would be written as $\left[-\hat{P}\exp(-\frac{P'}{\hat{P}})\right]_{P'}^{\infty}$ which is equal to $\hat{P}\exp(-\frac{P'}{\hat{P}})$. Consequently, the permeability evolution could be fitted into a function of the following form:

$$k=k^*-A(3e^2+2e^3)\left(\frac{1-\phi_0}{K_d}-\frac{1}{K_s}\right) \tag{22}$$

with

$$\begin{aligned}&k^*=k^{\infty}+c_1d^2(3e^2+2e^3)(\hat{P}+P')\left[\frac{(1-\phi_0)}{K_d^{\infty}}-\frac{1}{K_s}\right]\\&A=C_{kc}d^2\hat{P}\end{aligned} \tag{23}$$

where k^* is preserved permeability, where part of the cracks at confined state are still open. The parameter A has the same dimension as force and can be assigned to a tension force between fluid and solid. Eq.22 states that permeability is a function of effective pressure, porosity variation ($\frac{d\phi}{dP'}$), void ratio and characteristic length.

4 Material and methods

In order to describe the fluid flow in a poroelastic medium, it is essential to provide the relationships between microstructure of the porosity and strain, and between strain and permeability. The permeability model developed in section 3 represents the pore volume as a combination of spherical pores and cracks. The spherical pores are connected by penny-shaped cracks and the inter-connectivity between them is controlled by elastic closure of cracks. The crack closure mainly influences in fluid pathways (tortuosity), and consequently permeability. While the crack closure theory provide the relation between microstructure of porosity (aspect ratio distribution) and strain, the poroelasticity theory characterizes the relation between strain and applied effective pressure.

In the following, first the hydrostatic tests carried out will be explained where the stress-strain curves not only characterize the bulk behavior of the rock, but also provide valuable information about the microstructure of porosity.

4.1 Sample material and setup

The experiments were carried out on two cylindrical core samples of Flechtinger sandstone (FLG05 and FLG06), having 50 mm diameter and 100 mm length. It is a Lower Permian (Rotliegend) sedimentary rock in the North German Basin. Flechtinger sandstone is a fine layered sandstone mostly composed of quartz, feldspar and carbonates. A convectional triaxial test system was employed to perform the experiments (Fig.1). The set up is composed of a confining pressure intensifier to fill and pressurize the

triaxial cell up to 140 MPa, a set of Quizix pumps which are operating independently and can increase the pore fluid pressure up to 70 MPa, and a data monitoring and acquisition system. The circumferential and axial extensometers measured the lateral and axial strains. The confining pressure was measured by fluid pressure transducers in triaxial. The pore fluid pressure was measured by pressure transducers in drained experiments and by a differential pressure transducer in permeability tests.

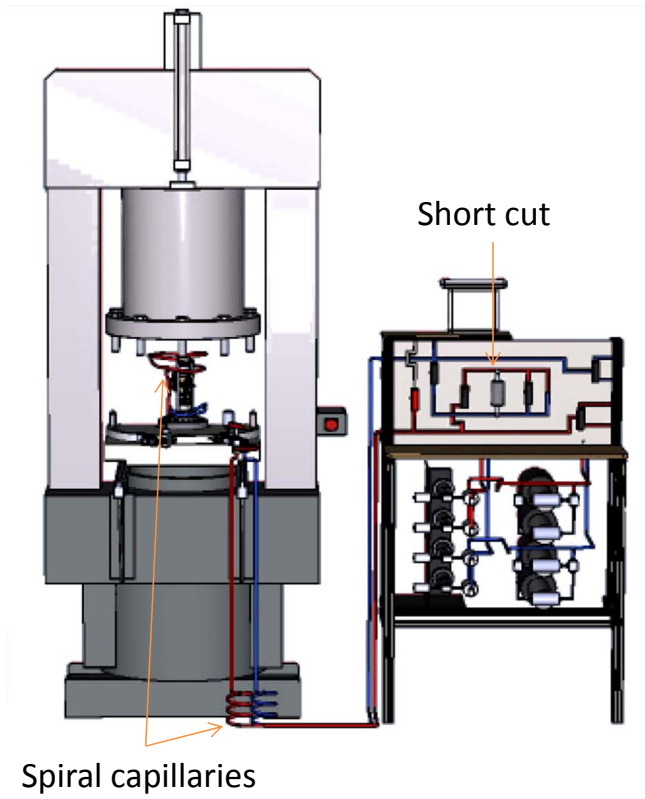

Figure 1: experimental set up: a conventional triaxial cell.

4.2 Experimental procedure, analysis and corrections

The pressure drop was measured at a steady state condition and a constant flow rate of 0.02 ml/min was applied. An extra differential pressure transducer was installed to measure the pressure difference between upstream and downstream through a bypass connection where the frictional pressure drop in capillaries was reduced (see Figure 1).

First, the initial porosity of the samples were determined by imbibition and Archimedes methods. The samples were dried in the 60 °C for 24 hours. Afterwards, the samples were saturated by first applying vacuum to the samples, which were placed in a desiccator and then by drawing water into desiccator where the water imbibes into the porous rock. The initial porosity was calculated by measuring dry weight (W_d), the saturated weight in air (W_s), and the suspended (Archimedes) weight in water (W_a) to

be $\phi^i = (W_s - W_d)/(W_s - W_a)$. Then the sample was mounted in the triaxial cell and the whole system was vacuumized. The vacuumized pressure in the whole set up was monitored to be sure that all the fittings and capillaries are well isolated and there is no leakage. Afterwards, the sample was saturated by flowing water through it for at least 72 hours. The samples were subjected to a cyclic seasonings (preconditioning) to minimize hysteresis and inelastic effects. The preconditioning was composed of four pressure cycles between 0 to 60 MPa with a rate of 1 MPa/min. Two different kind of experiments were carried out on the given specimens (Table 1), a hydrostatic drained test (FLG05, where FLG stands for Flechtinger sandstone) and a permeability measurement test (FLG06). The confining pressure was cycled from 2 to 55 MPa and temperature was increased step-wise from 30 °C to 140 °C. The range of experimental pressure and temperature were chosen such that representing changes due to injection of water into a geothermal reservoir in North German Basin (Hassanzadegan et al., 2011). During the injection of cold water into a doublet geothermal reservoir, effective pressure and temperature are chaining. The cold water of 60 °C will be injected into a 145 °C reservoir and the cold thermal front will propagate through the reservoir towards the production well. The effective pressure becomes more compressive in the vicinity of production well due to a decrease in pore pressure and becomes more tensile around the injection well due to an increase in pore pressure. The pore pressure and downstream pressure were held at a constant pressure of 1 MPa at drained and permeability tests, respectively.

Table 1: Specimen characteristics and achieved experiments

	Experiment	Porosity	Grain density
Specimen	Type	[%]	[gr/cm^3]
FLG05	drained	10.75	2.66
FLG06	permeability	10.68	2.64

Data was recorded every 15 seconds which corresponds to 25 kPa increase in confining pressure. The same sampling rate (four per minute) was employed for the pump system. In order to minimize the effect of small fluctuations of the recorded data two approaches are common [27]: fitting data to a mathematical function or averaging the data. The data was first smoothed by averaging every 15 raw data and subsequently, the tangent derivatives of stress-strain curve (tangent drained bulk modulus) was calculated ($K_d = \frac{\partial P_c}{\partial \varepsilon_b}$) and were fitted to the functions of the form presented of Eq.13. The data analysing was aimed at determining the pressure dependence of porosity and permeability and relating them through the poroelastic and crack closure theories. First and second derivative of stress-strain curves were obtained, and the porosity and permeability were calculated.

The capillary (drainage) system was modified to minimize the thermal effects on stainless capillary tubes. A part of capillary tubes sits inside the triaxial cell and the other part connects the triaxial cell to the pumps. Three thermocouples were employed, two were placed close to the upper and lower part of the sample within the triaxial cell and one thermocouple was placed outside the triaxial cell to measure the atmospheric temperature. Inside the cell, a uniform temperature distribution was a reasonable assumption. The temperature measurement uncertainty was determined by relative error, the ratio between standard deviation $\sigma(T)$ and the average measured temperature $\overline{T}$ (see Table 2). The injected fluid was brought to the sample temperature by placing a longer spiral shape capillary within the chamber. However, a temperature distribution was established at capillary tubes outside, as the triaxial cell temperature and surrounding temperature stayed constant. In order to minimize this temperature distribution effect, the heat transfer surface area was extended by employing fins and a spring shaped tube (see Figure 1).

Table 2: The uncertainty in temperature measurement was characterized by relative error [%], the ratio between standard deviation $\sigma(T)$ and the average measured temperature $\overline{T}$.

Temperature	Loading			Unloading		
[°C]	$\overline{T}$	$\sigma(T)$	[%]	$\overline{T}$	$\sigma(T)$	[%]
30	31.5	0.3	1.0	30.7	0.2	0.8
60	59.5	0.1	0.2	58.8	0.1	0.2
90	89.7	0.2	0.2	89.0	0.2	0.2
120	120.0	0.4	0.3	119.3	0.3	0.2
140	139.4	0.9	0.7	139.4	0.3	0.2

5 Experimental results

A drained jacketed test and a permeability measurement test (see Table 1) were performed. The porosity change was calculated by utilizing poroelastic theory and permeability was calculated by employing Darcy's law.

5.1 Porosity change

The porosity change was calculated by employing Eq.7. The tangent derivative of stress-strain curve was providing the tangent bulk modulus. The stress-strain curves were measured while performing jacketed test and permeability test. The stress-strain curves while flowing water through the sample (Figure 2) showed that Flechtinger sandstone suffered from inelastic deformation. That is, the stress-strain curves showed non recoverable strain after each pressure cycle. The maximum inelastic strain was observant at °C. Table 3 summarize the inelastic strains and quantifies the consequent porosity reduction. It was assumed that inelastic bulk strain ε_b^{in} and pore strain are equal and the initial porosity was corrected for inelastic deformation in both samples ($V_p = V_p^i - \varepsilon_b^{in} \times V_p^i$). V_p^i is the initial pore volume at the beginning of each cycle.

The porosity change, calculated at drained conditions was compared with porosity change while flowing water through the sample. Both specimens showed a compatible porosity evolution (Fig. 3). Therefore, porosity change was evaluated by employing tangent drained bulk (first derivative of stress-strain curve) while flowing water through the rock and using stress-strain curves plotted in Figure 2. The porosity of Flechtinger sandstone decreases with increasing effective pressure and after each pressure cycle (Table 3). The rate of porosity change with pressure was as low as 0.055 [%]/[MPa].

Table 3: The inelastic deformation of Flechtinger sandstone.

Temperature [°C]	Bulk inelastic strain [-]$\times 10^{-4}$	Porosity reduction [-]$\times 10^{-4}$	Porosity [%]
30	1.8	1.6	10.68
60	19	17	10.66
90	8.0	7.2	10.50
120	9.3	8.4	10.42
140	3.8	3.4	10.33

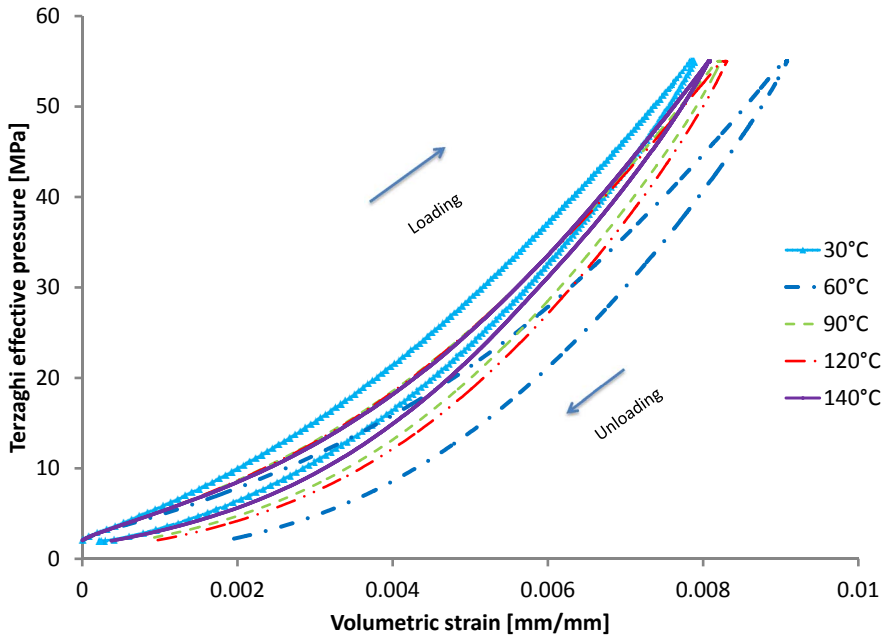

Figure 2: Terzaghi effective pressure versus volumetric strain. The downstream pore pressure was maintained constant at a value of 1 MPa and confining pressure was cycled.

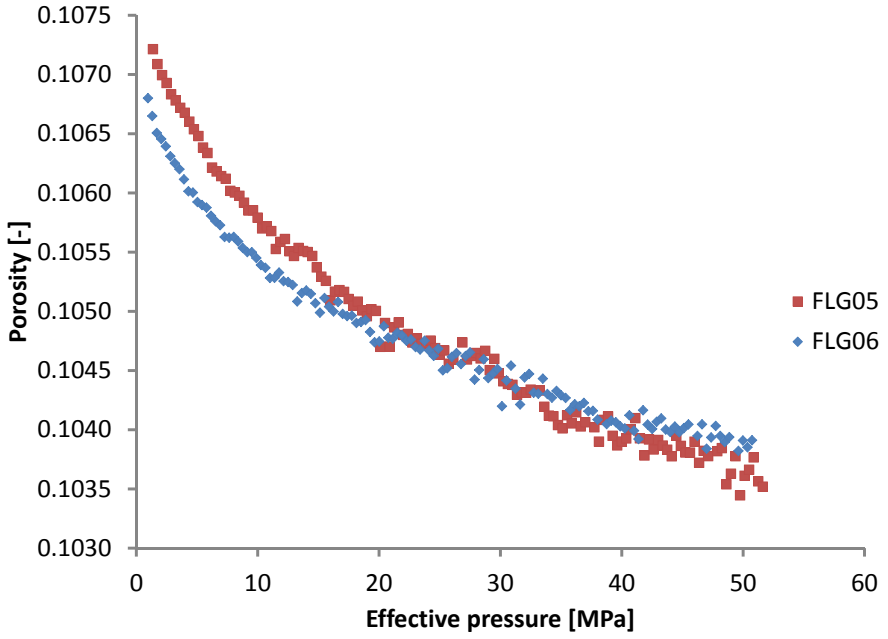

Figure 3: Porosity evolution as a function of effective pressure at drained and flowing conditions.

5.2 Bulk modulus and crack porosity

The deformation of the specimen (FLG06) while performing the permeability test was captured by one axial and two lateral extensometers. The derivatives of stress-strain curve ($K_d = \frac{\partial P_c}{\partial \varepsilon_b}$) was calculated by numerical differentiation of neighboring data points and plotted as a function of mean effective pressure, the difference between confining pressure and average pore pressure within the sample. The strain measurement accuracy meets the requirement for calibration according to ISO 9513 class 0.5, where the strain measurement accuracy is ± 0.5% of reading or ± 1μm of the indicated value, whichever is larger. The pressure measurement was quite precise with 0.001 MPa deviation. The error involved in calculating drained bulk modulus was estimated by Eq.24 to be approximately 30 MPa.

$$\left(\frac{\Delta K_d}{K_d}\right)^2 = \left(\frac{\Delta P}{P}\right)^2 + \left(\frac{\Delta \varepsilon_b}{\varepsilon_b}\right)^2 \tag{24}$$

Having calculated the uncertainty in measurements of the bulk modulus, the porosity-measurement error can be defined by the total derivative of the Eq.7 or Eq.16:

$$\left(\frac{\Delta \phi}{\phi}\right)^2 = \left(\frac{\Delta K_d}{K_d}\right)^2 + \left(\frac{\Delta P}{P}\right)^2 \tag{25}$$

The error in porosity measurement was estimated to be 3×10^{-4} (Eq.25). Afterwards, the data was fitted to the functions of the form suggested by Zimmerman (1991) and model parameters were derived by the least squares method where the overall solution minimizes the sum of the squares of the errors made at each data point. Figure 4 shows that the modeled bulk modulus adequately estimates the experimental data. A crossplot of Figure 4 was obtained (for all temperatures) by cutting the best fitting surface which was interpolated through data points, at different pressure levels. Figure 5 presents the evolution of bulk modulus due to temperature and the applied cyclic load. The bulk modulus slightly decreased with increasing temperature at low pressures and lightly increased with temperature at high pressures.

The solid matrix parameters, solid bulk modulus and Poisson's ratio of the Flechtinger sandstone, were calculated by the Voigt-Reuss-Hill average to be 41.2 GPa and 0.131, respectively (Hassanzadegan et al., 2012). The table 4 summarizes the loading bulk modulus parameters and crack porosity at different loading paths and temperatures. A 50% increase in crack porosity was occurred at 60 °C. The characteristic closure pressure decreased after 60 °C pressure cycle. The value of the relaxed bulk modulus parameter K_d^i decreased after each pressure cycle and with increasing temperature, however the confined bulk modulus parameter was fluctuating. The table 5 summarizes the unloading bulk modulus parameters and crack porosity. The value of K_d^∞ increased after each pressure cycle and with increasing temperature (except at 140 °C). The loading and unloading values of K_d^∞ were in the same range. The unloading parameters ϕ_c, $\hat{P}$ and K_d^i were smaller than those of loading path. Moreover, table 5 presents the average value of measured temperature and its standard deviation.

Table 4: Loading bulk modulus parameters at given temperatures.

Temperature	K_d^∞	K_d^i	$\hat{P}$	ϕ_{crack}
[°C]	[GPa]	[GPa]	[MPa]	[-]
30	10.51	3.05	13.49	0.0031
60	10.73	2.24	13.01	0.0046
90	10.25	2.37	11.44	0.0037
120	9.84	2.32	9.95	0.0033
140	10.68	2.18	10.64	0.0039

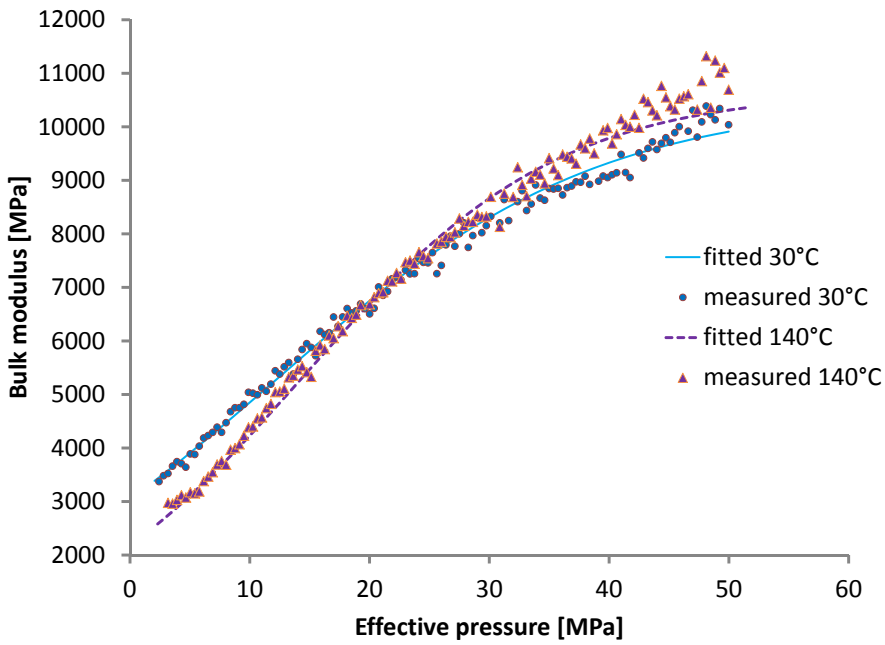

Figure 4: Loading bulk modulus as a function of effective pressure at 30 and 140 °C. The experimental data and modeled bulk modulus (Eq.13) fit adequately.

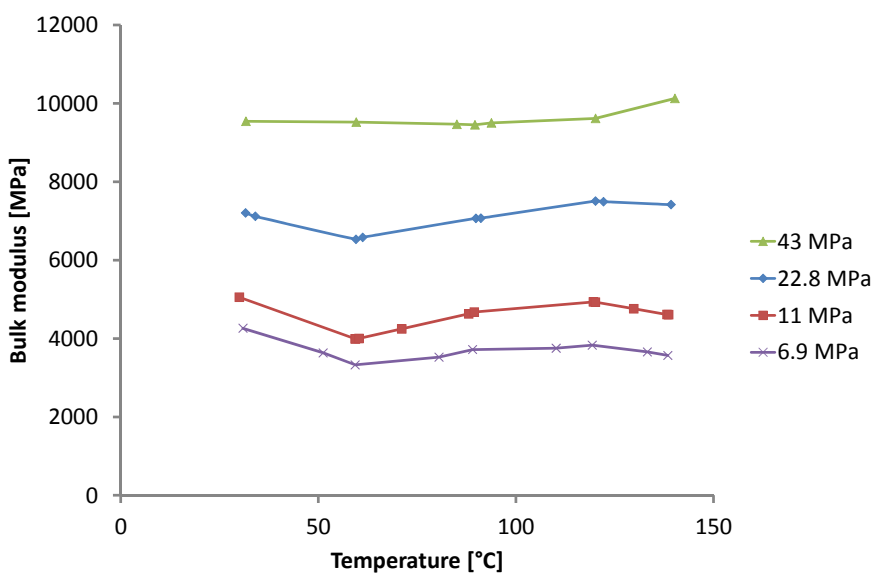

Figure 5: Bulk modulus as a function of temperature. A crossplot of Figure 4 for all temperatures shows the evolution of bulk modulus due to temperature and the applied cyclic load at different pressure levels. The new data points were obtained by interpolation.

Table 5: Unloading bulk modulus parameters at given temperatures.

Temperature	K_d^∞	K_d^i	$\hat{P}$	ϕ_{crack}
[°C]	[GPa]	[GPa]	[MPa]	[-]
30	10.06	1.98	6.68	0.0027
60	10.56	2.23	7.85	0.0028
90	10.94	1.99	7.63	0.0031
120	10.97	1.95	7.41	0.0031
140	10.90	1.91	7.43	0.0032

Figure 6 compares the spectrums of the crack porosity function at loading and unloading paths. The Morlier's method was employed to determine the crack porosity function. At unloading path the maximum of $C(a)$ was shifted towards the smaller values of the aspect ratio. The maximum value at unloading spectrum was approximately two times of the loading one.

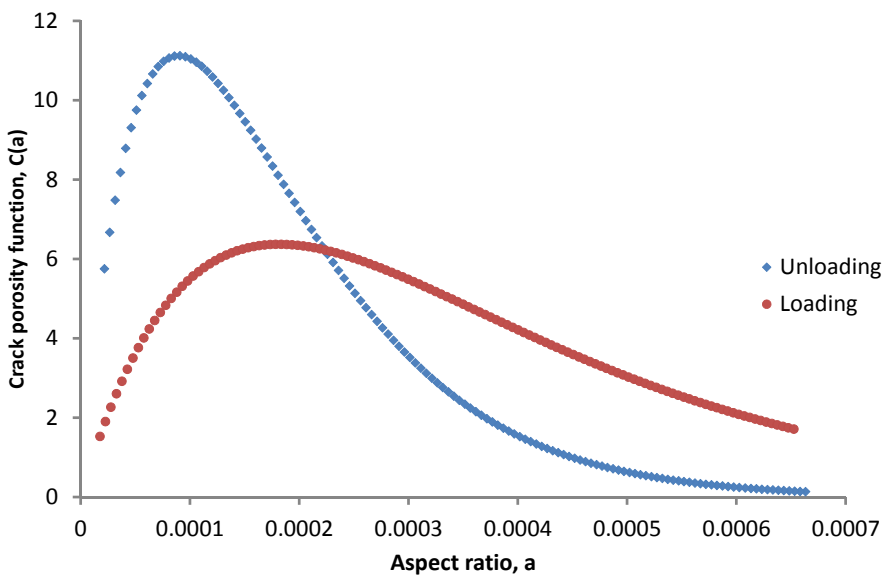

Figure 6: The loading and unloading crack porosity function of Flechtinger sandstone, as computed by Morlier's method at 30°C.

Figure 7 shows loading spectrum of aspect ratio at different temperatures. At loading path, the maximum value of $C(a)$ was increased with increasing the temperature, except from the 60°C spectrum. Figure 8 displays the unloading spectrum of aspect ratio at given temperatures. The maximum value of function $C(a)$ was shifted towards smaller value of a in comparison to loading path and the maximum value of $C(a)$ function increased with increasing the temperature except from the 60 °C spectrum.

5.3 Permeability

Permeability was measured at a constant flow rate of 0.02 ml/min and downstream pore pressure was kept constant at 1 MPa. The permeability was calculated by reading the pressure drop across the pressure

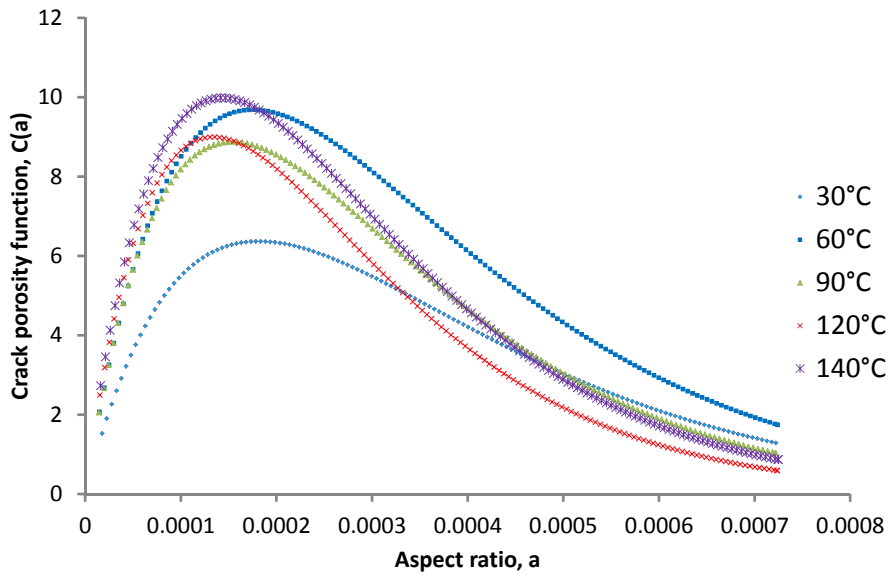

Figure 7: The loading crack porosity function of Flechtinger sandstone at different temperatures.

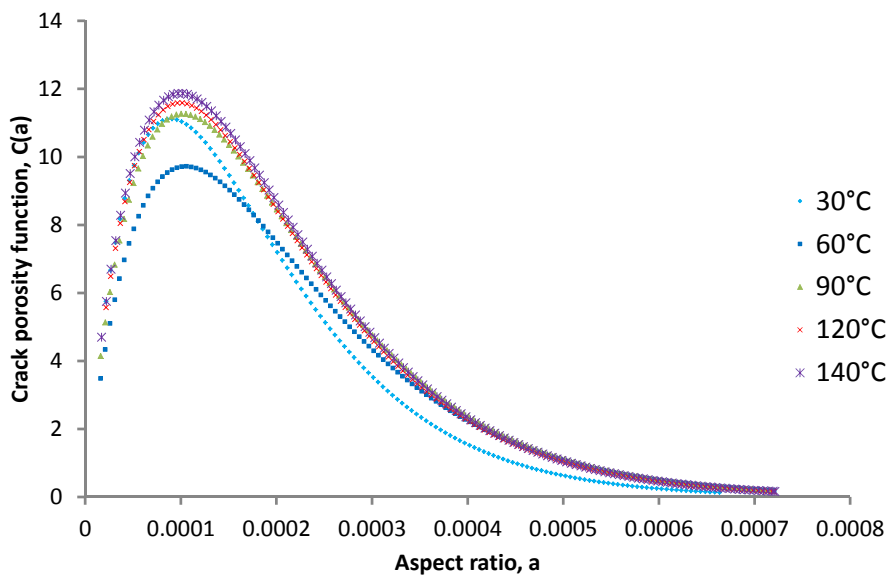

Figure 8: The unloading crack porosity function of Flechtinger sandstone at different temperatures.

transducer and employing Darcy's law (Eq.1). The permeability values are compatible with those reported by Blöcher et al. (2009). The relative precision error of permeability measurement, the ratio between standard deviation and average value, was calculated at a constant effective pressure, flow rate and temperature. The standard deviation, average value and relative error were calculated to be 9.5×10^{-5}, 0.0253 and 0.38 %, respectively. The viscosity of water was corrected for temperature at 1 MPa.

Figure 9 presents the loading permeability evolution as a function of mean effective pressure, the difference between confining pressure and average pore pressure within the sample. Figure 9 shows a good match between measured and the estimated permeability (Eq.22). Permeability was decreasing with increasing effective pressure. The loading permeability decreased with increasing temperature and after first and second pressure cycles (30 and 60 °C) and slightly increased with increasing temperature and after (90 and 120 °C) pressure cycles. The rate of permeability change was high at relaxed state and permeability linearly decreased with increasing pressure at confined state or was approximately constant. The experimental permeability data were fitted to proposed model (section 3) and the validity of the model was confirmed by predicting appropriately the permeability evolution.

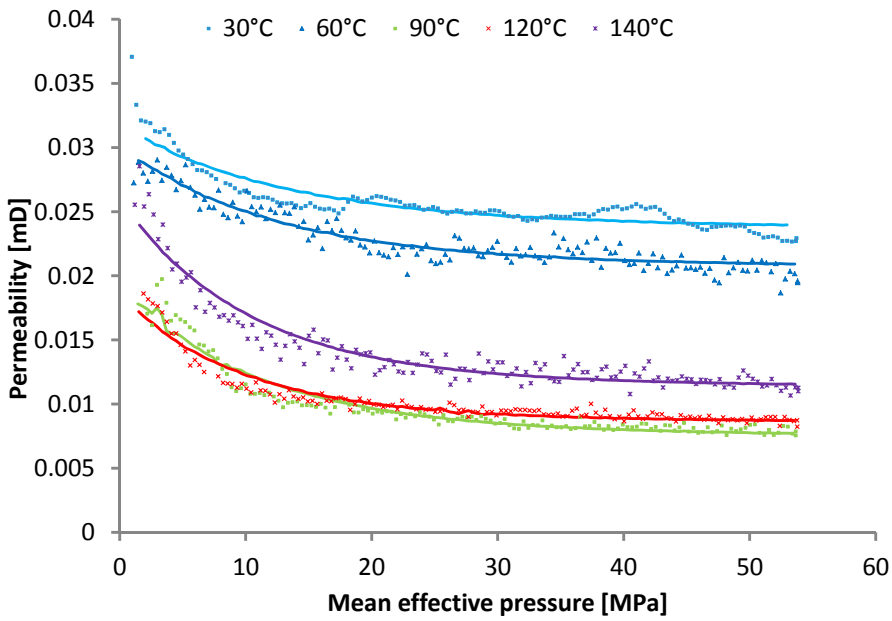

Figure 9: The loading permeability as a function of effective pressure and temperature. The solid lines show the matched permeability and scattered data points are experimental data.

Figure 10 shows the unloading permeability evolution. The unloading permeability at 30 °C is partly presented due to the noise in the data. The unloading permeability was lower than loading permeability and was nonlinear at relaxed state, effective pressures lower than characteristic pressure, and was linear or approximately constant at confined state. The unloading permeability slightly increased with increasing temperature and after 30 °C pressure cycle and enormously decreased after 60 °C pressure cycle. The unloading permeability increased with increasing temperature and after 90 and 120 °C pressure cycles. A crossplot of Figure 9 was obtained by cutting the best fitting surface at different pressure levels (Figure 11). The permeability decreased significantly up to 90 °C and slightly increased afterwards.

The force parameter A and preserved permeability K^* were obtained as best-fitting parameters of Eq.23. The values of force parameter A presented in Table 6 are the absolute values. They were negative at loading path and positive at unloading path. The minimum values of loading-unloading force parameters

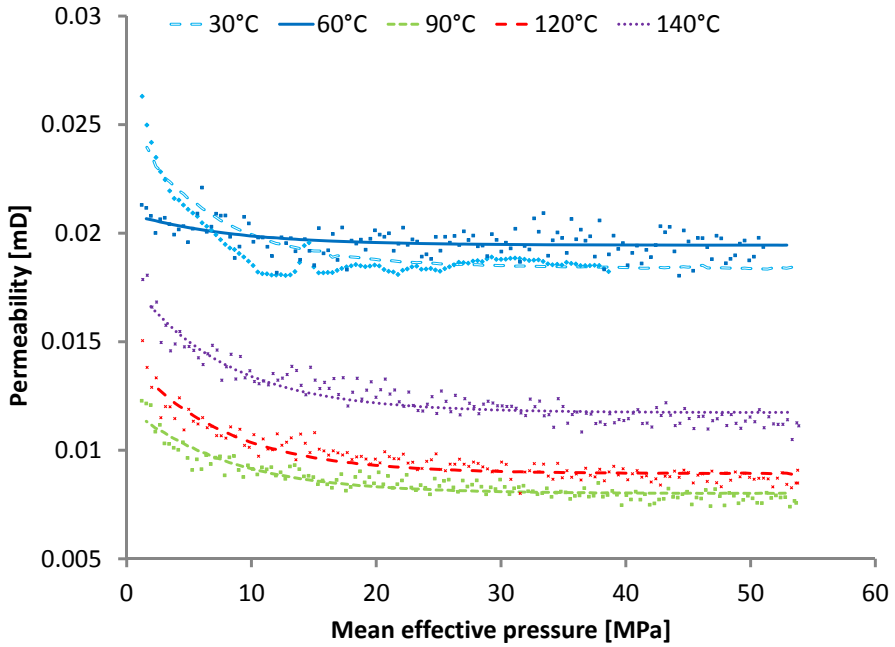

Figure 10: The unloading permeability as a function of effective pressure and temperature. The solid lines show the matched permeability and scattered data points are experimental data.

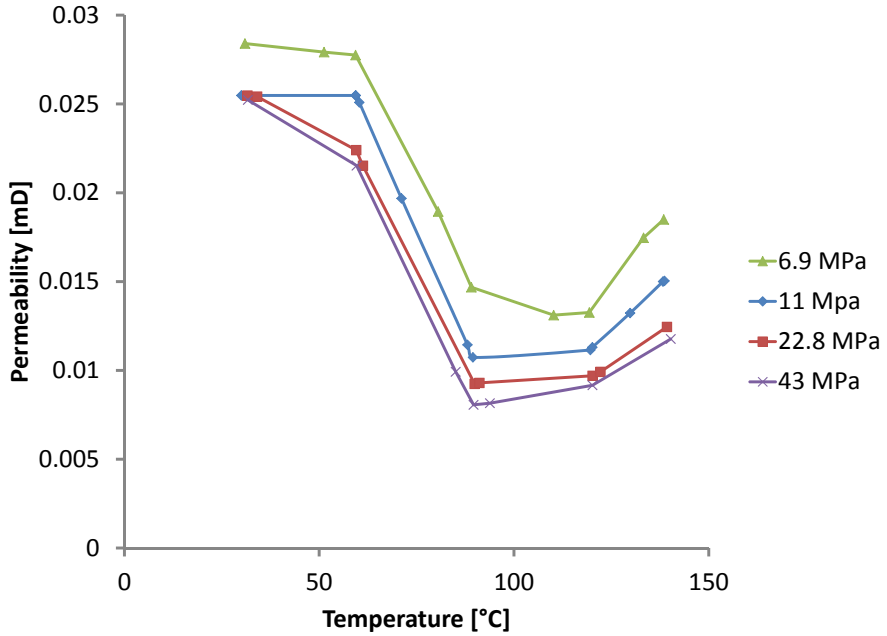

Figure 11: Permeability as a function of temperature at loading path. A crossplot of Figure 9 presents the permeability evolution. The new data points were obtained by interpolation.

were observed at 60 °C.

Table 6: The permeability fitting parameters and characteristic length

Temperature	loading			unloading		
[°C]	K^*[mD]	A[N]	d[μm]	K^*[mD]	A[N]	d[μm]
30	0.0203	2.07	110	0.0167	1.03	110
60	0.0178	1.84	105	0.0189	0.29	55
90	0.0038	2.53	130	0.0068	0.72	90
120	0.0054	2.13	130	0.0074	0.83	95
140	0.0074	2.88	150	0.0100	1.06	110

Having determined the force parameter A, the characteristic length d can be calculated, using Eq.23. It was assumed that $c_1 = \frac{1000}{180} \times \frac{9}{4} = 12.5$ (Bear, 1988). For all pressure cycles, the calculated unloading characteristic lengths were lower or equal to the loading characteristic lengths (see Table 6).

6 Interpretation and discussion

Three types of stress-permeability relations have been distinguished by David et al. (1994) and the mechanisms involved have been described: 1-low porosity crystalline rocks where the cracks are dominant, 2-porous clastic rocks where the relative movement of grains result in a decrease of permeability, and 3-grain crushing in unconsolidated material at high pressures.

The effects of applied pressure on the permeability depends on the pore geometry and the degree of connectivity between pores. The effect of pressure is not the same for all pore geometries, the flat pores close easily when the pressure is applied, however the equant pores (high aspect ratio pores) are stiffer. While the crack porosity had a little contribution in total porosity of Flechtinger sandstone, but the cracks provided the interconnections between pores and fluid pathways. According to Guéguen and Palciauskas (1994) the closure of the cracks depends on the elastic processes up to a certain value of pressure, after which the crack roughness and stiffness of equant pores preserve the permeability. In contrast, the crack volume is relatively a small part of the total porosity and the total porosity is governed by other than that caused by narrow cracks (Walsh, 1980).

Guéguen and Dienes (1989) presented two simple models, using 1D and 2D objects, pipes and cracks, respectively. The pore micro-structure was determined by statistical distribution of three parameters: average pipe (crack) length, average pipe radius (crack aperture) and average pipe (crack) spacing.

The introduced model relates the microstructure of porosity, strain and permeability through the key concept of effective pressure. The common approach to model pressure-dependence of the rock bulk modulus is to introduce a crack aspect ratio distribution of penny-shaped cracks (Walsh, 1980). The Flechtinger sandstone was assumed to be embedded by equant pores and penny-shaped cracks in a solid phase. The spherical pores (equant pores) are the stiffest type of the pores and could be assumed non-closable under typical elastic stress. The new model predicts the permeability evolution from a relaxed state, where the low aspect ratio cracks are open, to a confined state, where the cracks gradually close. The presented model introduce a characteristic closure pressure at which a transition from relaxed state to a confined state will occur. At relaxed state, pressures lower than characteristic closure pressure, the rock is more compliant and becomes stiffer with increasing effective pressure (confined state).

The presented model describe the nonlinear behavior of stress-strain curve by crack closure, however does not include the other nonlinearities such as Skempton effect (increase in pore pressure due to the applied confining pressure). Moreover, the presented model assumes a quasi-static deformation and does

not include the transient response, where the pore pressure diffusion is coupled with change in mass content.

The presented permeability model is compatible with percolation concept where the occupancy probability p is proportional to the crack porosity ϕ_c and inversely proportional to the aspect ratio a (Guéguen and Palciauskas, 1994). The Eq.15 presents a differential form of the occupancy probability. Both permeability and bulk modulus were assumed to be proportional to the cumulative population of open cracks which their probability density function can be derived by normalizing Eq.15. A relaxed bulk modulus, a confined bulk modulus and a characteristic closure pressure (aspect ratio) are the key parameters that characterize the bulk modulus and permeability model. At relaxed state where the most cracks are open the probability to have a connected network is high and by increasing the pressure the probability of having a connected fluid path decreases.

The exponential bulk modulus functions were fitted to experimentally measured tangent drained bulk modulus (Fig.4). At low effective pressures, both cracks (low aspect ratio pores) and equant dimension pores affect the elastic moduli and the rock exhibit compliant behavior, where the pressure dependence of bulk modulus is large. However, by increasing the confining pressure the cracks close and the spherical pores do not. The quality of the match is convenient for low and middle pressures, however at higher pressure (more than 45 MPa) and higher temperatures, a deviation can be observed. At high pressures and temperatures, the rock is stiffer than predicted which can be assigned to inelastic behavior of the Flechtinger sandstone. The inelastic behavior of the rock was observed to be higher during 60 °C pressure cycle (see Table 3).

Figure 6 shows that the maximum value of crack porosity function is moving towards the higher aspect ratio at loading path. Accordingly, the loading characteristic closure pressure is higher than unloading characteristic closure pressure. That is, a higher effective pressure at loading path is required in comparison to unloading path to close the high density cracks (the cracks with a certain aspect ratio which have the highest population). It confirms that the unloading moduli can be approximated to be elastic moduli at the initial part of unloading path where the most of the cracks are closed.

The range of aspect ratio values is compatible with those derived for Boise, Berea and Bandera sandstones Zimmerman (1991). The small value of aspect ratios can be explained by the fact that crack closure theory does not consider the interaction between cracks. Moreover, as presented in Eq.8, the crack radius appears in third power. That is, a few long cracks may strongly affect the rock behavior. David and Zimmerman (2012) reported an order of magnitudes higher aspect ratios for Vosgas and Fontainbleau sandstone, albeit the samples were subjected to a high confining pressure of 280 MPa.

The discrepancy in spectrums at loading and unloading paths, could explain the hysteresis in permeability evolution as observed here and by Bernabe (1986, 1987). The number of cracks which are open to fluid flow at loading and unloading paths at a same pressure is different. At unloading path, more cracks are open at relaxed state while at loading path the number of cracks which are open at low or middle range pressure is higher. Furthermore, the calculated unloading characteristic lengths were lower or equal to the loading characteristic lengths. That is, the pore dimension is lower at unloading path compare to loading path. The total crack porosity at loading path is higher than unloading path (see Tables 4 and 5). Furthermore, the unloading spectrum of crack porosity function follows a special trend with respect to temperature and the maximum value of crack porosity function increases with temperature (Fig.8). The crack porosity increases with temperature and after each pressure cycle, however the crack porosity change is close to the calculated uncertainty (see Table 5).

Creation of new cracks due to applied thermal and mechanical loads and inelastic behavior of rock may explain the changes in crack porosity and observed permeability evolution. Figure 11 shows that loading permeability decreases with increasing temperature initially (after first two pressure cycles), however, the permeability slightly increases with temperature afterwards. A decrease of permeability can be assigned to inelastic deformation and an increase in permeability can be attributed to creation of new cracks. That is, permanent closure of some cracks lower the degree of inter-connectivity between pores and affects on

how easily fluid flows within the rock. For example, the permeability decreased considerably after 60 °C pressure cycle where the highest amount of inelastic strain was observed (see Table 3). Creation of new cracks due to applied thermo-mechanical load may produce new pathways and can increase the degree of inter-connectivity between pores (see Table 5).

7 Conclusion

A new permeability model was derived from the basic principles underlying the theories of poroelasticity and crack closure. The strain was related to microstructure of porosity and permeability was related to strain. The first and second derivative of stress-strain curves were employed to connect permeability and microstructure of porosity. The permeability model also provided the average characteristic length of the porous media. The calculated unloading characteristic lengths were lower or equal to the loading characteristic lengths. The loading and unloading aspect ratio distribution described the hysteresis in permeability during loading and unloading paths. The loading permeability decreased with increasing temperature and after each pressure cycle.

Measurements of the mechanical behavior of the Flechtinger sandstone showed that stress-strain curves were nonlinear and not all the strains were recovered after unloading. The pressure dependence of the bulk modulus and nonlinearity in stress-strain curves was assigned to presence of cracks. The permeability was governed by cracks where the cracks not only provide pathways to fluid flow but also guaranty the inter-connection between pores.

The permeability decreased with increasing effective pressure and after each pressure cycle. It was nonlinear at relaxed state (low effective pressures) and linear at confined state (high effective pressures). In contrast, the unloading crack porosity was slightly increased. It can be concluded that a competition between Thermo-mechanical crack creation, and inelastic deformation of the rock governs the permeability evolution under cyclic loading.

References

Akazawa, T. (2004). A technique for automatic detection of onset time of pand s-phases in strong motion records, 13th world conference on earthquake engineering vancouver, b.c., Canada. In *13th World Conference on Earthquake Engineering*, pages 1–9.

Anderson, D. (1989). *Theory of the Earth*. Blackwell.

Anderson, E. (1951). *The dynamics of faulting and dyke formation with applications to Britain*. Hafner Pub. Co.

Angevine, C. L. and Turcotte, D. L. (1983). Porosity reduction by pressure solution: A theoretical model for quartz arenites. *Geological Society of America Bulletin*, 94(10):1129–1134.

Araujo, R., Sousa, J., and Bloch, M. (1997). Experimental investigation on the influence of temperature on the mechanical properties of reservoir rocks. *Int. J. Rock Mech. Min. Sci.*, 34:1 –16.

Bandura, A. (2012). *Geomechanical simulation of CO2 injection*, chapter 5, Geomechanical simulation of CO2 injection. Springer.

Barton, C., Zoback, M., and Moos, D. (1995). Fluid flow along potentially active faults in crystalline rock. *Geology*, 23(8):683–686.

Bear, J. (1988). *Dynamics of Fluids in Porous Media*. Dover Books on Physics and Chemistry. Dover.

Bernabe, Y. (1986). The effective pressure law for permeability in chelmsford granite and barre granite. *Int. J. Rock Mech. Min. Sci.*, 23(3):267–275.

Bernabe, Y. (1987). The effective pressure law for permeability during pore pressure and confining pressure cycling of several crystalline rocks. *J. Geophys. Res.*, 92:649–657.

Berryman, J. G. (1992). Effective stress for transport properties of inhomogeneous porous rock. *J. Geophys. Res*, 97:17409–17424.

Berryman, J. G. (1995). Mixture theories for rock properties. *American Geophysical Union Handbook of Physical Constants, edited by T. J. Ahrens*, AGU, New York:205–228.

Biot, M. A. (1941). General theory of three-dimensional consolidation. *J. Appl. Phys.*, 12(2):155–164.

Biot, M. A. (1956). Theory of propagation of elastic waves in a fluid-saturated porous solid. i. low-frequency range. *J. Acoust. Soc. Am.*, 28(2):168–178.

Biot, M. A. (1973). Nonlinear and semilinear rheology of porous solids. *J. Geophys. Res.*, 78:4924–4937.

Biot, M. A. and Willis, D. G. (1957). The elastic coefficients of the theory of consolidation. *J. Appl. Mech.*, 24:594–601.

Blacic, J., Halleck, P., D'Onfro, P., and Riecker, R. (1981). Thermomechanical properties of galesville sandstone. In *Mechanical behavior of Crustal Rocks: the Handin volume*, pages 153–159. Geophysical Monograph.

Blöcher, G., Reinicke, A., Moeck, I., Milsch, H., and Zimmermann, G. (2008). Concept of a hydro-mechanical-thermal simulation of a fractured reservoir. *ARMA, the 42nd US Rock Mechanics Symposium and 2nd U.S.-Canada Rock Mechanics Symposium*, 08(375).

Blöcher, G., Zimmermann, G., and Milsch, H. (2009). Impact of poroelastic response of sandstones on geothermal power production. *Pure Appl. Geophys.*, 166(5):1107–1123.

Blöcher, G., Zimmermann, G., Milsch, H., McDermott, C., and Huenges, E. (2007). Investigation of the undrained poroelastic response of sandstones to confining pressure via laboratory experiment, numerical simulation and analytical calculation. *Geological Society Special Publications*, In Rock Physics and Geomechanics in the Study of Reservoirs and Repositories(284):71–88.

Blöcher, M. G., Zimmermann, G., Moeck, I., Brandt, W., Hassanzadegan, A., and Magri, F. (2010). 3d numerical modeling of hydrothermal processes during the lifetime of a deep geothermal reservoir. *Geofluids*, 10(3):406–421.

Boley, B. A. and Weiner, J. H. (1988). *Theory of Thermal Stresses*. Dover Publications.

Bouteca, M. and Bary, D. (1994). Contribution of poroelasticity to reservoir engineering: Lab experiments, application to core decompression and implication in hp-ht reservoirs depletion. *SPE*.

Bouteca, M., Bary, D., and Maury, V. (1993). An experimental study of the contribution of the pore volume change to production within the framework of biots theory. *Proceedings of the 1993 Society of Core Analysts Technical Conference.*, pages 1–12.

Brace, W. (1980). Permeability of crystalline and argillaceous rocks. *Int. J. Rock Mech. Min. Sci.*, 17(5):241 – 251.

Brace, W. F. (1965). Some new measurements of linear compressibility of rocks. *J. Geophys. Res*, 70:391–398.

Brace, W. F. (1978). Volume changes during fracture and frictional sliding: A review. *Pure Appl. Geophys.*, 116:603–614.

Campanella, R. and Mitchell, J. (1968). Influence of temperature variations on soil behaviour,. *J. ASCE Soil Mech. Found. Div.*, 94(SM3):709–734.

Carman, P. (1956). *Flow of gases through porous media*. Butterworths Scientific Publications.

Carmichael, R. S. (1989). *Handbook of Physical Properties of Rocks*. CRC-Press.

Carroll, M. (1980). Mechanical response of fluid suturated porous materials. In *Theoretical and Applied Mechanics, Proc. 15th Int. Congress of Theoretical and Applied Mechanics, Toronto, August 1723, F. P. J. Rimrott and B. Tabarrok, eds., North-Holland, Amsterdam*, pages 251–262.

Carroll, M. M. and Katsube, N. (1983). The role of Terzaghi effective stress in linearly elastic deformation. *J. Energ. Resour. ASME*, 105(4):509–511.

Charlez, P. A. and Heugas, O. (1992). Measurement of thermoporoelastic properties of rocks, theory and applications. In Hudson, A., editor, *Rock characterization, ISRM Symposium, Eurock 92*, pages 42–46.

Cristescu, N. (1987). Elastic/viscoplastic constitutive equations for rock. *Int. J. Rock Mech. Min. Sci.*, 24(5):271 – 282.

David, C., Menendez, B., Zhu, W., and f. Wong, T. (2001). Mechanical compaction, microstructures and permeability evolution in sandstones. *Phys. Chem. Earth, Part A: Solid Earth And Geodesy*, 26(12):45–51.

David, C., Wong, T.-F., Zhu, W., and Zhang, J. (1994). Laboratory measurement of compaction-induced permeability change in porous rocks: Implications for the generation and maintenance of pore pressure excess in the crust. *Pure Appl. Geophys.*, 143:425–456.

David, E. and Zimmerman, R. W. (2012). Pore structure model for elastic wave velocities in fluid-saturated sandstones. *J. Geophys. Res*, 117:1–15.

Detournay, E. and Cheng, A. H.-D. (1993). *Fundamentals of poroelasticity. In Comprehensive Rock Engineering: Principles, Practice and Projects*, volume 2, chapter 5, pages 113 –169. Pergamon Press.

Dillen, M. (2000). *Time-lapse seismic monitoring of subsurface stress dynamics.* PhD thesis, Delft University of Technology.

Economides, M. and Nolte, K. (2000). *Reservoir stimulation.* J. Wiley.

Eshelby, J. D. (1957). The determination of the elastic field of an ellipsoidal inclusion, and related problems. *Proceedings of the Royal Society of London. Series A. Mathematical and Physical Sciences*, 241(1226):376–396.

Evans, B. and Kohlstedt, D. . L. (1995). *Rock Physics and Phase Relations A Handbook of Physical Constants*, chapter Rheology of rocks. American Geophysical Union.

Fjaer, E., Holt, R., Horsrud, P., and Raaen, A. M. (1992). *Petroleum Related Rock Mechanics.* Elsevier, Amsterdam,.

Fortin, J., Schubnel, A., and Guguen, Y. (2005). Elastic wave velocities and permeability evolution during compaction of Bleurswiller sandstone. *Int. J. Rock Mech. Min. Sci.*, 42(78):873 – 889.

Franquet, J. and Abass, H. (1999). Experimental evaluation of Biot's poroelastic parameter, three different methods. *The 37th U.S. Symposium on Rock Mechanics (USRMS)*, pages 349–355.

Fredrich, J. and Fossum, A. F. (2002). large scale three dimensional geomechanical modeling of reservoirs: examples from california and the deepwater gulf of mexico. *Oil and Gas Science and Technology*, 57:423–441.

Garaia, J. and Laugier, A. (2007). The temperature dependence of the isothermal bulk modulus at 1 bar pressure. *J. Appl. Phys.*, 101-023514:1–4.

Gehrke, D. (2006). Thermisch-hydraulische 3D modellierung des geothermischen reservoirs um die dublette (E GrSk 03/90 / Gt GrSk4/05) von Groß Schönebeck unter bercksichtigung von stimulationsmaßnahmen, ID: 11253. Technical report, Ernst-Moritz-Arndt-Universität Greifswald und GFZ Potsdam.

GeoQuest (2010). *GeoQuest-Reservoir Simulation Suite.* Schlumberger.

Ghabezloo, S. and Sulem, J. (2008). Stress dependent thermal pressurization of a fluid-saturated rock. *Rock Mech. Rock Eng.*, 42:1–24.

Ghabezloo, S. and Sulem, J. (2010). Effect of the volume of the drainage system on the measurement of undrained thermo-poro-elastic parameters. *Int. J. Rock Mech. Min. Sci.*, 47(1):60 – 68.

Ghabezloo, S., Sulem, J., and Saint-Marc, J. (2009). Evaluation of a permeability porosity relationship in a low-permeability creeping material using a single transient test. *Int. J. Rock Mech. Min. Sci.*, 46(4):761 – 768.

Goetze, C. and Evans, B. (1979). Stress and temperature in the bending lithosphere as constrained by experimental rock mechanics. *Geophysical Journal International*, 59(3):463–478.

Guéguen, Y. and Boutéca, M. (1999). Propriétés mécaniques des roches : pression de pore et effets d'échelle. *Oil & Gas Science and Technology - Rev. IFP*, 54(6):703–714.

Guéguen, Y. and Boutéca, M. (2004). *Mechanics of Fluid Saturated Rocks*. Elsevier Academic Press.

Guéguen, Y. and Dienes, J. (1989). Transport properties of rocks from statistics and percolation. *Mathematical Geology*, 21:1–13.

Guéguen, Y., Gavrilenko, P., and Le Ravalec, M. (1996). Scales of rock permeability. *Surveys in Geophysics*, 17:245–263.

Guéguen, Y. and Palciauskas, V. (1994). *Introduction to the Physics of Rocks*. Princeton University Press.

Handin, J., Hager, R. V., Friedman, M., and Feather, J. N. (1963). Experimental deformation of sedimentary rocks under confining pressure; pore peressure tests. *AAPG Bulletin*, 47:717–755.

Handin, J. W. and Hager, R. V. (1957). Experimental deformation of sedimentary rocks under confining pressure; [part 2] tests at high temperature. *AAPG Bulletin*, 42:2892–2934.

Hart, D. and Wang, H. E. (1999). Pore pressure and confining stress dependence of poroelastic linear compressibilites and skempton B coefficient for berea sandstone. *Rock mechanics for Industry, Balkema Rotterdam*, pages 365–371.

Hart, D. J. and Wang, H. F. (1995). Laboratory measurements of a complete set of poroelastic moduli for Berea sandstone and Indiana limestone. *J. Geophys. Res*, 100(B9):17741–17751.

Hashin, Z. and Shtrikman, S. (1963). Conductivity of polycrystals. *Phys. Rev.*, 130(1):129–133.

Hassanzadegan, A., Blöcher, G., Zimmermann, G., and Milsch, H. (2012). Thermoporoelastic properties of Flechtinger sandstone. *Int. J. Rock Mech. Min. Sci.*, 49(0):94 –104.

Hassanzadegan, A., Blöcher, G., Zimmermann, G., Milsch, H., and Moeck, I. (2011). Induced stress in a geothermal doublet system. In *Thirty-Sixth Workshop on Geothermal Reservoir Engineering, Stanford University, Stanford, California, SGP-TR-191*, pages 1–1.

Hearst, J. and Nelson, P. (1985). *Well logging for physical properties*. McGraw-Hill.

Hecht, C. A., Bönsch, C., and Bauch, E. (2005). Relations of rock structure and composition to petrophysical and geomechanical rock properties: Examples from permocarboniferous red-beds. *Rock Mech. Rock Eng.*, 38(3):197– 216.

Heffer, K. (2002). Geomechanical influences in water injection projects: An overview. *Oil & Gas Science and Technology - Rev. IFP*, 57(5):415–422.

Heiland, J. (2003). Poroelastic behaviour of physical properties in Rotliegend sandstones under uniaxial strain. *Pure and Applied Geophysics*, 160(5):889–908.

Heiland, J. and Raab, S. (2001). Experimental investigation of the influence of differential stress on permeability of a lower Permian (Rotliegend) sandstone deformed in the brittle deformation field. *Physics and Chemistry of the Earth, Part A: Solid Earth and Geodesy*, 26(1-2):33 – 38.

Hill, R. (1952). The elastic behaviour of a crystalline aggregate. *Proceedings of the Physical Society. Section A*, 65(5):349–354.

Holl, H.-G., Hurter, S., Saadat, A., Khler, S., Wolfgramm, M., Zimmermann, G., Trautwein, U., Winter, H., Legarth, B., and Huenges, E. (2003). First hand experience in a second hand borehole. *International Geothermal Conference: Hydraulic experiments and scaling in the geothermal well Groß Schönebeck after reopening*.

Homand-Etienne, F. and Houpert, R. (1987). Comportement mecanique des roches en compression diffrentes tempratures. *International congress on rock mechanics*, 6:965–969.

Huenges, E., Holl, H.-G., Bruhn, D., Brandt, W., Saadat, A., Moeck, I., and Zimmermann, G. (2007). Current state of the EGS project groß schönebeck– drilling into the deep sedimentary geothermal reservoir. *Proceedings European Geothermal Congress, Unterhaching, Germany, 30 May-1 June*.

Huenges, E., Trautwein, U., Legarth, B., and Zimmermann, G. (2006). Fluid pressure variation in a sedimentary geothermal reservoir in the North German basin: Case study Groß Schönebeck. *Pure and Applied Geophysics*, 163(10):2141 – 2152.

Jaeger, J., Cook, N., and Zimmerman, R. (2007). *Fundamentals of Rock Mechanics*. Blackwell Pub.

Kern, H. (1978). The effect of high temperature and high confining pressure on compressional wave velocities in quartz-bearing and quartz-free igneous and metamorphic rocks. *Tectonophysics*, 44(1-4):185 – 203.

Kerner, E. H. (1956). The electrical conductivity of composite media. *Proceedings of the Physical Society. Section B*, 69(8):802–807.

Kung, J., Rigden, S. M., and Jackson, I. (2000). Silicate perovskite analogue ScAlO3: temperature dependence of elastic moduli. *Phys. Earth Planet In.*, 120(4):299 – 314.

Kurz, J. H., Grosse, C. U., and Reinhardt, H.-W. (2005). Strategies for reliable automatic onset time picking of acoustic emissions and of ultrasound signals in concrete. *Ultrasonics*, 43(7):538 – 546.

Kwiatek, G., Bohnhoff, M., Dresen, G., Schulze, A., Schulte, T., Zimmermann, G., and Huenges, E. (2008). Microseismic event analysis in comjunction with stimulation treatment at the geothermal research well GtGrSk4/05 in groß schönebeck geothermal reservoir. *proceedings, Thirty-third workshop on geothermal reservoir engineering Stanford university, Stanford, California*, SGP-TR-185.

Lade, P. V. (1988). Effects of voids and volume changes on the behaviour of frictional materials. *Int. J. Numer. Anal. Met.*, 12:351–370.

Legarth, B., Huenges, E., and Zimmermann, G. (2005). Hydraulic fracturing in a sedimentary geothermal reservoir: results and implication. *Int J Rock Mech Mining Sci*, 42:10281041.

Lemmon, E., Huber, M., and Mclinden, M. (2007). *Reference fluid thermodynamic and transport propertiesrefprop*. version 8.0, National Institute of Standards and Technology, Gaithersburg, NIST Standard Reference Database 23.

Levin, V. (1967). Thermal expansion coefficients of heterogeneous materials. *Mekh. Tverd*, 2:93 – 94.

Lotz, B. (2004). Neubewertung des rezenten Wäarmestroms im Nordostdeutschen Becken. In *Geowissenschaften sichern die Zukunft*, volume 34.

Mackenzie, J. K. (1950). The elastic constants of a solid containing spherical holes. *Proceedings of the Physical Society. Section B*, 63(1):2–11.

Manghnani, M., Fisher, E., and Jr., W. B. (1972). Temperature dependence of the elastic constants of single-crystal rutile between 4 and 583 k. *J. Phys. Chem. Solids*, 33(11):2149 – 2159.

Mavko, G., Mukerji, T., and Dvorkin, J. (2003). *The Rock Physics Handbook: Tools for Seismic Analysis of Porous Media*. Cambridge University Press.

Mavko, G. M. and Nur, A. (1978). The effect of nonelliptical cracks on the compressibility of rocks. *J. Geophys. Res.*, 83:4459–4468.

McTigue, D. (1986). Thermoelastic response of fluid-saturated porous rock. *J. Geophys. Res*, 91(B9):9533–9542.

McTigue, D. F. (1990). Flow to a heated borehole in porous, thermoelastic rock analysis. *Water Resour. Res.*, 26:1763–1774.

Milsch, H., Blöcher, G., and Engelmann, S. (2008). The relationship between hydraulic and electrical transport properties in sandstones: An experimental evaluation of several scaling models. *Earth Planet. Sc. Lett.*, 275(3-4):355 – 363.

Milsch, H., Seibt, A., and Spangenberg, E. (2009). Long-term petrophysical investigations on geothermal reservoir rocks at simulated in situ conditions. *Transp Porous Med*, 77(1):59–78.

Moeck, I., Schandelmeier, H., and Holl, H. (2008). The stress regime in a Rotliegend reservoir of the Northeast German Basin. *Int J Earth Sci*, 98(7):1643–1654.

Morlier, P. (1971). Description de létat de fissuration d'une roche à partir déssais non-destructifs simples. *Rock Mech Rock Eng*, 3:125–138.

Nur, A. and Byerlee, J. D. (1971). An effective stress law for elastic deformation of rock with fluids. *J. Geophys. Res*, 76:6414–6419.

Nur, A. and Wang, Z. (1989a). *Seismic and Acoustic Velocities in Reservoir Rocks: Experimental studies.* Geophysics reprint series. Society of Exploration Geophysicists.

Nur, A. and Wang, Z. (1989b). *Seismic and Acoustic Velocities in Reservoir Rocks: Theoretical and model studies.* Society of Exploration Geophysicists.

Palciauskas, V. and Domenico, P. A. (1982). Characterization of drained and undrained response of thermally loaded repository rocks. *Water Resour Res*, 18(2):281–290.

Palciauskas, V. V. and Domenico, P. A. (1988). Fluid pressures in deforming porous rocks. *Water Resour. Res*, 25(2):203–213.

Palen, W. (1978). *The effects of temperature, pressure, and saturation on the sonic velocities and dynamic elastic moduli of reservoir sandstones.* University of California, Berkeley.

Ravalee, M. L. and Guéguen, Y. (1994). Permeability models for heated saturated igneous rocks. *J. Geophys. Res*, 99:24251–24261.

Renard, P. and de Marsily, G. (1997). Calculating equivalent permeability: a review. *Advances in Water Resources*, 20(56):253 – 278.

Reuss (1929). Berechnung der Fliessgrenze von Mischkristallen auf Grund der Plastizitätsbedingung für Einkristalle. *ZAMM - Journal of Applied Mathematics and Mechanics*, 9(1):49–58.

RGCOE (2010). *Reservoir Geomechanics Center of Excellence.* Schlumberger.

Rice, J. R. and Cleary, M. P. (1976). Some basic stress diffusion solutions for fluid-saturated elastic porous media with compressible constituents. *Rev Geophys Space Phys*, 14(2):227–241.

Roeloffs, E. A. (1988). Fault stability changes induced beneath a reservoir with cyclic variations in water level. *J. Geophys. Res*, 93(B3):2107 – 2124.

Sarout, J. (2012). Impact of pore space topology on permeability, cut-off frequencies and validity of wave propagation theories. *Geophys J Int*, 189:481–492.

Scheidegger, A. (1974). *The physics of flow through porous media.* University of Toronto Press.

Schepers, A. (2012). *Effects of fluid-rock interactions on electrical conductivity and permeability of Feldspar-rich sandstones.* PhD thesis, Deutsches GeoForschungsZentrum GFZ, Potsdam, STR1207.

Scheu, B., Kern, H., Spieler, O., and Dingwell, D. (2006). Temperature dependence of elastic p- and s-wave velocities in porous Mt. Unzen dacite. *J Volcanol Geoth Res*, 153(1-2):136 – 147.

Scholz, C. H. (1968). Microfracturing and the inelastic deformation of rock in compression. *Journal of Geophysical Research*, 73:1417–1432.

Schön, J. (2004). *Physical properties of rocks: fundamentals and principles of petrophysics.* Elsevier.

Schön, J., Helbig, K., and Treitel, S. (1998). *Handbook of geophysical exploration.* Geophysical Press.

Segall, P. and Fitzgerald, S. D. (1998). A note on induced stress changes in hydrocarbon and geothermal reservoirs. *Tectonophysics*, 289(1-3):117 – 128.

Simmons, G. and Brace, W. F. (1965). Comparison of static and dynamic measurements of compressibility of rocks. *J. Geophys. Res*, 70:5649–5656.

Sisavath, S., Jing, X., and Zimmerman, R. W. (2000). Effect of stress on the hydraulic conductivity of rock pores. *Phys Chem Earth Pt A*, 25(2):163 – 168.

Smith, J., Ness, H. V., and Abbott, M. (2001). *Introduction to Chemical Engineering Thermodynamics.* McGraw-Hill.

Soltanzadeh, H. and Hawkes, C. (2008). *Porous Media: Heat and Mass Transfer, Transport and Mechanics*, chapter 2, Induced Poroelastic and Thermoelastic Stress Changes Within Reservoirs During Fluid Injection and Production,, pages 27–57. Nova Science.

Somerton, W. (1980). Some physical properties of cerro prieto cores. *Geothermics*, 9(1-2):159 – 168.

Somerton, W. H. (1992). *Thermal properties and temperature-related behavior of rock-fluid systems.* Elsevier Science Publishing Company Inc.

Somerton, W. H., Janah*, A. U., and Ashqar, P. . (1981). Thermal expansion of fluid saturated rocks under stress. *SPWLA Twenty second annual logging symposium*, pages 1–8.

Sulem, J., Vardoulakis, I., Papamichos, E., Oulahna, A., and Tronvoll, J. (1999). Elasto-plastic modelling of red wildmoor sandstone. *Mech Cohes-Frict Mat*, 4(3):215–245.

Taylor, R. E. and Taylor, R. E. (1998). *Thermal expansions of Solids.* ASM International.

Terzaghi, K. (1923). Die Berechnung der Durchlaessigkeitsziffer des Tones aus dem Verlauf der hydrodynamischen Spannungserscheinungen. *Sitzungsberichte der Akadamie der Wissenchaften in Wien, Mathematisch- Naturwissenschaftliche Klasse, Abteilung, IIa*, 132(4):105–124.

Trautwein, U. and Huenges, E. (2005). Poroelastic behaviour of physical properties in Rotliegend sandstones under uniaxial strain. *Int. J. Rock Mech. Min. Sci.*, 42(7-8):924 – 932.

Turner, P. (1946). Thermal expansion stresses in reinforced plastics. *J. Res. NBS*, 37:239–250.

Vishal, V., Pradhan, S., and (2011), T. S. (2011). Tensile strength of rock under elevated temperatures. *Geotechnical and Geological Engineering*, 29(6):1127–1133.

Voigt, W. (1928). *Lehrbuch der Krystallphysik*. Teubner, Leipzig.

Walsh, J. B. (1965). The effect of cracks on the compressibility of rock. *J. Geophys. Res*, 70(2):381–389.

Walsh, J. B. (1973). Theoretical bounds for thermal expansion, specific heat, and strain energy due to internal stress. *J. Geophys. Res.*, 78:7637–7646.

Walsh, J. B. (1980). Static deformation of rock. *J Eng Mech Div ASCE*, 106:1005–1019.

Yale, D. (1985). Recent advances in rock physics. *Geophysics*, 50(12):2480–2491.

Yale, D. P. and Jamieson, W. H. (1994). Static and dynamic mechanical properties of carbonates. In *Rock Mechanics*, pages 1–1. Balkema, Rotterdam.

Yale, D. P. and Nieto, J. (1995). Effect of cementation on the static and dynamic mechanical properties of the Rotliegend sandstone. In *Rock mechanics: proceedings of the 35th U.S. Symposium, University of Nevada, Reno*. A.A. Balkema.

Zang, A. (1993a). Finite element study on the closure of thermal microcracks in feldspar/quartz-rocks–I. Grain-boundary cracks. *Geophysical Journal International*, 113:17–31.

Zang, A. (1993b). Finite element study on the closure of thermal microcracks in feldspar/quartz-rocks–II. Intra-, transgranular and mixed cracks. *Geophysical Journal International*, 113:32–44.

Zang, A. (1997). Akustische emissionen beim sprödbruch von gestein. habilitation thesis,. Technical report, Deutsches GeoForschungsZentrum GFZ, Potsdam, STR 97/19.

Zang, A. and Berckhemer, H. (1993). Classification of crystalline drill cores from the ktb deep well based on strain, velocity and fracture measurements. *Int. J. Rock Mech. Min. Sci.*, 30(4):331 – 342.

Zimmerman, R. W. (1991). *Compressibility of Sandstones*. Developments in Petroleum Science. Elsevier.

Zimmerman, R. W. (2000). Coupling in poroelasticity and thermoelasticity. *International Journal of Rock Mechanics and Mining Sciences*, 37(1-2):79 – 87.

Zimmerman, R. W., Somerton, W., and King, M. (1986). Compressibility of porous rocks. *Journal of Geophysical Research*, 91:12765–12777.

Zimmermann, G., Blöcher, G., Reinicke, A., and Brandt, W. (2011). Rock specific hydraulic fracturing and matrix acidizing to enhance a geothermal system concepts and field results. *Tectonophysics*, 503(12):146 – 154.

Zimmermann, G., Reinicke, A., Blöcher, G., Milsch, H., Gehrke, D., Holl, H.-G., Moeck, I., Brandt, W., and Saadat, A. (2007). Well path design and stimulation treatments at the geothermal research well GtGrSk4/05 in Groß Schönebeck. Stanford, California. thirty-second workshop on geothermal reservoir engineering, Stanford University.

Zoback, M. and Byerlee, J. (1975). Permeability and effective stress. *American Association Of Petroleum Geologists Bulletin*, 59:154–158.